Revision 2

Nanostructural domains in martian apatites that record primary subsolidus exsolution of halogens: Insights into nakhlite petrogenesis

Marina Martínez[a*,†], Charles K. Shearer[a,b], and Adrian J. Brearley[a]

[a]Department of Earth & Planetary Sciences, MSC03-2040, 1University of New Mexico, Albuquerque, NM 87131, USA (mmartinezjimenez@unm.edu)

[b]Institute of Meteoritics, MSC03-2040, University of New Mexico, Albuquerque, NM 87131, USA

[*]Corresponding author.
[†]Present address: Universitat Autònoma de Barcelona (UAB), Edifici Cs, Av. de l'Eix Central, s/n, 08193 Cerdanyola del Vallès, Barcelona (Marina.Martinez@uab.cat)

ABSTRACT

The microstructures of selected F-, Cl-, OH-bearing martian apatite grains, two in Northwest Africa (NWA) 998 (cumulus apatites, embedded in pyroxene) and a set of four in Nakhla

(intercumulus apatites), were studied by focused ion beam - transmission electron microscopy (FIB-TEM) techniques. Our results show that the nanostructure of martian apatite is characterized by a domain structure at the 5-10 nm-scale defined by undulous lattice fringes and slight differences in contrast, indicative of localized elastic strain within the lattices and misorientations in the crystal. The domain structure records a primary post-magmatic signature formed during initial subsolidus cooling ($T < 800$ ºC), in which halogens clustered by phase separation (exsolution), but overall preserved continuity in the crystalline structure. Northwest Africa 998 apatites, with average Cl/F ratios of 1.26 and 2.11, show higher undulosity of the lattice fringes and more differences in contrast than Nakhla apatites (average Cl/F = 4.23), suggesting that when Cl/F is close to 1, there is more strain in the structure. Vacancies likely played a key role stabilizing these ternary apatites that otherwise would be immiscible. Apatites in Nakhla show larger variations in halogen and rare-earth element (REE) contents within and between grains that are only a few microns apart, consistent with growth under disequilibrium conditions and crystallization in open systems. Nakhla apatite preserves chemical zonation, where F, REEs, Si, and Fe are higher in the core and Cl increases towards the outer layers of the crystal. There is no evidence of subsolidus ionic diffusion or post-magmatic fluid interactions that affected bulk apatite compositions in NWA 998 or Nakhla. The observed zonation is consistent with crystallization from a late-stage melt that became Cl-enriched, and assimilation of volatile-rich crustal sediments is the most plausible mechanism for the observed zonation. This work has broader implications for interpreting the chemistry of apatite in other planetary systems.

Keywords: apatite, halogens, nanostructures, FIB-TEM, nakhlites, Mars.

INTRODUCTION

The calcium phosphate mineral apatite, $Ca_{10}(PO_4)_6(F,OH,Cl)_2$, is a ubiquitous, accessory mineral in igneous, metamorphic, sedimentary, and hydrothermal systems present in most planetary bodies in the solar system (e.g., Earth, Moon, Mars, and asteroids). The widespread interest in apatite derives from the fact that it contains the volatiles F, Cl, and OH; thus, it can be used as an important tracer for reconstructing petrogenetic processes in different planetary environments (e.g., Shearer et al., 2011; Tartèse et al., 2014; Webster and Piccoli, 2015; McCubbin and Jones, 2015; Zirner et al., 2015). For example, apatite is used to estimate the activities (fugacities) of volatiles, both in melts and fluids (e.g., McCubbin and Ustunisik, 2018). These studies provide important insights into the role of volatiles in magmatic and hydrothermal planetary processes, the identification of planetary volatile reservoirs, and provide glimpses into primordial volatile behavior during the early Solar System (e.g., accretion and differentiation; Sharp et al., 2016). However, the formation of apatite is very complex, and can result from a wide range of different processes, from primary magmatic crystallization to the secondary products of alteration or metamorphic and metasomatic processes (e.g., Zirner et al., 2015).

Despite the wealth of data from compositional and isotopic studies of apatite (e.g., Williams et al., 2016; Shearer et al., 2018), the current lack of microstructural information for planetary or even terrestrial apatite represents a major gap in interpreting the volatile record preserved in this complex mineral. Remarkably, there has only been one single TEM study of the microstructure of terrestrial apatite, where the authors showed nanometric exsolution phenomena and thus, a miscibility gap for apatite was constrained for the first time (Ferraris et al., 2005). Other techniques, such as electron backscatter diffraction and atom probe tomography, have also been used to gain structural information on the effects of volatiles in shocked apatite (Černok et

al., 2019; Barrett et al., 2021; Darling et al., 2021). However, given that the nakhlites are the least shocked martian meteorites (~15–20 GPa; e.g., Malavergne et al., 2001; Treiman and Irving, 2008), the effects of shock on apatite and other minerals are considered minimal, and apatite in the nakhlites represent a good starting point to observe structures related to their petrogenetic formation processes. More recently, the first studies on the microstructure of extraterrestrial apatite (i.e., Słaby et al., 2017; Birski et al., 2019) have demonstrated that micro- and nanostructural examination of apatite has the potential to provide constraints on conditions of crystallization, precipitation, and fluid interaction of a magmatic source. Furthermore, the volatile contents and isotopic compositions (D/H (deuterium/hydrogen), $^{37}Cl/^{35}Cl$, $^{18}O/^{16}O$) in apatite have been used to better understand many of these processes related to the origin and evolution of Mars (e.g., Williams et al., 2016; Shearer et al., 2018; Peslier et al., 2019; Barnes et al., 2020).

One of the main caveats in using martian apatite as a petrogenetic indicator is that the extreme variability of Cl/F ratios in Nakhla apatite cannot be explained by a typical igneous process (e.g., Meurer and Boudreau, 1996). Different hypotheses have been proposed to account for this variability, including secondary processes involving low-temperature aqueous fluids (Bridges and Grady, 1999, 2000; Bridges et al., 2001) and crystallization from a magma that underwent assimilation of Cl-, LREE-rich fluids (McCubbin and Nekvasil, 2008; McCubbin et al., 2013) or crustal sediments (e.g., Usui et al., 2012; Lin et al., 2013; Shearer et al., 2018). In these different scenarios, apatites will form with different Cl/F ratios. For example, when apatite crystallizes with a fluid present, Cl partitions into the fluid phase whereas F is retained in the melt, resulting in F-rich apatites (Holland, 1972; Kilinc and Burnham, 1972; Aiuppa et al., 2009;

Ustunisik et al., 2011). In comparison, crystallization from a melt will form Cl-rich apatites due to equilibration of interstitial phases with a magma that assimilated a Cl-rich contaminant.

For scenarios where fluids are involved, different sources for the fluid have been suggested, for example, aqueous alkali-ferrous chloride fluids that exsolved from the parental melt as it crystallized (Giesting and Filiberto, 2016), or alternatively, crustal fluids (brines) that infiltrated from the surface (Cartwright et al., 2013). Another possibility that has been proposed for the origin of volatiles in the shergottites is Cl-rich aqueous brines that formed through degassing of the magma chamber or sills when magmas crystallized at depth (Howarth et al., 2015). Crustal assimilation (either a fluid or sediment) is supported by the existence of two Cl-isotopic reservoirs recorded in apatites from the Chassigny meteorite: intercumulus apatites are enriched in heavy Cl, corresponding to the values from the crust, whereas apatite inside melt inclusions in olivine are enriched in light Cl, corresponding to the mantle signature, as well as to the primordial solar system composition from which Mars accreted (McCubbin et al., 2010; Shearer et al., 2018). This discovery led to the conclusion that the crust (heavy isotopic reservoir) likely played a role during Chassigny crystallization, which was constrained to have occurred after the formation of melt inclusions in pyroxenes, but before solidification of the interstitial melt to cumulus olivine in Chassigny (McCubbin et al., 2013).

The present study examines the (sub)microstructures of martian apatites and explores their compositions at the nanoscale using transmission electron microscopy (TEM) in an effort to explore the microstructures of apatite as potential indicators of their formation and possible subsequent alteration processes. Understanding the microstructure of apatite has the potential to shed new light on the magmatic and subsolidus evolution of volatiles in the martian volcanic system and has broader implications for understanding other planetary environments.

This is the peer-reviewed, final accepted version for American Mineralogist, published by the Mineralogical Society of America.
The published version is subject to change. Cite as Authors (Year) Title. American Mineralogist, in press.
DOI: https://doi.org/10.2138/am-2022-8794. http://www.minsocam.org/

SAMPLES AND ANALYTICAL METHODS

Petrographic observations and transmission electron microscope analyses of various apatite grains were made in the two nakhlites, NWA 998 (,002) and Nakhla. The studied samples are polished 1-inch round petrographic thin sections from the Institute of Meteoritics Collection at the University of New Mexico. Both samples were coated with a 10 nm layer of carbon to prevent charging during scanning electron microscopy (SEM) imaging. Each thin section was studied to identify and locate apatite grains using backscattered electron (BSE) imaging and energy dispersive spectroscopy (EDS) X-ray analysis on a FEI Quanta 3D Dualbeam© field emission gun (FEG) SEM. The analytical conditions used were 30 kV accelerating voltage and a beam current of 4 nA. The instrument is equipped with an EDAX Genesis EDS system and an Apollo 40 SDD 40 mm^2 EDS detector for qualitative X-ray analysis. Complete BSE mosaics of the entire thin sections were obtained using SEM to assess the general spatial distribution of apatite grains and aid location within the samples (Fig. 1). We did not perform quantitative analyses of the complete distribution or modal abundance of the apatite grains. BSE imaging at very low kV (5-10 kV) and high contrast was performed to examine apatite grains at high magnifications and determine their possible microstructures and petrographic occurrences.

Focused ion beam (FIB) samples for TEM of selected apatite grains were prepared with the FIB technique using the FEI Quanta 3D FEGSEM/FIB instrument. The region of interest was protected from sputtering by the Ga^+ beam by depositing a 2 μm-thick Pt strip across the area prior to sample extraction. The FIB samples were removed from the thin sections by the in situ lift-out technique using an Omniprobe 200 micromanipulator and transferred onto Cu half grids. The samples were ion milled to a thickness of approximately 50 nm for optimal high-resolution imaging with ion beam currents decreasing from 1 nA down to 53 pA for the final stage of ion

137 milling, at 30 kV operating voltage. Dark-field STEM images of one FIB section in NWA 998
138 showed nm-scale worm-like features that are present on all the phases, including epoxy-filling
139 fractures. These are artifacts caused by re-deposition during FIB preparation that were
140 subsequently removed using a low-angle final polishing step with a 2 kV and 50 pA ion beam.
141 Bright-field (BF) TEM imaging, high-resolution TEM (HR-TEM), TEM-EDS, scanning TEM
142 (STEM)-EDS, selected area electron diffraction (SAED), high-angle annular dark field
143 (HAADF) imaging, and STEM-EDS mapping were performed on the FIB samples using a JEOL
144 2010F FEG TEM/STEM operating at 200 kV using GATAN Microscopy Suite® (GMS)
145 imaging software. Quantitative EDS analyses were obtained using an Oxford AZTec X-ray
146 analysis system with a X-Max 80N 80 mm^2 SDD energy dispersive X-ray spectrometer (EDS)
147 detector system. Each spectrum was collected for 300 and 500 seconds in regular TEM mode and
148 Scanning TEM mode, respectively, using a spot size of 5 and a defocused beam of ~100 nm in
149 TEM mode to reduce beam damage. Quantification of EDS data was conducted using the Cliff-
150 Lorimer thin film approximation with theoretical k-factors. Errors were all <5% (relative error).
151 The analyses assume oxygen present according to oxide stoichiometry and normalized to 100
152 wt%. All SEM and TEM studies were performed at the Department of Earth and Planetary
153 Science at the University of New Mexico.

154 The measured X-ray flux from apatite is affected by crystal orientation (Stormer et al.,
155 1993; Stock et al., 2015). As a result, apparent F concentrations can change by as much as 100%
156 when the electron beam is parallel to the *c* axis (Stormer et al., 1993; Stock et al., 2015), which is
157 the case for FIB sections 2 (NWA 998) and 3 (Nakhla). Therefore, there might be errors with the
158 apparent F concentration reported here (less for Cl, Ca, and P; Webster and Piccoli, 2015). To
159 correct that, we have used a relatively large TEM electron beam diameter (~1-2 μm), as far as it

was possible, to reduce the electron beam densities. FIB1 (NWA 998), cut parallel to the *c* axis, gives more accurate analyses for F and Cl, as the electron beam is incident perpendicular to the *c* axis (Goldoff et al., 2012; Stock et al., 2015). However, because FIB sections 1 and 2 (NWA 998) give similar results, we consider this effect to be minimal. Finally, the missing component is represented by Z content in the tables (1 = F + Cl + Z), which includes OH and vacancies; thus, the halogen site is assumed not fully occupied (Piccoli and Candela, 2002).

RESULTS

General petrographic characteristics of Northwest Africa 998 apatites

The martian augite-rich cumulate basalt NWA 998 represents the most equilibrated nakhlite currently known (McCubbin et al., 2013). The crystallization sequence in this sample started with subhedral olivine, followed by orthopyroxene, titanomagnetite, zoned augite to pigeonite, which represents the framework of the rock with a modal abundance of ~75 vol% (Treiman and Irving, 2008), plagioclase, and interstitial mesostasis regions (Irving et al., 2002; Russell et al., 2003; Treiman, 2005; Treiman and Irving, 2008). Late-stage intercumulus regions consist of potassium feldspar, chlorapatite, pyrrhotite, chalcopyrite, titanomagnetite, and alkali-rich glass.

Apatites in NWA 998 are among the largest found in the martian meteorites, and textural interpretations suggest both cumulus and intercumulus origins (e.g., McCubbin et al., 2013). Apatite occurring as mineral inclusions within titanomagnetite (e.g., apatites 5.2 and 5.4 in Fig. 2c) have been interpreted as indicating a relatively early crystallization inside melt pockets during growth of the cumulus minerals (McCubbin et al., 2013). Nevertheless, Treiman and Irving (2008) concluded that all apatites are intercumulus and attributed the larger apatites rimming cumulus pyroxenes to the replacement of augite by pigeonite at the rims of the crystal

(producing zonation), which released Ca into the melt. The authors argue that the replacement of augite by low-Ca pyroxene could have been a response to devolatilization (i.e., loss of water or other components from the magma), although the lack of merrillite in late-stage mesostasis pockets in NWA 998 does not support devolatilization.

Apatites in NWA 998 are coarse-grained, ranging from ~5 to ~200 μm in size (relatively large in comparison to other samples, which range between ~5 and ~50 μm in size), randomly distributed, fractured, and mainly subhedral, but several euhedral grains are also identified. Backscattered electron images of NWA 998 apatites are presented in Figure 2, and additional images can be found in Martínez (2021). They mainly occur with pigeonite, augite, alkali feldspar, K-,Na-rich glass, titanomagnetite, ilmenite, and troilite, typically associated with large fractures between cumulus pyroxene grains. All apatite grains lack observable zonation at the SEM scale. Cumulus apatites, the objects of this study, are those that are totally or partially included in pigeonite (e.g., at the interface between cumulus Fe-rich pigeonite grains, Figs. 1, 2a) or augite (e.g., Fig. 2b-d). These cumulus apatite grains are generally larger and more equant than intercumulus apatites, reaching similar sizes to other crystals in the paragenetic sequence. Cumulus apatites may have crystallized at the very end of pyroxene crystallization, near the surface between cumulus pigeonite grains, regions where incompatible elements accumulated. Our petrographic observations indicate that cumulus apatites crystallized before titanomagnetite (e.g., Fig. 2c).

Compositionally, apatites in NWA 998 show little variation along the F-Cl join (~1:1 ratio) in the ternary plot of the X-site occupancy ($F_{0.84}Cl_{0.76}OH_{0.40}$ atoms per formula unit (apfu); McCubbin et al., 2013; Fig. 4), with a typical OH content >20% of the Z-site occupancy, calculated based on stoichiometry (Bunch and Reid, 1975; Treiman and Irving, 2008; McCubbin

et al., 2013). Nonetheless, Channon (2013) only measured 0.07-0.11 wt% H_2O in NWA 998 apatite using secondary ion mass spectrometry (SIMS). A ternary F-Cl-Z plot, where Z = missing component, of NWA 998 and Nakhla apatite compositions reported in the literature by EPMA and SIMS, along with results obtained in the present study by S/TEM-EDS, is presented in Figure 4.

General petrographic characteristics of Nakhla apatites

Nakhla belongs to a more evolved stage in the paragenetic sequence of the parental liquid compared to NWA 998 (Wadhwa and Crozaz, 1995; Treiman and Irving, 2008; McCubbin et al., 2013). Examples of BSE images of Nakhla apatites can be found in Figure 3 and in Martínez (2021). Apatite grains in Nakhla only crystallized in the interstitial regions between cumulus grains under conditions far from equilibrium and rapid cooling. Apatites are randomly distributed throughout the thin section and range from moderately to highly elongated, most likely due to different orientations of elongate crystals within the section, and have subhedral to anhedral habits. Nakhla apatites are significantly smaller (~1-5 μm wide and up to 50 μm long, with a mean length of ~20 μm) compared to NWA 998 apatites. The myriad of apatites occur in groups of crystals that range from randomly oriented (most cases, e.g., Fig. 3a,b) to parallel or subparallel (rarer, e.g., Fig. 3c). They are found in almost all intercumulus residual mesostasis pockets, closely intergrown with K-rich glass, associated with plagioclase (~50 μm in size) that is compositional zoned in An content, titanomagnetite (~ 20-50 μm size), troilite (ranging from sub-μm to ~20 μm in size), and silica (ranging from a few microns to ~20 μm in size). Typically, each intercumulus region contains more than one individual apatite grain. Fractures are present in all apatite grains. The micron-sized apatites can occur in trails or clustered at the interface between feldspathic glass and crystalline feldspar (e.g., Fig. 3a,b). In contrast to NWA 998,

apatites in Nakhla show zonation, where the cores of the apatite needles have a lower Z contrast in BSE imaging (e.g., apatites 2.2 and 3 in Fig. 3b,d). Compositionally, apatite grains in Nakhla have highly variable Cl/F ratios (from 1.55 to 27.5, Table 3), from very Cl-rich to very F-rich, with a missing component abundance ranging from 0 to 14 mol% (McCubbin et al., 2013; Brounce et al., 2022) (Fig. 4).

TEM observations

A total of three FIB sections were cut for microstructural analysis using TEM, two in NWA 998 (FIB1, FIB2) and one in Nakhla (FIB3). FIB1 was cut parallel to the elongated direction of a cumulus, euhedral to subhedral apatite grain, ~25 x 80 μm in size, entirely included in Fe-rich pigeonite (Ap 7.3 in Fig. 2d). FIB2 was cut in a different subhedral to euhedral cumulus apatite grain in NWA 998, closely intergrown with titanomagnetite and Ca-rich pyroxene (Ap 5.2 in Fig. 2c). FIB3 was extracted in Nakhla, targeting a cluster of similarly oriented, acicular, intercumulus apatite grains within a mesostasis melt pocket (Fig. 3c).

Bright-field and dark-field S/TEM observations

FIB1, NWA 998 cumulus apatite. Transmission electron microscopy shows that apatite is present in the upper part of the FIB section, comprising about 65% of the FIB section area. Apatite consists of a single crystal with a few slightly misoriented subgrains, a few parallel, straight fractures (~0.2-0.5 μm-size) that crosscut the FIB section, which were filled with epoxy during thin section preparation, and some dislocations (Fig. 5a). The parallel nature of the fractures (parallel to the (111) plane), suggests that apatite develops fractures during shock within a preferential crystallographic direction, a feature that has been described in other minerals (e.g., Pittarello et al., 2020; Darling et al., 2021). The dislocations occur as elongated arrays, heterogeneously distributed, subparallel to the fractures (inset in Fig. 5a). Despite the

252 fractures and dislocations, the apatite within the FIB section looks homogeneous at the micron
253 scale. Energy dispersive X-ray analyses and diffraction patterns reveal that the lower part of the
254 FIB section consists of Fe-rich, Ca-poor pyroxene, consistent with pigeonite composition (Fig.
255 5a, Table 1), and the crystal is associated with a pore ~1.5-2 μm in size (Fig. 5a).
256 Dark-field STEM imaging in FIB1 also reveals compositional heterogeneities in the form
257 of mottled Z-contrast regions at the 5-10 nm scale (Fig. 6a). These regions consist of irregularly-
258 shaped domains with lower Z contrast, surrounded by continuous higher-Z regions. Although the
259 proportions of these two different domains are approximately equal throughout the FIB section,
260 we cannot rule out the possibility that these features were produced by beam damage.
261 **FIB2, NWA 998 cumulus apatite.** The general characteristics of FIB2 in cumulus
262 apatite 5.2 is described in Martínez (2021). Bright-field TEM and dark-field STEM images,
263 combined with diffraction patterns, reveal that apatite in FIB2 is a single crystal with a few
264 subgrains slightly misoriented relative to one another (Fig. 5b). SAED patterns indicate that the
265 apatite is oriented close to the *c* axis, the [011] zone axis. An exception is a small region (dashed
266 white rectangle in Fig. 5b) consisting of polycrystalline apatite (0.5 μm-size). Apatite in FIB2
267 appears mostly homogeneous with a few dislocations on the right-hand side of the FIB section, a
268 few subgrain boundaries, and curved cleavage on the (100) planes at 120° angles that show slight
269 curvature (Fig. 5b). A melt inclusion and a fragmented vein are also present in the FIB section.
270 **FIB3, Nakhla intercumulus apatites.** The FIB3 foil exhibits a complex structure with
271 four subhedral to euhedral apatite grains (3-5 μm size), numbered from 1 to 4 in Figure 5c.
272 Diffraction patterns show that the four grains are oriented perpendicular to the *c* axis (Fig. 5c,
273 inset). The four apatite grains exhibit similar shapes and sizes, their interiors are fracture free
274 except for apatite 4, which contains some fractures that crosscut the crystal, and the cleavage is

well distinguished in apatites 1 and 3. Apatite 3 has a rounded shape and is surrounded by radial nanoporosity and/or fractures (Fig. 6b). Bright-field TEM images show that apatites have strong contrast, indicative of significant strain. Z-contrast STEM imaging on apatite 3 also shows differences in contrast and the left-hand side of the grain shows growth layers (~20-50 nm wide each) that radiate away from a single point that probably represents the original nucleation site of the grain (Fig. 6c,d). Apatites 1 and 4 are embedded in crystalline phases (tridymite and alkali-rich feldspar with a composition of $Or_{61.3}Ab_{38.6}$) (Fig. 5c), and small regions of K-rich glass have also been identified in the FIB section (Figs. 5c, 6e,f). Apatites 2 and 3 are mostly embedded in a completely featureless material that appears to be amorphous, based on electron diffraction patterns, and is crosscut by a few veins (Figs. 5c, 6b,f). Qualitative TEM-EDS analyses of the amorphous material indicate it is almost pure SiO_2 with trace concentrations of Al_2O_3 (up to 0.9 wt%). Amorphous silica and K-, Na-rich feldspar constitute the groundmass between grains (Fig. 5c). In addition, small (~1 μm-size) crystals of tridymite with textures that suggest they were the last phases that crystallized in the melt pocket, are included in the K-, Na-rich feldspar (Fig. 6e). Tridymite is enclosed in shells of a low Z-contrast material that is too fine-grained to identify (Fig. 6e). The FIB section also contains clay minerals as a fibrous phase, a few nanometers in size, that STEM-EDS analyses show consists of K-, Fe-rich phyllosilicates with minor Cl (0.7–1.26 wt% Cl), consistent with a composition close to glauconite or illite (Martínez, 2021). Clay minerals have a sheet texture with nanocrystalline flakes arranged in clusters (Fig. 6f), occurring throughout the FIB section as veins, filling porosity, filling interstitial regions between grains (~40–600 nm in size), and surrounding other phases, such as tridymite and amorphous silica (Fig. 6e,f).

Nanostructures of NWA 998 and Nakhla apatites

298 Selected area diffraction patterns in FIB1, cut parallel to the elongated direction, and
299 FIB2, cut perpendicular to the elongation direction of the crystal show a diffuse streaking
300 parallel to the [111] direction (Fig. 5a, inset), and to the [313] direction (e.g., Fig. 5b, inset),
301 respectively. No streaking is observed in the SAEDs from FIB3 (Nakhla).
302 High-resolution TEM images of the homogeneous-looking single crystal apatites in the
303 three FIB sections (two in NWA 998 and one in Nakhla) reveal a domain structure at the 5-10
304 nm scale (Figs. 7 and 8). In FIB1 (NWA 998), HR-TEM images were taken parallel to the [1-21]
305 zone axis, and the observed domains could be attributable to the same domains seen with dark-
306 field STEM mentioned above (Fig. 6a). The domains are apparent from differences in the
307 contrast in the lattice fringes across domain boundaries, with each domain exhibiting a slight
308 crystallographic misorientation relative to one another (Fig. 7). These misorientations between
309 domains are apparent when viewing the HR-TEM images at a low angle to the page along the
310 lattice fringes. Lattice planes are continuous, but show distinct, slight curvature around the edges
311 of the domains, and narrow boundaries appear to distinguish one domain from another (Fig.
312 7a,b), which might be attributed to the presence of vacancies. These nanostructures are indicative
313 of highly localized strain within the structure. Thus, we attribute the streaking to the presence of
314 these strained domains that result in localized variability in the lattice parameters of the apatite
315 structure.
316 The domains in the single crystal apatite in FIB2 (NWA 998) are more variable (Fig. 7c)
317 than in FIB1 (NWA 998), and lattice planes in some areas show notably more curvature,
318 indicative of strong localized strain in the structure. The boundaries between the domains are
319 clearly continuous and hard to distinguish at close-up images (Fig. 7d,e). High-resolution TEM
320 imaging of the polycrystalline apatite from FIB2 (dashed rectangle in Fig. 5b) shows that some

grains have lattice fringes that are less well-defined than others i.e., some regions of the apatite are amorphous (Fig. 7f). Curvature of lattice fringes is much less apparent in Nakhla apatite (FIB3) but is nevertheless distinguishable in lattice fringes within the FIB section cut normal to the (001) direction (Fig. 8a,b). Some domains (a few 10s of nm in size) appear to be amorphous (Fig. 8c), and some areas exhibit the characteristic mottled Z-contrast (Fig. 8c), also seen in NWA 998 apatites (FIB1 and FIB2).

Apatite S/TEM-EDS compositions

Apatite compositions obtained by quantitative S/TEM-EDS analyses are plotted in Figure 4 and schematically represented in Figure 9, together with data from the literature for comparison. In FIB1 (NWA 998), apatite has slightly more chlorine (2.40 wt% average) than F (1.90 wt% average) (Cl/F = 1.26, Table 1), and REE concentrations are below detection levels. Apatite compositions in FIB2 (NWA 998) show some variability in the FIB section, ranging from 1.26 to 1.57 wt% F and from 2.91 to 3.59 wt% Cl (Table 2/ Table 1 in the melt inclusion paper), with an average Cl/F ratio of 2.23 (wt%), slightly Cl-enriched compared to FIB1. The polycrystalline apatite (dashed rectangle in Fig. 5b) has a Cl/F ratio of 5.14 (Table 2) distinct from the single crystal apatite. Silica content in the different areas of FIB1 is variable, ranging from 0.79 to 3.12 wt% SiO_2 (Table 1). In a Si versus Ca/P (atomic %) plot (Fig. 10), the overall positive correlation indicates that some silica could be bonded in the apatite structure. However, given that (1) substitution in apatite involving Si for P include REE for Ca (Pan and Fleet, 2002), and (2) REEs are below detection limits in all the analyses (Table 2), we conclude that Si is most likely hosted in another phase (e.g., ellestadite, Brounce et al., 2022).

TEM-EDS analyses on apatite 3 in FIB3 (Nakhla) show zonation of halogens (Table 3), where Cl content is lower in the core (4.47 wt%), higher at the rim (5.50 wt%), and inversely

correlated with F (0.62 wt% in the core and 0.20 wt% at the rim). Rare-earth elements are also higher in the core (0.55 wt% Ce_2O_3 and 0.33 wt% Nd_2O_3) than the rim (0.13 wt% Ce_2O_3 and 0.05 wt% Nd_2O_3). Iron and SiO_2 show zonation with the same trend, ranging from 0.44 wt% FeO in the core to 0.14 wt% FeO at the rim, and 5.16 wt% SiO_2 in the core to 3.42 wt% SiO_2 at the rim in this grain, ruling out contamination from adjacent feldspar. In fact, silica is variable between and within grains, and is also positively correlated with the Ca/P ratio (Fig. 10b). In general, SiO_2 contents from the four apatite grains are higher than in NWA 998, ranging from ~2.48 to 5.93 wt% (Table 3). The four studied apatites in Nakhla contain trace, variable amounts of REEs (up to 0.59 wt% Ce_2O_3 and 0.33 wt% Nd_2O_3). Overall, the F and Cl contents vary significantly from grain to grain and even within grains and have higher wt% Cl/F ratios (1.55 - 27.50) than NWA 998 apatites. Halogens range from 0.2 to 1.9 wt% for F, with a mean of 0.95 wt% F, and from 2.9 to 5.5 wt% Cl, with a mean of 4.02 wt% Cl (Table 3). This is broadly consistent with previous reports of apatite compositions in Nakhla (e.g., McCubbin et al., 2013; Brounce et al., 2022; Figs. 4, 9).

DISCUSSION

The nakhlites are cumulate rocks from Mars considered to derive from a shallow level magma body or a thick lava flow (e.g., Harvey and McSween, 1992; Lentz et al., 1999; Mikouchi et al., 2006; Treiman, 2005, Beck et al., 2006; Day et al., 2006; Treiman and Irving, 2008), although recent studies support multiple flows or hypabyssal intrusions (Hewins et al., 2020) or a co-genetic plumbing system for the chassignites-nakhlites (Udry and Day, 2018). Chassignites and nakhlites have been petrologically linked to the same magmatic system (Jagoutz, 1991; Nyquist et al., 2001; Eugster et al., 2002; Eugster, 2003; Marti and Mathew, 2004; Bogard and Garrison, 2008; Park et al., 2009; Carlson and Boyet, 2009; Korochantseva et

al., 2011), and several nakhlites (NWA 817, MIL 03346/ 090039/ 090032/ 090136, and NWA 5790) may record the eruptive event (e.g., Day et al., 2006).

Apatites in the chassignites and nakhlites exhibit large variations in Cl content and isotope compositions between grains and smaller variations within grains. This observation leads to the question of whether the martian interior contains a major volatile reservoir, or the observed variations are the result of the interaction of the magma with fluids or sediments from the country rock, leading to disequilibrium conditions. There has been reported evidence that suggests that the nakhlite magma body experienced at least two interactions with hydrothermal fluids (Gooding et al., 1991). One fluid/rock interaction occurred with a magmatic hydrothermal fluid exsolved from the nakhlite magma body during cooling once the magma reached chloride saturation (McCubbin et al., 2013; Brounce et al., 2022), and the second involved a later, shallower, aqueous brine resulting from an impact adjacent to the nakhlite parent rocks that formed secondary, low-temperature minerals (Ashworth and Hutchison, 1975; Newsom, 1980; Gooding et al., 1991; Abramov and Kring, 2005; Changela and Bridges, 2010; Bridges and Schwenzer, 2012; Hicks et al., 2014; Lee et al., 2015).

Apatite textures and compositions in the nakhlites have been used to reconstruct their magmatic and subsolidus histories and to better understand volatile reservoirs, their interactions, and their behavior in the martian crust and mantle (e.g., McCubbin and Nekvasil, 2008; McCubbin et al., 2013; Brounce et al., 2022). However, it is clear from our observations that apatite grains in the nakhlites reflect a complex record of both magmatic and subsolidus processes and that extracting petrogenetic and volatile records are difficult and fraught with interpretive issues. For these reasons, examining apatite at the submicron scale provides valuable insights into this complex thermal, geochemical, and volatile history, and can help resolve the

important question of whether basalts can be used as reliable windows into the volatile geochemistry of the martian mantle.

In the following sections, we discuss the complex microstructures observed in NWA 998 and Nakhla apatites that have not been described before: domain structures at the nanoscale, Z-contrast differences at the nanoscale, zonation of halogens and REEs, and regions of an amorphous phase in Nakhla apatite. The understanding of submicron-sized structures in apatite can help discern between the four proposed models to explain the geochemical signatures of the chassignites-nakhlites: (1) mantle-derived magmas with no crustal component (e.g., Jones, 1989; Longhi, 1991), (2) assimilation of a crustal, volatile-rich component by mantle-derived magmas during crystallization, such as soil (e.g., Sautter et al., 2006; Usui et al., 2012; Shearer et al., 2018) or a fluid-phase (e.g., McCubbin and Nekvasil, 2008; McCubbin et al,, 2013), and (3) near solidus or subsolidus metasomatism (e.g., Treiman et al., 2007).

Implications for nanostructural domains in ternary solid-solution apatites: Primary subsolidus signatures and the importance of vacancies in the missing component

Different characteristics of the domain structures are observed in apatite at the nanoscale, by dark-field STEM and high-resolution TEM. Dark-field STEM (Fig. 6a) reveals differences in composition between the domains and HR-TEM (Figs. 7, 8) demonstrates the presence of localized strain. The domain structure seen with HR-TEM is defined by slight differences in contrast and undulosity in lattice fringes, related to localized changes in orientation of the crystal relative to the incident beam. Northwest Africa 998 apatite displays a much higher degree of undulosity of the lattice fringes (Fig. 7c) compared to Nakhla apatite (Fig. 8). The boundaries between the domains in HR-TEM images are sharp and are defined by distinct differences in contrast between the lattice fringes in each domain (Fig. 7). However, the lattice fringes are

continuous across the domain boundary indicating that the slight misorientation between the different domains is completely accommodated by elastic strain in the structure (Fig. 7d,e). The strain is likely to be highest at these boundaries, but the mismatch is not sufficiently high to have resulted in the formation of dislocations to accommodate the strain. The domain texture seen with dark-field STEM in NWA 998 apatite indicates compositional differences between the domains and might be due to the differences in the concentration of the two halogens, F and Cl. However, EFTEM imaging and EELS spectra were not sufficient to determine that Cl and F segregation are responsible for these domains (Fig. 8d). Nonetheless, the fact that the nanostructural domains observed with STEM are at the same scale (5-10 nm) as HR-TEM domains suggest that the localized strain in the crystal caused by the differences in orientations of the nanodomains are related to differences in compositions.

A possible explanation for these phenomena can be understood by a consideration of the crystal structure of apatite, particularly, the location of the halogens. The apatite crystal structure ($P6_3/m$) consists of three cation polyhedra: the rigid PO_4 polyhedra, which remain invariant with the different halogens, the $Ca(1)O_9$ tricapped trigonal prism, which has little response to variations in F, Cl, and OH concentrations, and the $Ca(2)O_5X(O)$ polyhedron (X=F, Cl, OH), which experiences the major structural response due to anion substitution, because it is bonded to the anion column (Hughes et al., 1989; Hughes and Rakovan, 2002). Fluoride, Cl^-, and OH^- ions are located inside the channels that create the arrangement of planar triangles of Ca(2) atoms at z=1/4 and z=3/4 by the hexagonal screw 6_3, perpendicular to the c axis. However, experiments on synthetic apatites by nuclear magnetic resonance (NMR) spectroscopy and synchrotron-based single-crystal X-ray diffraction (SCXRD) demonstrate that OH-poor to OH-free synthetic apatites with a variety of F and Cl substitutions in the halogen column result in complex

structural variations (McCubbin et al., 2008; Schettler et al., 2011; Hughes et al., 2014; Vaughn et al., 2015). For example, in OH-free apatites, the interaction of F with large Cl atoms creates an additional off-mirror F site at (0,0,0.167) (aside from the (0,0,1/4) site) (Hughes et al., 2014) that is coupled with a relaxed Cl site at (0,0,0.59). About 92% of the total Cl atoms are accommodated in the relaxed Cl site and the remaining 8% are located at (0,0,0), allowing sufficient F-Cl distances to maintain the solid solution (Hughes et al., 2014). Schettler et al. (2011) also showed that the Ca(2) site splits into two distinct sites (Ca2A and Ca2B for F and Cl, respectively) and that their positions are a function of the halogen content. In addition, experiments have shown that the small oxyapatite component (plus vacancies) in the structure allows the long-range neighboring of F and Cl within the anion channels and maintains the hexagonal structure (McCubbin et al., 2008; Schettler et al., 2011). Neither of these positions have been observed in any natural apatite so far. In NWA 998 and Nakhla apatites, F and Cl are in solid solution among the anion column, thus the coordinated cation Ca(2) creates two different sites, one for F and OH if present (Ca2A), and one for shifted Cl (Ca2B), enabling the optimum Ca-Cl bond distance to be maintained (Bauer and Klee, 1993; Schettler et al., 2011; Hughes et al., 2014). In pure chlorapatite and hydroxyapatite, the mirror plane symmetry disappears because Cl or OH arrange above or below the mirror plane, forcing the structure to order and becoming monoclinic ($P2_1/b$). However, in most natural samples, the hexagonal $P6_3/m$ symmetry is preserved because each mirror-related plane is half-occupied, or there are enough vacancies (in chlorapatite) or impurities (F ions in hydroxyapatite) in the anion column to destroy the ordering (Sudarsanan and Young, 1969; Elliott et al., 1973; Hughes and Rakovan, 2002; McCubbin et al., 2008; Schettler et al., 2011). It is likely that some apatite compositions in Nakhla, for example, extremely Cl-rich and F-poor (Cl/F ratio up to 27.5, Table 3, Fig. 4), preserve the hexagonal

459 structure (Fig. 8a,b) due to the presence of vacancies in the structure (besides OH), which are
460 discussed below. Ordering in the Ca and P sites when other elements substitute (e.g., Si in the P
461 site or REEs in Ca sites) result in a variety of different structural responses that are not well
462 characterized yet (e.g., McConnell, 1973; Hughes et al., 1991; Hughes and Rakovan, 2002; Kelly
463 et al., 2017).

464 We suggest that the domain structures observed in NWA 998 and Nakhla are the result of
465 a nanoscale segregation (exsolution) of the halogens into distinct F- and Cl-rich domains, which
466 have different unit cell parameters (a=9.598Å; vol. 543Å^3 Cl-apatite, c.f. 9.3973Å; vol. 523Å^3 F-
467 apatite, Hughes et al., 1989). Although the volume difference between the endmembers is only
468 ~1%, it may be sufficient to cause lattice strain between F- and Cl-rich domains. This
469 assumption seems reasonable given that Cl is 36% larger than F, resulting in disordering of Cl in
470 the halogen column, due to its displacement 1.2 Å above and below the mirror plane (Hounslow
471 and Chao, 1968; Hughes et al., 1989). This conclusion is further supported by the fact that the
472 domain structures observed in NWA 998 and Nakhla are not observed in apatite from lunar
473 basalts (Martínez et al., 2020), which is predominantly fluorapatite and displays a uniform
474 nanostructure. We rule out that these domains are caused by REEs given that the concentration
475 of REEs in NWA 998 is below detection limits, whereas the REE abundances in Nakhla apatites
476 are high (Table 3), but NWA 998 apatite shows a higher number of domains and more strain
477 (undulosity of the lattice fringes) within the structure compared to Nakhla (Figs. 7, 8).

478 The highly undulous lattice fringes in NWA 998 apatite observed with HR-TEM (larger
479 lattice strain) compared to Nakhla is ascribed to the distinct Cl/F ratios (1.75 average of NWA
480 998 apatites, versus 4.23 average of Nakhla apatites, Tables 1, 2, 3, Fig. 9). More similar F and
481 Cl contents may result in a higher abundance of domains with different Cl/F ratios caused by the

unmixing process of the two halogens. When Cl dominates the apatite structure, as seen in Nakhla, the domain abundance diminishes (Fig. 8a,b). The *a* and *b* directions are the most affected by changes in the halogen column, since the twist angle of the CaO_6 metaprisms (which are connected with the PO_4 tetrahedron) is highly sensitive to composition and the twist angle increases or decreases to satisfy the CaO_6X polyhedra bonding requirements (White et al., 2005). Thus, the halogen channel expands or contracts perpendicular to the basal plane, consistent with the direction of undulosity obtained from HR-TEM, the [100] direction (Fig. 7c). FIB2 (NWA 998) and FIB3 (Nakhla), sliced perpendicular (or close to perpendicular) to the crystallographic *c* axis, exhibit the most favorable crystallographic orientation for lattice mismatches. In addition, diffraction patterns from NWA 998 apatite show diffuse streaking along the [111] and [313] directions (Fig. 5a,b), ascribed to inter-channel disorder between Cl and F ions (Ferraris et al., 2005). The optimal phase boundaries for different compositional domains form between lattice planes in F- and Cl-apatite domains with the lowest lattice mismatch, (111) and (313) being two of them.

A domain structure caused by phase separation at the nanometer scale has previously been observed in apatite by Ferraris et al. (2005). This study found a complex nanostructure in apatite when viewed along the [100] direction (*c* axis) defined by differences in contrast and beam sensitivity in HR-TEM at two scales that differ by an order of magnitude. At the larger scale, guest apatite was observed as irregularly-shaped regions of a darker contrast in BF-TEM images amidst host-apatite, consistent with Cl- and F-rich apatites, respectively (Ferraris et al., 2005). At a smaller order of magnitude, bright areas 5-10 nm in diameter with poorly defined hexagonal facets were identified as ellestadite, a monoclinic apatite variety with formula $Ca_5(SiO_4,PO_4,SO_4)_3(F,Cl,OH)$. Both host and guest apatites have similar *c* but distinct *a*

parameters and their interfaces are coherent with possible lattice mismatch to preserve coherency of domains with sizes of ~15 nm. Ferraris et al. (2005) concluded that F- and Cl-bearing apatite is thermodynamically unstable as a single phase and that spinodal decomposition produced continuous growth of two phases during cooling. The authors also distinguished two geothermometric events: a first, long, kinetically-driven phase separation close to the coherent spinodal decomposition temperature, which caused unmixing into F- and Cl-rich apatite domains; and a second, short, diffusion-dependent period at a slightly higher temperature (contact metamorphism) that generated ellestadite domains.

The nanoscale exsolution domains observed in the present work have not been reported previously in any F-Cl-OH apatite. Crystallographic studies by Hughes et al. (1989) on three near endmember apatites demonstrate that the structural configurations of the column anions (F, Cl, OH) are not miscible. The authors argued that for a binary apatite with composition $Ca_5(PO_4)_3(OH_{0.5}Cl_{0.5})$, each of the OH or F sites would be one-fourth occupied by its respective occupant, OH or Cl, and the same would happen with ternary apatites. Hence, anion-anion distances calculated by Hughes et al. (1989) for column anions using end-member data precludes such a disordered $P6_3/m$ arrangement. Nonetheless, recent studies dedicated to understanding the non-ideal mixing of F and Cl along the F-Cl apatite binary join on synthetic apatites using NMR and SCXRD techniques have demonstrated that there are possible ways anionic mixing within apatite channels is feasible (McCubbin et al., 2008; Schettler et al., 2011; Hughes et al., 2014, Vaughn et al., 2015). These studies infer that hydroxyl groups may play an important role in stabilizing the hexagonal structure, because ordering can occur within single columns but not among different anion columns (Hughes et al., 1989; Pan and Fleet, 2002), and point towards the importance of vacancies in precluding the formation of a miscibility gap (e.g., Hughes and

Rakovan, 2002; Hovis and Harlov, 2010; Schettler et al., 2011; Hughes et al., 2014; McCubbin and Ustunisik, 2018). Indeed, Schettler et al. (2011) experimentally showed that the only possible way to stabilize hexagonal endmember chlorapatite is by the presence of vacancies. Hughes et al. (1989) also predicted that although the overall near endmember chlorapatite preserves the $P6_3/m$ symmetry, the structure may contain short-range regions with Cl clusters ordered above or below the plane in a given column (local ordering), which was demonstrated by McCubbin et al. (2008) in synthetic apatite experiments by SCXRD and NMR spectroscopy.

As discussed above, binary and ternary apatites respond to solid solution by large shifts of anion positions relative to the endmembers, by reduction of symmetry to monoclinic (Hughes et al., 1989; Schettler et al., 2011; Hughes et al., 2014), or by the presence of anion vacancies (Hughes and Rakovan, 2002). The fact that NWA 998 apatites have the highest missing component abundances, commonly higher than 30 mol% (Fig. 4), but only 0.07 to 0.11 wt% water has been measured in NWA 998 apatite by SIMS (Channon, 2013), suggests that vacancies are present as an important part of the missing component. Our results show that the hexagonal symmetry is maintained, hence indicating that large displacements of anion positions likely occur, and/or that vacancies are present, which may be located at the boundary between domains, seen as blurry but coherent interfaces, separating clusters of Cl, F, and/or OH anions (Figs. 7d,e, 8c). An important implication is thus that when OH is derived by stoichiometry when using EPMA analyses in martian nakhlites, the result is likely overestimated.

The coherent interfaces between the different domains (the lattice remains continuous across the boundary between the domains) are consistent with the Ferraris et al. (2005) observations, indicating that strain between the domains was small enough to be accommodated by elastic strain. The fact that the domain sizes are very small (5-10 nm) and coherent indicate

551 that either the domains formed at low temperature (~600 ºC) or that the cooling rate was fast,
552 preventing coarsening and formation of interfacial dislocations and/or semicoherent interfaces
553 between the domains. This is consistent with subsolidus cooling rates calculated by Mikouchi
554 and Miyamoto (2002) for the nakhlites, based on chemical zoning profiles (Fe-Mg and Ca) in
555 olivine cores and assuming cooling started at 1100ºC. The authors also noted that Nakhla
556 exhibits irregular Ca-zoning profiles in olivines, suggesting a more complex crystallization
557 history than other nakhlites (Mikouchi and Miyamoto, 2002). Recent work by Hovis and Harlov
558 (2010) and McCubbin and Ustunisik (2018) showed that there is stronger non-ideal mixing along
559 the F-Cl join in apatite compared to the F-OH or Cl-OH joins and demonstrated that, in binary F-
560 Cl apatites, F becomes more compatible in apatite as there is less F in the system because apatite
561 solid-solution stability depends on the occupancy of the F off-mirror site determined by Hughes
562 et al. (2014). Finally, Li and Costa (2020) showed that, at magmatic temperatures higher than
563 800-1250 ºC, the calculated W^G values are not high enough to produce a miscibility gap in
564 ternary apatite. If the microstructures seen in NWA 998 and Nakhla indeed record miscibility
565 gaps between F and Cl, then the apatite in NWA 998 had to form at lower temperatures (less
566 than 800 ºC), consistent with the discussion above. Less likely, if apatite formed above 800 ºC
567 (above the miscibility gap), the exsolution had to form at a temperature lower than 800 ºC. In
568 addition, vacancies were essential in stabilizing ternary apatites and eliminating a miscibility gap
569 at high temperatures.

570 **Implications for nanostructures in Nakhla apatites**

571 Apatite plays a critical role in understanding the magmatic system on Mars and can
572 provide additional insights into the sources of volatiles. Apatite is widely used as a petrogenetic
573 indicator because the F-Cl-OH ratio in apatite varies proportionally with the F-Cl-OH ratio of the

melt from which it crystallizes, reflecting the role of volatiles in the system. However, the halogen and hydroxyl contents of apatite do not represent the F-Cl-OH ratio of the parental fluid or melt (Piccoli and Candela, 2002; Boyce et al., 2014). Experimental studies on apatite melt-partitioning reveal that apatite prefers F over Cl, and Cl over OH (Stormer and Carmichael, 1971; Mathez and Webster, 2005; Boyce et al., 2014; McCubbin et al., 2015).

The volatile chemistry of apatite in the nakhlites is complex and has led to several different hypotheses to explain their volatile chemistry: an enriched mantle source, crustal assimilation, interaction of a fluid during basalt crystallization, and near subsolidus metasomatism of a crystallized basalt. In the following section, we discuss the microstructures and compositions of the four intercumulus apatite grains analyzed in Nakhla by TEM to evaluate which of the four petrogenetic models the observations support best.

TEM-EDS analyses show that the four apatite grains in FIB3 (Nakhla) exhibit large variations in Cl and F contents (Cl ranging from 2.82 to 4.83 wt%, F ranging from 0.09 to 1.43 wt%, Table 3), consistent within the range obtained by EPMA by McCubbin et al. (2013) (Figs. 4, 9). Ascribing these variations, which are also apparent within individual grains, simply by fractional crystallization is not sufficient, given the large range of these variations. The recently discovered ferroan chassignite NWA 8694 also requires a more complex process to crystallize olivine as ferroan as in NWA 8694 (Fo_{54}), and magma mixing has been proposed as a possible explanation (Hewins et al., 2020). In addition, apatite δD values in Nakhla are much lower than some of the clay-like alteration assemblage δD values, indicating that the majority of OH in Nakhla apatites is not derived from martian atmospheric water (Hallis et al., 2012). Instead, the wide compositional variability might be attributable to assimilation of crustal evaporitic sediments (Sautter et al., 2006) or fluids (McCubbin et al., 2013) during crystallization, and/or

disequilibrium due to outgassing of the residual melt (Potts, 2017). Based on the following arguments, we support a model based on assimilation of crustal sediments in a Cl-rich melt that experienced degassing:

1) Nakhla apatites are intercumulus minerals formed after ~95% melt solidification. Therefore, they are affected by degassing of the interstitial late-stage melts, influencing the F-Cl-OH contents in apatite (Potts, 2017). On the contrary, NWA 998 apatites show similar Cl/F ratios and their REE contents are below detection limits, indicating that they crystallized earlier in the paragenetic sequence (i.e., as a cumulus phase, McCubbin et al., 2013). We argue that differentiated, late-stage residual melt pockets were first connected to each other (open system), hence mineral assemblages did not grow in local equilibrium but were connected to the larger cumulus pile, sensitive to changes in composition of the overall system. However, at a very late stage of crystallization, it is possible that the different melt pockets became isolated from one another, leading to distinct chemical evolution of the different mesostasis pockets within a single sample and within the same melt pocket, seen by the small scale at which compositional variations in Nakhla apatites occur (i.e., Cl/F ratios are different in each grain in the FIB section; Table 3). Degassing of the residual melt (e.g., Sautter et al., 2006) or degassing of a Cl-rich fluid after the melt reached chloride saturation (McCubbin et al., 2013) is recorded by a change in the oxidation state of S in apatite (Brounce et al., 2022), but it probably affected Nakhla apatites up to a certain point, because at the very end stage, they became isolated and their chemistry reflects local equilibrium within very small melt pockets.
2) The textural occurrence of apatite 3 (Nakhla), cut perpendicular to the *c* axis and exhibiting a nucleation region with subsequent layers of growth, provides an opportunity

620 to learn about the evolution of the melt during apatite crystallization (Fig. 6c,d). Although
621 STEM X-ray maps of Cl *Kα* for apatite 3 (not shown) do not show compositional
622 heterogeneities within the grain, TEM-EDS analyses of this grain show zonation of
623 elements, where F, REEs, Si, and Fe are higher in the core, while Cl content increases
624 towards the rim. The observed increase of Cl/F ratio with progressive crystallization is
625 consistent with sequential crystallization from a melt that was becoming Cl-enriched
626 through time due to preferential F incorporated into the apatite structure mentioned
627 above. Rare-Earth Elements decrease from core to rim, also characteristic of apatite
628 crystallizing from a late-stage melt (Jolliff et al., 1993).
629 3) There is no evidence of subsolidus equilibration which would have erased the very fine
630 scale zonation, indicating that apatites grew and cooled rapidly, consistent with their
631 habits (Fig. 3). The fact that apatite preserves zonation in Fe is particularly strong
632 evidence of minimal subsolidus equilibration, given that Fe and Mg equilibrate more
633 readily than REEs in phosphates (Hess et al., 1990).
634 4) High-resolution TEM imaging shows that the crystal structure of Nakhla apatite is highly
635 heterogeneous. Some images show minimal variations in contrast indicative of low strain
636 and the high level of crystallinity is apparent from the hexagonal configuration of apatite
637 structure viewed down the *c*-axis with straight lattice fringes (Fig. 8a). Other areas show
638 higher contrast differences and slightly curvature of the lattice fringes in the (010) plane
639 (Fig. 8b). We infer that these heterogeneities are caused by compositional variations (e.g.,
640 F/Cl differences and/or REEs, Table 3). As discussed above, these differences in contrast
641 are caused by the segregation into F- and Cl-rich domains, which is a primary feature that
642 developed during initial post-magmatic cooling, immediately when apatite started to cool

down < 800 ºC (see Mikouchi and Miyamoto, 2002). Areas that show more complexity in the structure due to slight amorphization might be indicative of post-magmatic fluid interaction (Fig. 8c). Other signatures of post-magmatic fluid interaction in the FIB section are evident, such as the presence of clay minerals filling porosity or veins outlining other mineral phases (Figs. 5c, 6b,e,f), or the amorphization of tridymite (Figs. 5c, 6f). However, fluids do not seem to have affected most of the primary apatite. Phyllosilicates (saponite, serpentine, hydrous minerals from the iddingsite group, and berthierine) or clay-like vein assemblages (commonly refer as 'iddingsite' veins) are well documented in Nakhla and other nakhlites, formed as a result of the interaction of the nakhlite basalt with hydrothermal aqueous fluids at the surface and near subsurface of Mars (e.g., Ashworth and Hutchison, 1975; Gooding et al., 1991; Bridges et al., 2001; Gillet et al., 2002; McCubbin et al., 2013; Muttik et al., 2014; Lee et al., 2015; Lee and Chatzitheodoridis, 2016) or as products of terrestrial alteration (Hicks et al., 2014). Therefore, although the intercumulus melt in which apatites are found has evidence of a late, post-magmatic fluid interaction, apatites been affected minimally by these processes. Hence, we infer that their original primary magmatic compositional and microtextural characteristics are preserved.

Therefore, given that (i) different apatites that are only a few microns apart in the same melt pocket show large variability of Cl/F (wt%) ratios (Table 3, Figs. 4, 9), (ii) the zonation in apatite 3 is consistent with late-stage crystallization from a melt (Fig. 6d), (iii) the heterogeneities in the nanostructure of apatite are variable (Fig. 8), and (iv) there is no evidence of a fluid phase interaction during apatite crystallization, we conclude that the studied Nakhla apatites crystallized from a melt that experienced degassing and mechanical mixing with crustal

666 sediments (Potts 2017; Sautter et al., 2006). Post-magmatic aqueous alteration by a superficial
667 fluid is evident (e.g., presence of clay minerals), but did not affect the primary characteristics of
668 apatite.

669 **CONCLUSIONS**

670 We have observed a domain structure at the 5-10 nm scale in the studied apatites in both
671 NWA 998 and Nakhla. The domain structure is characterized by high undulosity of the lattice
672 fringes and differences in contrast, which are indicative of elastic strain and small, highly
673 localized misorientations in the crystal. The domain structure is significant and ubiquitous in the
674 microstructure of NWA 998 apatites, whereas in Nakhla apatites it is very heterogeneous: some
675 areas show low strain and low contrast, while other areas show curvature of the lattice fringes in
676 the (010) planes. The lack of dislocations, the coherent interfaces, together with the
677 understanding of the apatite crystal structure suggest that these domains are related to halogen
678 segregation (Cl clusters ordered within the apatite structure) at low temperatures (< 800 ºC). The
679 diffuse coherent interfaces between the domains are interpreted as vacancies within the halogen
680 column, which are believed to play an essential role in stabilizing ternary apatites in NWA 998
681 and Nakhla, especially when Cl/F ratios in apatite are closer to 1. These observed nanostructural
682 domains are a post-magmatic signature that formed during the initial subsolidus cooling (primary
683 feature). Later, post-magmatic surface aqueous brines interacted with the mesostasis regions
684 (e.g., presence of phyllosilicates) but had minimal effect on the primary magmatic apatites.
685 Evidence of this post-magmatic fluid interaction in the bulk apatite are seen as slight amorphized
686 regions in one of the apatite grains studied.

687 This is the first study that has used FIB-TEM techniques in significant detail to observe
688 nanostructures on weakly shocked apatite grains and therefore, some features are reported here

689 for the first time, such as the observed chemical zoning in Nakhla apatites. Nonetheless, they
690 might be more common than previously recognized, because EPMA or SEM-EDS analyses
691 cannot detect such small-scale variations. The large variations in Cl/F ratios between and within
692 grains that are only a few microns apart are consistent with crystallization from a late-stage melt
693 that experienced degassing (degassing affected the F-Cl-OH contents of apatite grains) and
694 mixing of different materials that introduced Cl into the melt. Apatite 3 exhibits zonation of
695 elements (the core contains higher F, REEs, Si, and Fe, and the rim is Cl-enriched) that is
696 characteristic of crystallization from a late-stage melt and is inconsistent with the presence of a
697 fluid. At the very late stages of crystallization, as different melt pockets reduced in size, chemical
698 communication between them ceased, and apatites within individual melt pockets grew under
699 very localized equilibrium conditions.

700 In conclusion, this work may influence the way we interpret apatite chemistry in
701 planetary samples and demonstrates that there are fundamental challenges to calculating the
702 amount of water by stoichiometry using the subtraction of OH by assuming F+Cl+OH = 1. This
703 is not a straightforward process, as vacancies are likely to play an important role in the apatite
704 structure as they can reduce the miscibility gap of ternary apatites upon cooling.

705 **ACKNOWLEDGEMENTS**

706 We would like to thank Ying-Bing Jiang and Elena Dobrica for their help with the TEM.
707 Electron Microscopy and Electron Microprobe Analysis were performed in the Electron
708 Microbeam Analysis Facility at the University of New Mexico, a facility that is funded by the
709 National Science Foundation, NASA, and the state of New Mexico. We thank F. M. McCubbin,
710 an Anonymous Reviewer, C. Ferraris, and the Associate Editor Anne Peslier for insightful

comments, which helped improve the quality of this manuscript. This work was supported and funded by NASA Cosmochemistry Grant NNX15AD28G to A. J. Brearley.

REFERENCES CITED

Abramov, O. and Kring, D.A. 2005. Impact-induced hydrothermal activity on early Mars. Journal of Geophysical Research, Planets, 110, E12.

Aiuppa, A., Baker, D.R., and Webster, J.D. 2009. Halogens in volcanic systems. Chemical Geology, 263, 1–18.

Ashworth, J.R. and Hutchison, R. 1975. Water in non-carbonaceous stony meteorites. Nature, 256, 714–715.

Barnes, J.J., McCubbin, F.M., Santos, A.R., Day, J.M.D., Boyce, J.W., Schwenzer, S.P., Ott, U., Franchi, I.A., Messenger, S., Anand, M., and Agee, C.B. 2020. Multiple early-formed water reservoirs in the interior of Mars. Nature Geoscience 13, 260–264.

Barrett, T.J., Černok, A., Degli-Alessandrini, G., Zhao, X., Anand, M., Franchi, I.A., and Darling, J.R. 2021. Exploring relationships between shock-induced microstructures and H_2O and Cl in apatite grains from eucrite meteorites. Geochimica et Cosmochimica Acta 302, 120–140.

Bauer, M. and Klee, W.E. 1993. The monoclinic-hexagonal phase transition in chlorapatite. European Journal of Mineralogy, 5, 307–316.

Beck, P., Barrat, J.A., Gillet, P., Wadhwa, M., Franchi, I.A., Greenwood, R.C., Bohn, M., Cotten, J., van de Moortèle, B. and Reynard, B. 2006. Petrography and geochemistry of the chassignite Northwest Africa 2737 (NWA 2737). Geochimica et Cosmochimica Acta, 70, 2127–2139.

Birski, Ł., Słaby, E., Chatzitheodoridis, E., Wirth, R., Majzner, K., Kozub-Budzyń, G.A., Sláma, J., Liszewska, K., Kocjan, I., and Zagórska, A. 2019. Apatite from NWA 10153 and NWA 10645—The key to deciphering magmatic and fluid evolution history in nakhlites. Minerals, 9, 695.

Bogard, D.D. and Garrison, D.H. 2008. ^{39}Ar–^{40}Ar age and thermal history of Martian dunite NWA 2737. Earth and Planetary Science Letters, 273, 386–392.

Boyce, J.W., Tomlinson, S.M., McCubbin, F.M., Greenwood, J.P., and Treiman, A. H. 2014. The lunar apatite paradox. Science, 344, 400–402.

Bridges, J.C. and Grady, M.M. 1999. A halite-siderite-anhydrite-chlorapatite assemblage in Nakhla: Mineralogical evidence for evaporites on Mars. Meteoritics & Planetary Science, 34, 407–415.

Bridges, J.C. and Grady, M.M. 2000. Evaporite mineral assemblages in the nakhlite (martian) meteorites. Earth and Planetary Science Letters, 176, 267–279.

Bridges, J.C. and Schwenzer, S.P. 2012. The nakhlite hydrothermal brine on Mars. Earth and Planetary Science Letters, 359, 117–123.

Bridges, J.C., Catling, D.C., Saxton, J.M., Swindle, T.D., Lyon, I.C., and Grady, M.M. 2001. Alteration assemblages in Martian meteorites: Implications for near-surface processes. Space Science Reviews, 96, 365–392.

Brounce, M., Boyce, J.W., and McCubbin, F.M. 2022. Sulfur in apatite from the Nakhla meteorite record a late-stage oxidation event. Earth and Planetary Science Letters, 595, 117784.

Bunch, T.E. and Reid, A.M. 1975. The nakhlites Part I: Petrography and mineral chemistry. Meteoritics, 10, 303–315.

Carlson, R.W. and Boyet, M. 2009. Short-lived radionuclides as monitors of early crust–mantle differentiation on the terrestrial planets. Earth and Planetary Science Letters, 279, 147–156.

Cartwright, J.A., Gilmour, J.D., and Burgess, R. 2013. Martian fluid and Martian weathering signatures identified in Nakhla, NWA 998 and MIL 03346 by halogen and noble gas analysis. Geochimica et Cosmochimica Acta, 105, 255–293.

Černok, A., White, L.F., Darling, J., Dunlop, J., and Anand, M. 2019. Shock-induced microtextures in lunar apatite and merrillite. Meteoritics & Planetary Science, 1262–1282.

Changela, H.G. and Bridges, J.C. 2010. Alteration assemblages in the nakhlites: Variation with depth on Mars. Meteoritics & Planetary Science, 45, 1847–1867.

Channon, M.B. 2013. Oxygen isotopes and volatiles in Martian meteorite. Doctoral dissertation, California Institute of Technology.

Darling, J.R., White, L.F., Kizovski, T., Černok, A., Moser, D.E., Tait, K.T., Dunlop, J., Langelier, B., Douglas, J.O., Zhao, X., Franchi, I.A. and Anand, M. 2021. The shocking state of apatite and merrillite in shergottite Northwest Africa 5298 and extreme nanoscale

chlorine isotope variability revealed by atom probe tomography. Geochimica et Cosmochimica Acta 293, 422–437.

Day, J., Taylor, L.A., Floss, C., and McSween, H. Y. 2006. Petrology and chemistry of MIL 03346 and its significance in understanding the petrogenesis of nakhlites on Mars. Meteoritics & Planetary Science, 41, 581–606.

Elliott, J.C., Mackie, P.E., and Young, R.A. 1973. Monoclinic hydroxyapatite. Science, 180, 1055–1057.

Eugster, O. 2003. Cosmic-ray exposure ages of meteorites and lunar rocks and their significance. Chemie der Erde-Geochemistry, 63, 3–30.

Eugster, O., Busemann, H., Lorenzetti, S., and Terribilini, D. 2002. Ejection ages from krypton-81-krypton-83 dating and pre-atmospheric sizes of martian meteorites. Meteoritics & Planetary Science, 37, 1345–1360.

Ferraris, C., White, T.J., Plévert, J., and Wegner, R. 2005. Nanometric modulation in apatite. Physics and Chemistry of Minerals, 32, 485–492.

Giesting, P.A. and Filiberto, J. 2016. The formation environment of potassic-chloro-hastingsite in the nakhlites MIL 03346 and pairs and NWA 5790: Insights from terrestrial chloro-amphibole. Meteoritics & Planetary Science, 51, 2127–2153.

Gillet, P., Barrat, J.A., Deloule, E., Wadhwa, M., Jambon, A., Sautter, V., Devouard, B., Neuville, D., Benzerara, K., and Lesourd, M. 2002. Aqueous alteration in the Northwest Africa 817 (NWA 817) Martian meteorite. Earth and Planetary Science Letters, 203, 431–444.

Goldoff, B., Webster, J.D., and Harlov, D.E. 2012. Characterization of fluor-chlorapatites by electron probe microanalysis with a focus on time-dependent intensity variation of halogens. American Mineralogist, 97, 1103–1115.

Gooding, J.L., Wentworth, S.J., and Zolensky, M.E. 1991. Aqueous alteration of the Nakhla meteorite. Meteoritics, 26, 135–143.

Hallis, L.J., Taylor, G.J., Nagashima, K., and Huss, G.R. 2012. Magmatic water in the martian meteorite Nakhla. Earth and Planetary Science Letters, 359, 84–92.

Harvey, R.P. and McSween Jr, H.Y. 1992. Petrogenesis of the nakhlite meteorites: Evidence from cumulate mineral zoning. Geochimica et Cosmochimica Acta, 56, 1655–1663.

Hess, P.C., Horzempa, P., Rutherford, M.J., and Devine, J. 1990. Phosphate equilibria in lunar basalts. 21st Lunar and Planetary Science Conference. Lunar and Planetary Institute, Woodlands, Texas. Houston.

Hewins, R.H., Humayun, M., Barrat, J.A., Zanda, B., Lorand, J.P., Pont, S., Assayag, N., Cartigny, P., Yang, S., and Sautter, V. 2020. Northwest Africa 8694, a ferroan chassignite: Bridging the gap between nakhlites and chassignites. Geochimica et Cosmochimica Acta, 282, 201–226.

Hicks, L.J., Bridges, J.C., and Gurman, S. J. 2014. Ferric saponite and serpentine in the nakhlite martian meteorites. Geochimica et Cosmochimica Acta, 136, 194–210.

Holland, H.D. 1972. Granites, solutions, and base metal deposits. Economic Geology, 67, 281–301.

Hounslow A.W. and Chao G.Y. 1968. Monoclinic chlorapatite from Ontario. The Canadian Mineralogist, 10, 252–259

Hovis, G.L. and Harlov, D.E. 2010. Solution calorimetric investigation of fluor-chlorapatite crystalline solutions. American Mineralogist, 95, 946-952.

Howarth, G.H., Pernet-Fisher, J.F., Bodnar, R.J., and Taylor, L.A. 2015. Evidence for the exsolution of Cl-rich fluids in martian magmas: Apatite petrogenesis in the enriched lherzolitic shergottite Northwest Africa 7755. Geochimica et Cosmochimica Acta, 166, 234–248.

Hughes, J.M. and Rakovan, J. 2002. The crystal structure of apatite, $Ca_5(PO_4)_3(F,OH,Cl)$. Reviews in Mineralogy and Geochemistry, 48, 1–12.

Hughes, J.M., Cameron, M., and Crowley, K.D. 1989. Structural variations in natural F, OH, and Cl apatites. American Mineralogist, 74, 870–876.

Hughes, J.M., Cameron, M., and Mariano, A.N. 1991. Rare-earth-element ordering and structural variations in natural rare-earth-bearing apatites. American Mineralogist, 76, 1165–1173.

Hughes, J.M., Nekvasil, H., Ustunisik, G., Lindsley, D.H., Coraor, A.E., Vaughn, J., Phillips, B., McCubbin, F.M., and Woerner, W.R. 2014. Solid solution in the fluorapatite–chlorapatite binary system: High-precision crystal structure refinements of synthetic F-Cl apatite. American Mineralogist, 99, 369–376.

Jagoutz, E. 1991. Chronology of SNC meteorites. Space Science Reviews, 56, 13–22.

Jolliff, B.L., Haskin, L. A., Colson, R. O., and Wadhwa, M. 1993. Partitioning in REE-saturating minerals: Theory, experiment, and modelling of whitlockite, apatite, and evolution of lunar residual magmas. Geochimica et Cosmochimica Acta, 57, 4069–4094.

Jones, J.H. 1989. Isotopic relationships among the shergottites, the nakhlites and Chassigny. Proceedings of the 19th Lunar and Planetary Science Conference. Lunar and Planetary Institute, Woodlands, Texas.

Kelly, S.R., Rakovan, J., and Hughes, J.M. 2017. Column anion arrangements in chemically zoned ternary chlorapatite and fluorapatite from Kurokura, Japan. American Mineralogist, 102, 720–727.

Kilinc, I.A. and Burnham, C.W. 1972. Partitioning of chloride between a silicate melt and coexisting aqueous phase from 2 to 8 kilobars. Economic Geology, 67, 231–235.

Korochantseva, E.V., Schwenzer, S.P., Buikin, A.I., Hopp, J., Ott, U., and Trieloff, M. 2011. ^{40}Ar-^{39}Ar and cosmic-ray exposure ages of nakhlites—Nakhla, Lafayette, Governador Valadares—and Chassigny. Meteoritics & Planetary Science, 46, 1397–1417.

Lee, M.R. and Chatzitheodoridis, E. 2016. Replacement of glass in the Nakhla meteorite by berthierine: Implications for understanding the origins of aluminum-rich phyllosilicates on Mars. Meteoritics & Planetary Science, 51, 1643–1653.

Lee, M.R., MacLaren, I., Andersson, S.M.L., Kovacs, A., Tomkinson, T., Mark, D.F., and Smith, C.L. 2015. Opal-A in the Nakhla meteorite: A tracer of ephemeral liquid water in the Amazonian crust of Mars. Meteoritics & Planetary Science, 50, 1362–1377.

Lentz, R.F., Taylor, G.J., and Treiman, A.H. 1999. Formation of a martian pyroxenite: a comparative study of the nakhlite meteorites and Theo's Flow. Meteoritics & Planetary Science, 34, 919–932.

Li, W. and Costa, F. 2020. A thermodynamic model for F-Cl-OH partitioning between silicate melts and apatite including non-ideal mixing with application to constraining melt volatile budgets. Geochimica et Cosmochimica Acta, 269, 203–222.

Lin, Y., Hu, S., Miao, B., Xu, L., Liu, Y., Xie, L., Feng, L., and Yang, J. 2013. Grove Mountains 020090 enriched lherzolitic shergottite: A two-stage formation model. Meteoritics & Planetary Science, 48, 1572–1589.

Longhi, J. 1991. Complex magmatic processes on Mars-Inferences from the SNC meteorites. Proceedings of the 21st Lunar and Planetary Science Conference. Lunar and Planetary Institute, Woodlands, Texas.

Malavergne, V., Guyot, F., Benzerara, K., and Martinez, I. 2001. Description of new shock-induced phases in the Shergotty, Zagami, Nakhla and Chassigny meteorites. Meteoritics & Planetary Science, 36, 1297–1305.

Marti, K. and Mathew, K.J. 2004. Martian mantle signatures in Yamato nakhlites. Antarctic meteorite research, 17, 117–131.

Martínez, M. 2021. Microstructural and Microchemical Studies of Fluid–Chondrule Interactions in a Pristine CR Carbonaceous Chondrite and Apatite in Martian Nakhlites. Ph.D. thesis. The University of New Mexico, USA. https://digitalrepository.unm.edu/eps_etds/304

Martínez, M., Brearley, A.J., and Shearer, C.K. 2020. Reading the microstructure of apatite in the moon and mars to constrain the petrogenetic evolution of chassignites and nakhlites and assess their volatile sources. 51st Lunar and Planetary Science Conference, Abstract 1878.

Mathez, E.A. and Webster, J.D. 2005. Partitioning behavior of chlorine and fluorine in the system apatite-silicate melt-fluid. Geochimica et Cosmochimica Acta, 69, 1275–1286.

McConnell, D. 1973. Apatite: Its Crystal Chemistry, Mineralogy and Geologic and Biologic Occurrences. Applied Mineralogy 5, first ed. Springer-Verlag, New York.

McCubbin, F.M. and Nekvasil, H. 2008. Maskelynite-hosted apatite in the Chassigny meteorite: Insights into late-stage magmatic volatile evolution in martian magmas. American Mineralogist, 93, 676–684.

McCubbin, F.M. and Jones, R.H. 2015. Extraterrestrial apatite: Planetary geochemistry to astrobiology. Elements, 11, 183–188.

McCubbin, F.M. and Ustunisik, G. 2018. Experimental investigation of F and Cl partitioning between apatite and Fe-rich basaltic melt at 0 GPa and 950–1050 C: Evidence for steric controls on apatite-melt exchange equilibria in OH-poor apatite. American Mineralogist: Journal of Earth and Planetary Materials, 103, 1455–1467.

McCubbin, F.M., Mason, H.E., Park, H., Phillips, B.L., Parise, J.B., Nekvasil, H., and Lindsley, D.H. 2008. Synthesis and characterization of low-OH- fluor-chlorapatite: A single crystal XRD and NMR spectroscopic study. American Mineralogist 93, 210–216.

McCubbin, F.M., Smirnov, A., Nekvasil, H., Wang, J., Hauri, E., and Lindsley, D.H. 2010. Hydrous magmatism on Mars: A source of water for the surface and subsurface during the Amazonian. Earth and Planetary Science Letters 292, 132–138.

McCubbin, F.M., Elardo, S.M., Shearer Jr, C.K., Smirnov, A., Hauri, E.H., and Draper, D.S. 2013. A petrogenetic model for the comagmatic origin of chassignites and nakhlites:

Inferences from chlorine-rich minerals, petrology, and geochemistry. Meteoritics & Planetary Science, 48, 819–853.

McCubbin, F.M., Vander Kaaden, K.E., Tartèse, R., Boyce, J.W., Mikhail, S., Whitson, E.S., Bell, A.S., Anand, M., Franchi, I.A., Jianhua, W., and Hauri, E.H. 2015. Experimental investigation of F, Cl, and OH partitioning between apatite and Fe-rich basaltic melt at 1.0–1.2 GPa and 950–1000 C. American Mineralogist, 100, 1790–1802.

Meurer, W.P. and Boudreau, A.E. 1996. An evaluation of models of apatite compositional variability using apatite from the Middle Banded series of the Stillwater Complex, Montana. Contributions to Mineralogy and Petrology, 125, 225–236.

Mikouchi, T. and Miyamoto, M. 2002. Comparative cooling rates of nakhlites as inferred from iron-magnesium and calcium zoning of olivines. 33rd Lunar and Planetary Science Conference, Abstract 1343.

Mikouchi, T., Miyamoto, M., Koizumi, E., Makishima, J., and McKay, G. 2006. Relative burial depths of nakhlites: an update. 37th Lunar and Planetary Science Conference, Abstract 1865.

Muttik, N., McCubbin, F. M., Keller, L.P., Santos, A.R., McCutcheon, W.A., Provencio, P.P., Rahman, Z., Shearer, C.K., Boyce, J. W., and Agee, C.B. 2014. Inventory of H_2O in the ancient Martian regolith from Northwest Africa 7034: The important role of Fe oxides. Geophysical Research Letters, 41, 8235–8244.

Newsom, H. E. 1980. Hydrothermal alteration of impact melt sheets with implications for Mars. Icarus, 44, 207–216.

Nyquist, L.E., Bogard, D.D., Shih, C.Y., Greshake, A., Stöffler, D., and Eugster, O. 2001. Ages and geologic histories of Martian meteorites. In Chronology and evolution of Mars (eds. R. Kallenbach, J. Geiss, and W.K. Hartmann). Space Sciences Series of ISSI, vol 12. Springer, Dordrecht. Pp. 105–164.

Pan, Y.M. and Fleet, M.E. 2002. Compositions of the apatite-group minerals: Substitution mechanisms and controlling factors, Phosphates: Geochemical, Geobiological, and Materials Importance, pp. 13–49.

Park, J., Garrison, D.H., and Bogard, D.D. 2009. ^{39}Ar–^{40}Ar ages of martian nakhlites. Geochimica et Cosmochimica Acta, 73, 2177–2189.

Peslier, A.H., Hervig, R., Yang, S., Humayun, M., Barnes, J.J., Irving, A.J., and Brandon, A.D. 2019. Determination of the water content and D/H ratio of the martian mantle by unraveling degassing and crystallization effects in nakhlites. Geochimica et Cosmochimica Acta, 266, 382–415.

Piccoli, P.M. and Candela, P.A. 2002. Apatite in igneous systems. Reviews in Mineralogy and Geochemistry, 48, 255–292.

Pittarello, L., Ferrière, L., Feignon, J.G., Osinski, G.R., and Koeberl, C. 2020. Preferred orientation distribution of shock-induced planar microstructures in quartz and feldspar. Meteoritics & Planetary Science, 55, 1082–1092.

Potts, N.J. 2017. Using Lunar Apatite to Assess the Volatile Inventory of the Lunar Interior. PhD thesis. The Open University.

Sautter, V., Jambon, A., and Boudouma, O. 2006. Cl-amphibole in the nakhlite MIL 03346: Evidence for sediment contamination in a Martian meteorite. Earth and Planetary Science Letters, 252, 45–55.

Schettler, G., Gottschalk, M., and Harlov, D.E. 2011. A new semi-micro wet chemical method for apatite analysis and its application to the crystal chemistry of fluorapatite-chlorapatite solid solutions. American Mineralogist, 96, 138-152.

Sharp, Z.D., Williams, J., Shearer, C.K., Agee, C.B., and McKeegan, K. 2016. The chlorine isotope composition of Martian meteorites 2. Implications for the early solar system and the formation of Mars. Meteoritics & Planetary Science, 51, 2111–2126.

Shearer, C.K., Burger, P.V., Papike, J.J., Sharp, Z.D., and McKeegan, K.D. 2011. Fluids on differentiated asteroids: Evidence from phosphates in differentiated meteorites GRA 06128 and GRA 06129. Meteoritics & Planetary Science, 46, 1345–1362.

Shearer, C.K., Messenger, S., Sharp, Z.D., Burger, P.V., Nguyen, A.N., and McCubbin, F.M. 2018. Distinct chlorine isotopic reservoirs on Mars. Implications for character, extent, and relative timing of crustal interactions with mantle-derived magmas, evolution of the martian atmosphere, and the building blocks of an early Mars. Geochimica et Cosmochimica Acta, 234, 24–36.

Słaby, E., Förster, H. J., Wirth, R., Giera, A., Birski, Ł., and Moszumańska, I. 2017. Validity of the apatite/merrillite relationship in evaluating the water content in the Martian mantle: Implications from shergottite Northwest Africa (NWA) 2975. Geosciences, 7, 99.

Stock, M.J., Humphreys, M.C., Smith, V.C., Johnson, R.D., Pyle, D.M., and EIMF. 2015. New constraints on electron-beam induced halogen migration in apatite. American Mineralogist, 100, 281-293.

Stormer, J.C. and Carmichael, I.S.E. 1971. Fluorine-hydroxyl exchange in apatite and biotite: A potential igneous geothermometer. Contributions to Mineralogy and Petrology, 31, 121–131.

964 Stormer, J.C., Pierson, M.L., and Tacker, R.C. 1993. Variation of F and Cl X-ray intensity due to
965 anisotropic diffusion in apatite during electron microprobe analysis. American
966 Mineralogist, 78, 641–648.

967 Sudarsanan, K.T. and Young, R.A. 1969. Significant precision in crystal structural details. Holly
968 Springs hydroxyapatite. Acta Crystallographica Section B: Structural Crystallography
969 and Crystal Chemistry, 25, 1534–1543.

970 Tartèse, R., Anand, M., McCubbin, F.M., Elardo, S.M., Shearer, C.K., and Franchi, I.A. 2014.
971 Apatites in lunar KREEP basalts: The missing link to understanding the H isotope
972 systematics of the Moon. Geology, 42, 363–366.

973 Treiman, A.H. 2005. The nakhlite meteorites: Augite-rich igneous rocks from Mars.
974 Geochemistry, 65, 203–270.

975 Treiman, A.H. and Irving, A.J. 2008. Petrology of martian meteorite Northwest Africa 998.
976 Meteoritics & Planetary Science, 43, 829–854.

977 Treiman, A.H., Dyar, M.D., McCanta, M., Noble, S.K., and Pieters, C.M. 2007. Martian Dunite
978 NWA 2737: Petrographic constraints on geological history, shock events, and olivine
979 color. Journal of Geophysical Research: Planets, 112, E4.

980 Ustunisik, G., Nekvasil, H., and Lindsley, D. 2011. Differential degassing of H_2O, Cl, F, and S:
981 Potential effects on lunar apatite. American Mineralogist, 96, 1650–1653.

982 Udry, A. and Day, J.M. 2018. 1.34 billion-year-old magmatism on Mars evaluated from the co-
983 genetic nakhlite and chassignite meteorites. Geochimica et Cosmochimica Acta, 238,
984 292–315.

985 Usui, T., Alexander, C.M.D., Wang, J., Simon, J.I., and Jones, J.H. 2012. Origin of water and
986 mantle–crust interactions on Mars inferred from hydrogen isotopes and volatile element
987 abundances of olivine-hosted melt inclusions of primitive shergottites. Earth and
988 Planetary Science Letters, 357, 119–129.

989 Vaughn, J.S., Woerner, W.R., Lindsley, D.H., Nekvasil, H., Hughes, J.M., and Phillips, B.L.
990 2015. Hydrogen environments in low-OH, F, Cl apatites revealed by double resonance
991 solid-state NMR. The Journal of Physical Chemistry C, 119, 28605–28613.

992 Wadhwa, M. and Crozaz, G. 1995. Trace and minor elements in minerals of nakhlites and
993 Chassigny: Clues to their petrogenesis. Geochimica et Cosmochimica Acta, 59, 3629–
994 3645.

995 Webster, J.D. and Piccoli, P.M. 2015. Magmatic apatite: A powerful, yet deceptive,
996 mineral. Elements, 11, 177–182.

White, T., Ferraris, C., Kim, J., and Madhavi, S. 2005. Apatite–an adaptive framework structure. Reviews in Mineralogy and Geochemistry, 57, 307–401.

Williams, J.T., Shearer, C.K., Sharp, Z.D., Burger, P.V., McCubbin, F.M., Santos, A.R., Agee, C.B., and McKeegan, K.D. 2016. The chlorine isotopic composition of Martian meteorites 1: Chlorine isotope composition of Martian mantle and crustal reservoirs and their interactions. Meteoritics & Planetary Science, 51, 2092–2110.

Zirner, A.L., Marks, M.A., Wenzel, T., Jacob, D.E., and Markl, G. 2015. Rare earth elements in apatite as a monitor of magmatic and metasomatic processes: The Ilímaussaq complex, South Greenland. Lithos, 228, 12–22.

1007 **FIGURE CAPTIONS**

1008 Figure 1. BSE mosaics of the two thin sections of the martian basalts used in this study. (a)
1009 NWA 998 thin section showing cumulus pyroxenes (in medium grey), titanomagnetite (in lighter
1010 grey), and troilite (in white). Intercumulus regions are shown in darker grey, which are randomly
1011 distributed and range from ~100 μm to ~500 μm, and some contain intercumulus apatite. Apatite
1012 grains (up to ~200 μm in size) are commonly found embedded in cumulus pigeonite or augite. b)
1013 Nakhla thin section showing cumulus pyroxenes, which comprise most of the area,
1014 titanomagnetite, which varies greatly in size (in light grey), and intercumulus regions (in dark
1015 grey), ranging from ~50 to ~370 μm in size. Apatites in Nakhla are exclusively found inside
1016 intercumulus melt pockets. White squares indicate the locations of the apatite grains that were
1017 selected for this study, which represent a large subpopulation of all apatites in the samples. Some
1018 of the individual apatite grains are shown and described in Figures 2 and 3.
1019

1020 Figure 2. Backscattered electron SEM images of selected apatite (Ap) grains in NWA 998.
1021 Apatite numbers refer to grains identified in Fig. 1. a) Ap2: Anhedral intercumulus chlorapatite,
1022 ~50 μm size, associated with K-rich glass, zoned pyroxene, and a fracture. b) Ap3: Anhedral
1023 intercumulus chlorapatite, ~100 μm in size, associated with titanomagnetite, K-rich glass, and
1024 zoned pyroxene. c) Ap5: Euhedral cumulus chlorapatites with sizes ranging from ~10 to 50 μm,
1025 partially intergrown or totally included in titanomagnetite. FIB section 2 (FIB2) was extracted in
1026 the euhedral apatite 5.2. The observed linear features are artifacts caused by thin section
1027 polishing. d) Ap7: Anhedral to euhedral cumulus apatite grains included in pigeonite and augite.
1028 FIB section 1 (FIB1) was extracted in Ap7.3, a subhedral, ~75 μm long grain, fully included in
1029 augite. e) Ap10: Large (up to 200 μm in size) anhedral, intercumulus apatites partially included

in alkali feldspar and augite. f) A12: Anhedral intercumulus chlorapatite grains, ~25–35 μm size, included in alkali feldspar and intergrown with titanomagnetite. Legend: Ap = apatite, Afs = alkali feldspar, Alk-glass = alkali-rich glass, K-glass = K-rich glass, Pgn = pigeonite, Aug = augite, Tmt = titanomagnetite, Tro = troilite, Ilm = ilmenite.

Figure 3. Backscattered electron SEM images of apatite (Ap) grains in Nakhla. a) Ap1: Acicular intercumulus apatites, ~5 μm in size, randomly oriented, embedded in alkali feldspar and K-rich glass, and associated with titanomagnetite. Apatites cut close to parallel or perpendicular to the *c* direction show zonation. b) Intercumulus μm-sized apatites cut perpendicular and subparallel to the *c* axis, partially included in a melt pocket and the pyroxene. Ap2.2 are compositionally zoned. c) Parallel to subparallel acicular chlorapatites included in K-rich glass and alkali feldspar, associated with troilite. FIB3 was cut perpendicular to the elongation direction. d) Apa3: Euhedral, zoned intercumulus apatite, ~15 μm-size, in the interstice between a K-rich maskelynite melt pocket and augite. Legend: Ap = apatite, Afs = alkali feldspar, Or = orthoclase, K-glass = K-rich glass, Pyx = pyroxene, Aug = augite, Tmt = titanomagnetite, Tro = troilite.

Figure 4. Ternary plot of apatite X-site occupancy (mol%) for NWA 998 and Nakhla. Unless otherwise indicated, individual symbols represent single analyses. Aquamarine and yellow crosses represent multiple analyses of NWA 998 apatites from Treiman and Irving (2008) and McCubbin et al. (2013), respectively, obtained by EPMA (the shadowed green area comprise the full range of apatite values obtained by McCubbin et al., 2013). The shadowed pink and green areas comprise the full range of compositions for Nakhla and NWA 998 apatites, respectively,

1052 obtained by EPMA, from McCubbin et al. (2013) study. All analyses from this work were
1053 obtained by semiquantitative S/TEM-EDS analysis. Z = missing component (OH + vacancies).
1054

1055 Figure 5. Dark-field STEM mosaics of the three FIB sections extracted in NWA 998 and Nakhla
1056 apatites. a) FIB1 extracted in NWA 998 cumulus apatite showing that it consists of a single
1057 crystal with a set of parallel fractures and dislocations. The grain boundary between apatite and
1058 pigeonite is marked with a dashed line. The observed nanometer-scale, worm-like features
1059 throughout the FIB section are caused by re-deposition during FIB sample preparation.
1060 Numbered squares represent the location of EDS analyses (Table 1). Left-hand side inset shows
1061 a BF-TEM image of a fracture and a dislocation array, which are parallel and subparallel to each
1062 other. Right-hand side inset shows a [1-21] zone axis diffraction pattern of apatite showing
1063 diffuse streaking parallel to the [111] direction. b) FIB2 extracted in NWA 998 cumulus apatite
1064 oriented parallel to the [011] zone axis showing that it is mostly homogeneous in texture, except
1065 for a small region where apatite is polycrystalline (dashed rectangle). Cleavage planes show
1066 curvature and opening (fracturing). Inset of the [534] zone axis diffraction pattern shows
1067 streaking in the [313] direction. c) FIB3 extracted in an intercumulus region in Nakhla showing
1068 apatite grains numbered from 1 to 4. Apatites are embedded in an amorphous silica and K-rich
1069 glass. Other phases include silica (tridymite), K-,Na-rich feldspar, and clay minerals
1070 (phyllosilicates). Fractures and/or porosity occur throughout. Inset of a diffraction pattern
1071 showing that the grain is cut perpendicular to the *c* axis. Amor SiO_2 = amorphous SiO_2, Tri =
1072 tridymite, K-glass = K-rich feldspathic glass (maskelynite), clay min = clay minerals.
1073

Figure 6. Dark-field STEM images of martian apatites. a) Z-contrast image of NWA 998 FIB2 apatite showing 5-10 nm-size domains with different Z-contrasts indicative of compositional differences between them. b) Dark-field image of a region in Nakhla (FIB3) showing apatite grains with radial fractures filled with phyllosilicates and embedded in amorphous silica and K-rich glass. c) Dark-field STEM image of apatite 3 (FIB3, Nakhla) showing a texture that suggests apatite nucleated at a region on the left-hand side of the grain. d) Close-up image of the region in (c) showing the corresponding layers of growth (~50-100 μm in width). e) Region in Nakhla mesostasis melt pocket (FIB3) showing the occurrence of tridymite, K-, Na-rich feldspar, and phyllosilicates. f) Region in Nakhla mesostasis melt pocket (FIB3) showing the characteristic sheet texture of the phyllosilicates, typically found filling interstitial regions between grains (apatite, amorphous silica, and alkali-rich feldspar).

Figure 7. High-resolution TEM images of NWA 998 apatites. a) Single crystal apatite in FIB1, with 2.43 wt% Cl and 1.92 wt% F, showing mottled texture with different domains 5-10 nm in size, apparent by mismatches and differences in the contrast in the lattice fringes. b) Close-up HRTEM image with inset Fast Fourier Transform (FFT) indicating the direction of the streaking parallel to the [111] direction. Different domains are marked in dashed white lines, showing that some domains are very close to exactly down the zone axis, while others show a slight misorientation. The differences in contrast in the lattice fringes are indicative of slight differences in orientation of the different domains and strain in the lattice. c) Single crystal apatite in the right-hand side of FIB2, with 3 wt% Cl and 1.5 wt% F. The HRTEM image shows that (100) lattice fringes exhibit evidence of curvature (undulosity), indicative of strain in the lattice. d) and e) Two close-up images in FIB 2 showing that lattice fringes do not lose continuity

1097 at the boundaries between domains. f) Polycrystalline apatite (region marked with a dashed
1098 rectangle in Figure 5b), with 3.65 wt% Cl and 0.71 wt% F. Note the grain boundary (different
1099 orientations of the lattice fringes). SAED patterns of the crystal show it is oriented parallel to the
1100 [011] zone axis. Apatite in this area does not show curvature of the lattice fringes or significant
1101 diffraction contrast.
1102

1103 Figure 8. High-resolution TEM images of Nakhla apatites in FIB3 showing: a) and b) the
1104 hexagonal crystal structure viewed down the [001] zone axis, and slight curvature of the (010)
1105 lattice fringes in (a) but not in (b). The region in (c) shows changes in the contrast of the lattice
1106 fringes due to slight differences in orientation of the different domains and slight curvature of
1107 (010) planes (same direction as in (a) and (b)). d) High-resolution TEM image of planar features
1108 in apatite, showing brighter regions in the (110) and the (100) planes. Inset of Cl map (lower
1109 right) performed with EFTEM shows that very slight differences in Cl concentration are
1110 apparent. However, the heterogeneity does not appear to correspond to the brighter regions
1111 observed with HTEM.
1112

1113 Figure 9. Schematic representation (not to scale) of the chassignites NWA 2737, Chassigny, and
1114 NWA 8694 (data from Beck et al., 2006; McCubbin and Nekvasil, 2008; McCubbin et al., 2013;
1115 and Hewins et al., 2020), and the nakhlites NWA 998 (data from McCubbin et al., 2013 and this
1116 work) and Nakhla (data from McCubbin et al., 2013 and this work) with their different apatite
1117 occurrences and halogen evolution. Note that differences in orientation of the crystal relative to
1118 the incident beam in apatite grains might result in variations in the F and Cl contents (Stormer et
1119 al., 1993).

1120

1121 Figure 10. Ca/P versus Si (atomic %) from a) NWA 998 cumulus apatite (FIB2) and b) Nakhla

1122 intercumulus apatites (FIB3), obtained by TEM-EDS.

1123

1124

1125 # TABLES

1126 Table 1. TEM-EDS analyses (oxide wt%) on apatite 7.3 (Fig. 5a) and pigeonite in NWA 998 FIB1.
1127

Oxides wt%	Apatite				**Mean**		Pigeonite
P_2O_5	37.70	39.90	40.15	38.52	**39.60**	SiO_2	56.47
SiO_2	2.44	1.63	1.22	2.57	**1.99**	Al_2O_3	0.51
CaO	56.08	53.86	53.60	53.87	**55.09**	FeO	23.39
FeO	0.30	0.27	0.32	0.42	**0.33**	MnO	0.67
F	1.86	2.13	1.53	2.07	**1.92**	MgO	17.29
Cl	1.64	2.22	3.18	2.56	**2.43**	CaO	1.68
Total	100	100	100	100	**100**		100
Cl/F (wt%)	0.88	1.04	2.08	1.24	**1.26**		
Structural formulae based on 13 oxygens						*Based on 6 [O]*	
P	2.75	2.90	2.93	2.81	**2.85**	Si	2.1
Si	0.21	0.14	0.10	0.22	**0.17**	Al	0.02
Ca	5.18	4.96	4.95	4.99	**5.02**	Fe	0.73
Fe	0.02	0.02	0.02	0.03	**0.02**	Mg	0.96
F	0.51	0.58	0.42	0.57	**0.52**	Mn	0.02
Cl	0.24	0.32	0.46	0.37	**0.35**	Ca	0.07
Z	0.25	0.10	0.12	0.06	**0.13**		
Total cat	8.17	8.01	8.01	8.06	**8.06**		
Ca/P atomic	1.89	1.71	1.69	1.77	**1.76**		

1128 n.d. = not detected
1129 Z = missing component (OH + vacancies)
1130
1131 Table 2. TEM-EDS analyses (oxide wt%) of the host and the polycrystalline (Polycr) apatites in NWA
1132 998 FIB2 after cleaning the FIB section at 5 kV to remove redeposited material.
1133

Oxides wt%	Host apatite									**Mean**	Polycr
P_2O_5	40.42	40.84	40.01	39.46	39.28	38.93	39.76	40.1	39.44	**39.80**	40.06
SiO_2	0.79	1.75	1.33	1.39	2.25	2.76	2.5	2.16	2.93	**1.98**	2.82
Al_2O_3	1.34	1.28	1.3	1.47	0.53	0.42	0.4	0.19	0.23	**0.80**	0.13
SO_3	n.d.	n.d.	n.d.	n.d.	n.d.	n.d.	n.d.	n.d.	n.d.	**n.d.**	n.d.
CaO	52.81	51.83	52.19	52.9	52.64	52.82	52.39	52.43	52.3	**52.48**	52.46
FeO	0.46	0.4	0.42	0.42	0.33	0.31	0.3	0.32	0.27	**0.36**	0.18
F	1.26	1.74	1.45	1.42	1.4	1.56	1.49	1.47	1.57	**1.48**	0.71
Cl	2.91	2.17	3.28	2.93	3.59	3.22	3.18	3.33	3.27	**3.10**	3.65
Total	100	100	100	100	100	100	100	100	100	**100**	100
Cl/F (wt%)	2.31	1.25	2.26	2.06	2.56	2.06	2.13	2.27	2.08	**2.11**	5.14
Structural formulae based on 13 oxygens											
P	2.92	2.92	2.9	2.86	2.86	2.83	2.88	2.91	2.86	**2.88**	2.88
Si	0.07	0.15	0.11	0.12	0.19	0.24	0.21	0.18	0.25	**0.17**	0.24

Al	0.13	0.13	0.13	0.15	0.05	0.04	0.04	0.02	0.02	**0.08**	0.01
S	n.d.	n.d.	n.d.	n.d.	n.d.	n.d.	n.d.	n.d.	n.d.	**n.d.**	n.d.
Ca	4.83	4.69	4.79	4.86	4.86	4.87	4.8	4.81	4.8	**4.81**	4.78
Fe	0.03	0.03	0.03	0.03	0.02	0.02	0.02	0.02	0.02	**0.02**	0.01
F	0.34	0.46	0.39	0.38	0.38	0.42	0.4	0.4	0.42	**0.40**	0.19
Cl	0.42	0.31	0.48	0.42	0.52	0.47	0.46	0.48	0.47	**0.45**	0.53
Z	0.24	0.23	0.13	0.19	0.1	0.11	0.14	0.12	0.1	**0.15**	0.28
Total cat	7.99	7.91	7.97	8.02	7.99	8	7.95	7.95	7.95	**7.97**	7.93
Ca/P atomic	1.66	1.61	1.65	1.7	1.7	1.72	1.67	1.66	1.68	**1.67**	1.66

Z = calculated missing component (OH + vacancies)
n.d. = not detected

Table 3. S/TEM-EDS analyses (oxides wt%) of the four apatite grains in Nakhla (FIB3).

Oxides wt%	Ap1	Ap1	Ap2	Ap2	Ap2	Ap3C	Ap3C	Ap3R	Ap3R	Ap4	Ap4	Mean
P_2O_5	38.82	38.96	38.36	37.61	39.19	37.61	37.42	38.20	38.48	36.90	35.43	37.91
SiO_2	2.48	2.76	3.81	5.41	3.14	4.58	5.16	3.42	3.59	5.93	3.91	4.02
Al_2O_3	0.30	0.08	n.d.	0.13	0.36	0.42	0.43	0.30	0.36	0.94	0.32	0.33
Ce_2O_3	0.45	0.59	n.d.	n.d.	0.09	0.53	0.55	0.14	0.13	0.30	n.d.	0.25
Nd_2O_3	0.19	0.23	n.d.	n.d.	0.09	0.33	0.31	0.06	0.05	0.21	n.d.	0.13
MnO	0.06	n.d.	n.d.	n.d.	0.09	0.08	0.06	0.05	0.05	0.18	n.d.	0.05
CaO	52.46	52.41	52.90	51.88	51.70	51.22	50.50	51.97	51.49	51.61	55.48	52.15
FeO	0.32	0.37	0.08	0.15	0.24	0.41	0.44	0.21	0.14	0.56	0.27	0.29
SO3	n.d.	n.d.	n.d.	n.d.	n.d.	n.d.	n.d.	n.d.	n.d.	n.d.	0.15	0.01
F	1.22	1.34	1.00	0.87	0.84	0.62	0.63	0.52	0.20	1.90	1.33	0.95
Cl	3.66	3.21	3.86	3.96	4.24	4.18	4.47	5.12	5.50	2.93	3.11	4.02
Total	100	100	100	100	100	100	100	100	100	100	100	100
Cl/F	3.00	2.40	3.86	4.55	5.05	6.74	7.10	9.85	27.50	1.55	2.34	4.23
Structural formulae based on 13 [O]												
P	2.84	2.84	2.79	2.72	2.85	2.74	2.72	2.80	2.81	2.64	2.62	2.76
Si	0.21	0.24	0.33	0.46	0.27	0.39	0.44	0.30	0.31	0.50	0.34	0.35
Al	0.03	0.01	n.d.	0.01	0.04	0.04	0.04	0.03	0.04	0.09	0.03	0.03
Ce	0.01	0.02	n.d.	n.d.	n.d.	0.02	0.02	n.d.	n.d.	0.01	n.d.	0.01
Nd	0.01	0.01	n.d.	n.d.	n.d.	0.01	0.01	n.d.	n.d.	0.01	n.d.	n.d.
Mn	n.d.	n.d.	n.d.	n.d.	0.01	0.01	n.d.	n.d.	n.d.	0.01	n.d.	n.d.
Ca	4.86	4.84	4.87	4.75	4.76	4.73	4.66	4.83	4.77	4.68	5.19	4.81
Fe	0.02	0.03	0.01	0.01	0.02	0.03	0.03	0.01	0.01	0.04	0.02	0.02
S	n.d.	n.d.	n.d.	n.d.	n.d.	n.d.	n.d.	n.d.	n.d.	n.d.	0.02	n.d.
F	0.33	0.37	0.27	0.23	0.23	0.17	0.17	0.14	0.05	0.51	0.37	0.26
Cl	0.54	0.47	0.56	0.57	0.62	0.61	0.65	0.75	0.80	0.42	0.46	0.59
Z	0.13	0.17	0.17	0.19	0.16	0.22	0.18	0.11	0.14	0.07	0.17	0.16
Total cat	8.00	7.98	7.99	7.96	7.94	7.96	7.93	7.98	7.95	7.98	8.23	7.99

Ca/P atomic	1.71	1.71	1.75	1.75	1.67	1.73	1.71	1.72	1.70	1.77	1.98	1.74

Ap# = apatite number (in Fig. 5c)
C = core, R = rim
Z = calculated missing component (OH + vacancies)
n.d. = not detected

Figure 1

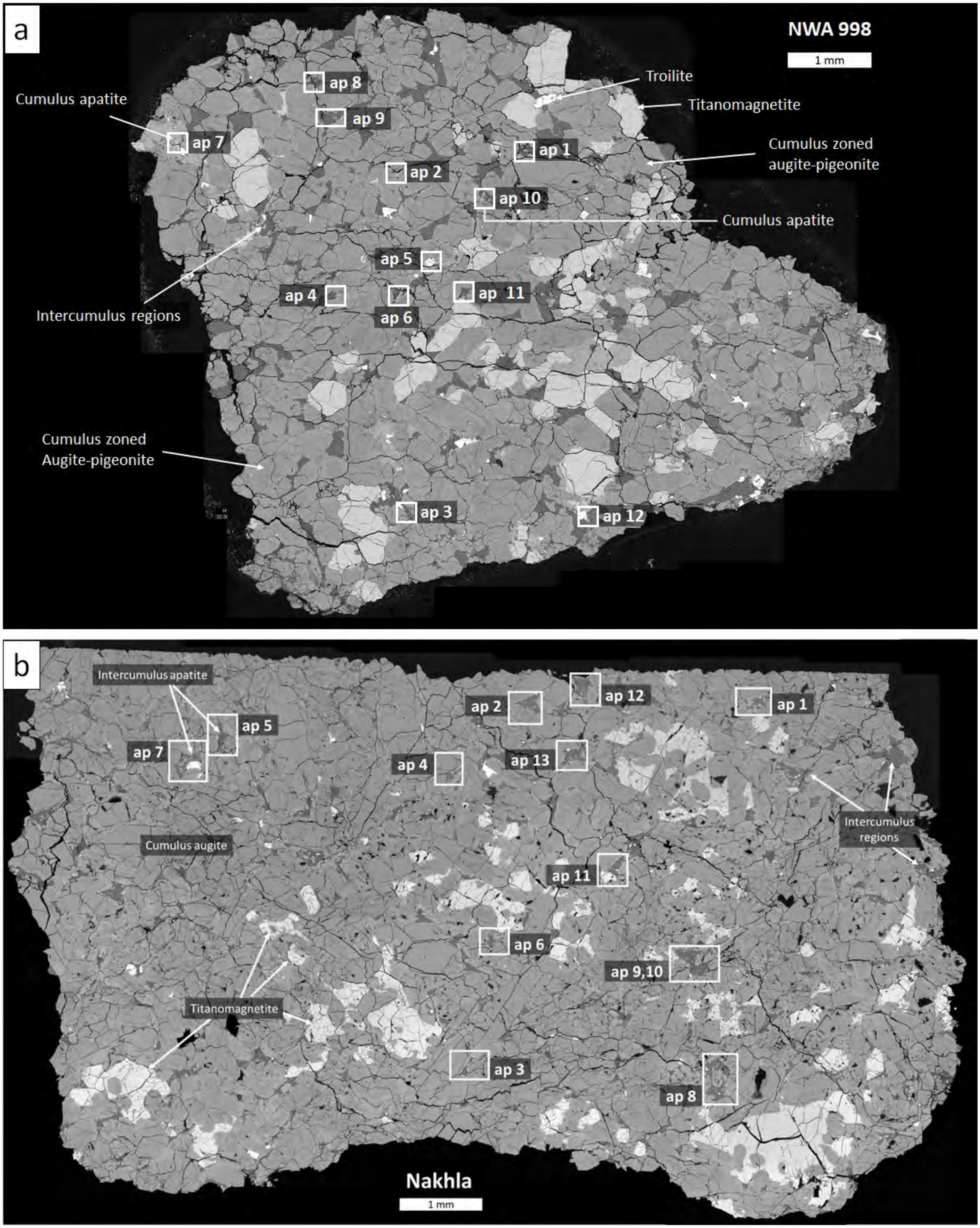
a
NWA 998
1 mm
Troilite
Titanomagnetite
Cumulus apatite
Cumulus zoned
augite-pigeonite
Cumulus apatite
Intercumulus regions
Cumulus zoned
Augite-pigeonite
ap 8
ap 9
ap 7
ap 1
ap 2
ap 10
ap 5
ap 4
ap 6
ap 11
ap 3
ap 12
b
Intercumulus apatite
ap 5
ap 7
ap 2
ap 12
ap 1
ap 4
ap 13
Intercumulus
regions
Cumulus augite
ap 11
ap 6
ap 9,10
Titanomagnetite
ap 3
ap 8
Nakhla
1 mm

Figure 2

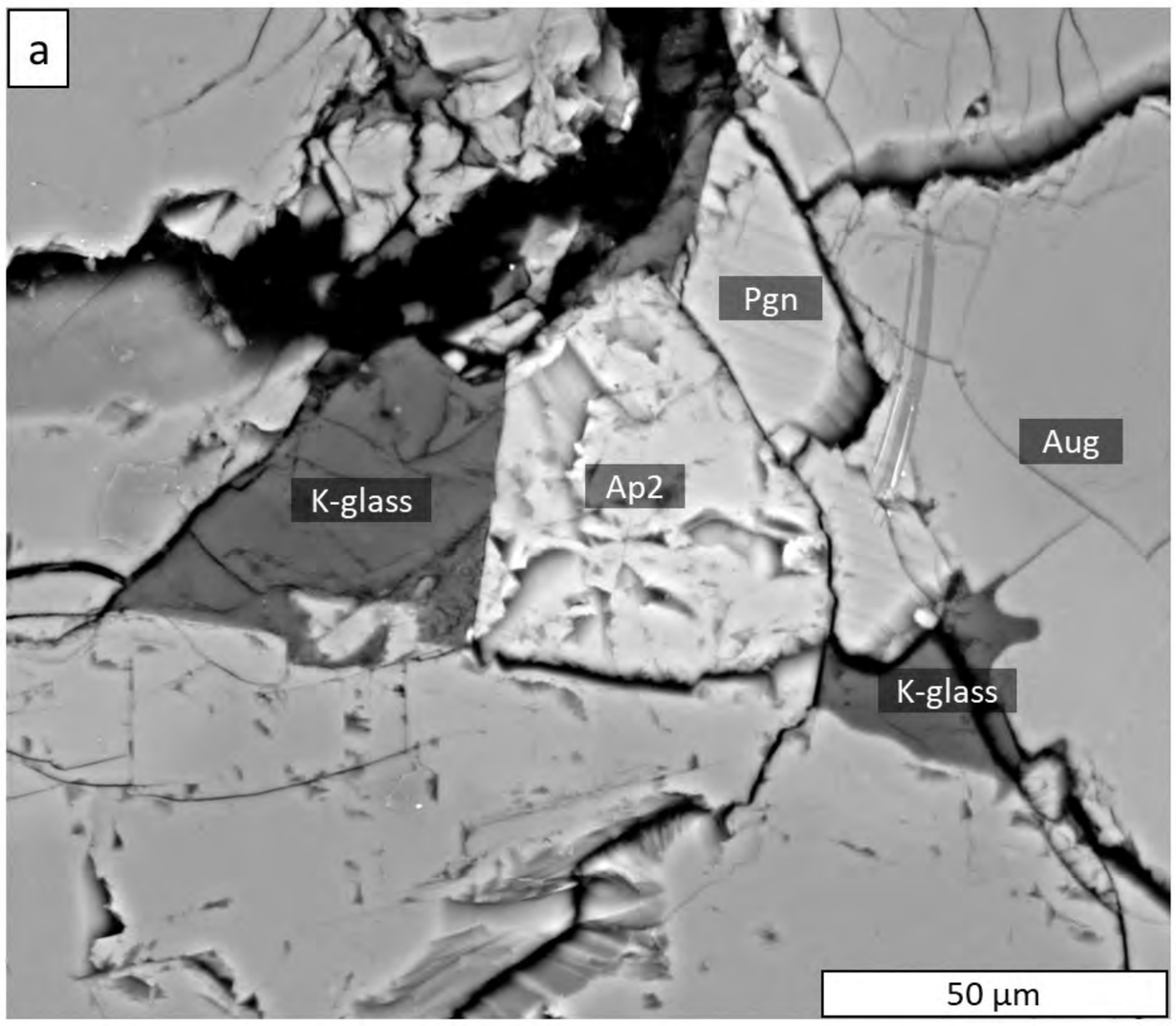
a
Pgn
Aug
K-glass
Ap2
K-glass
50 µm

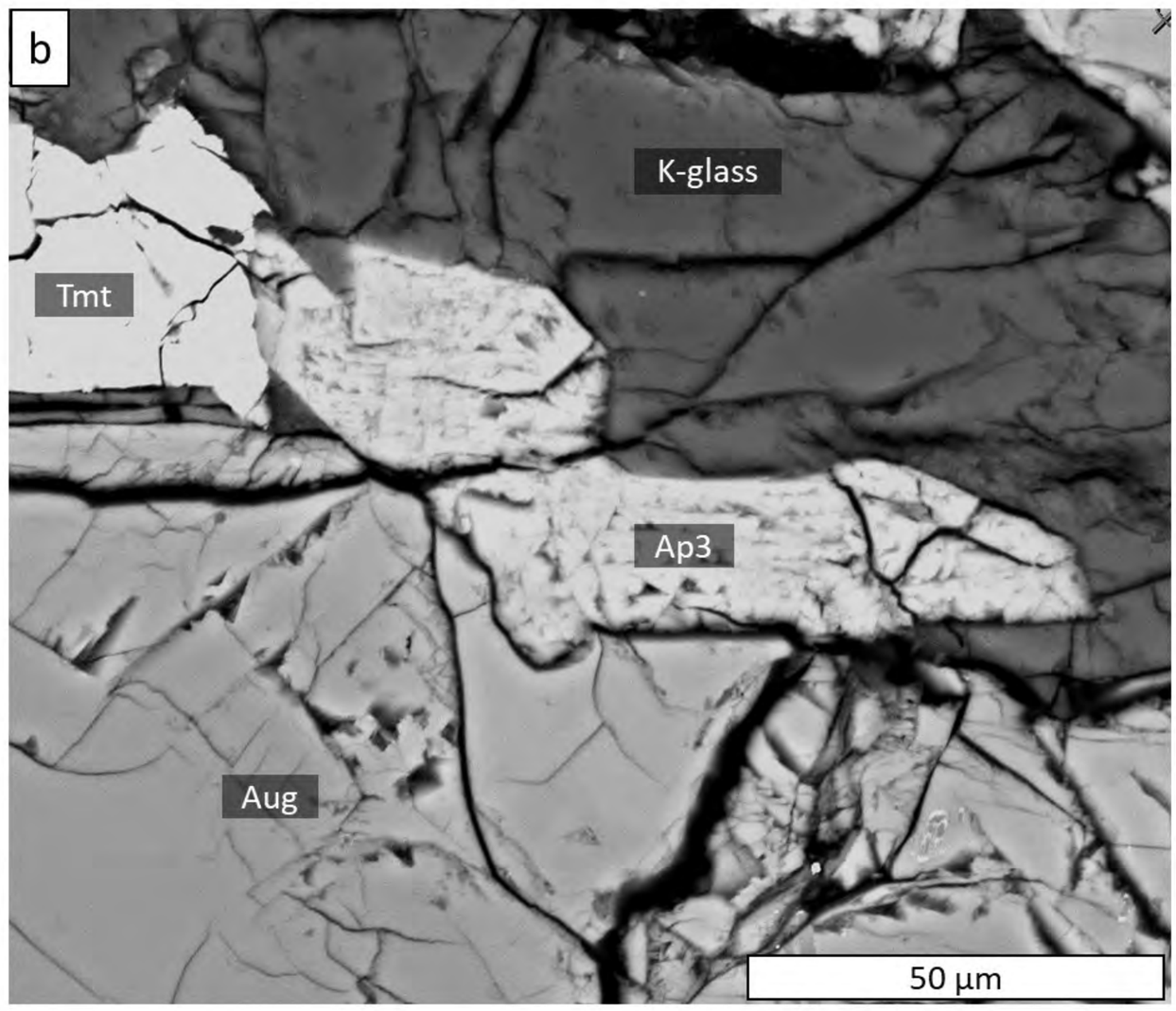
b
K-glass
Tmt
Ap3
Aug
50 µm

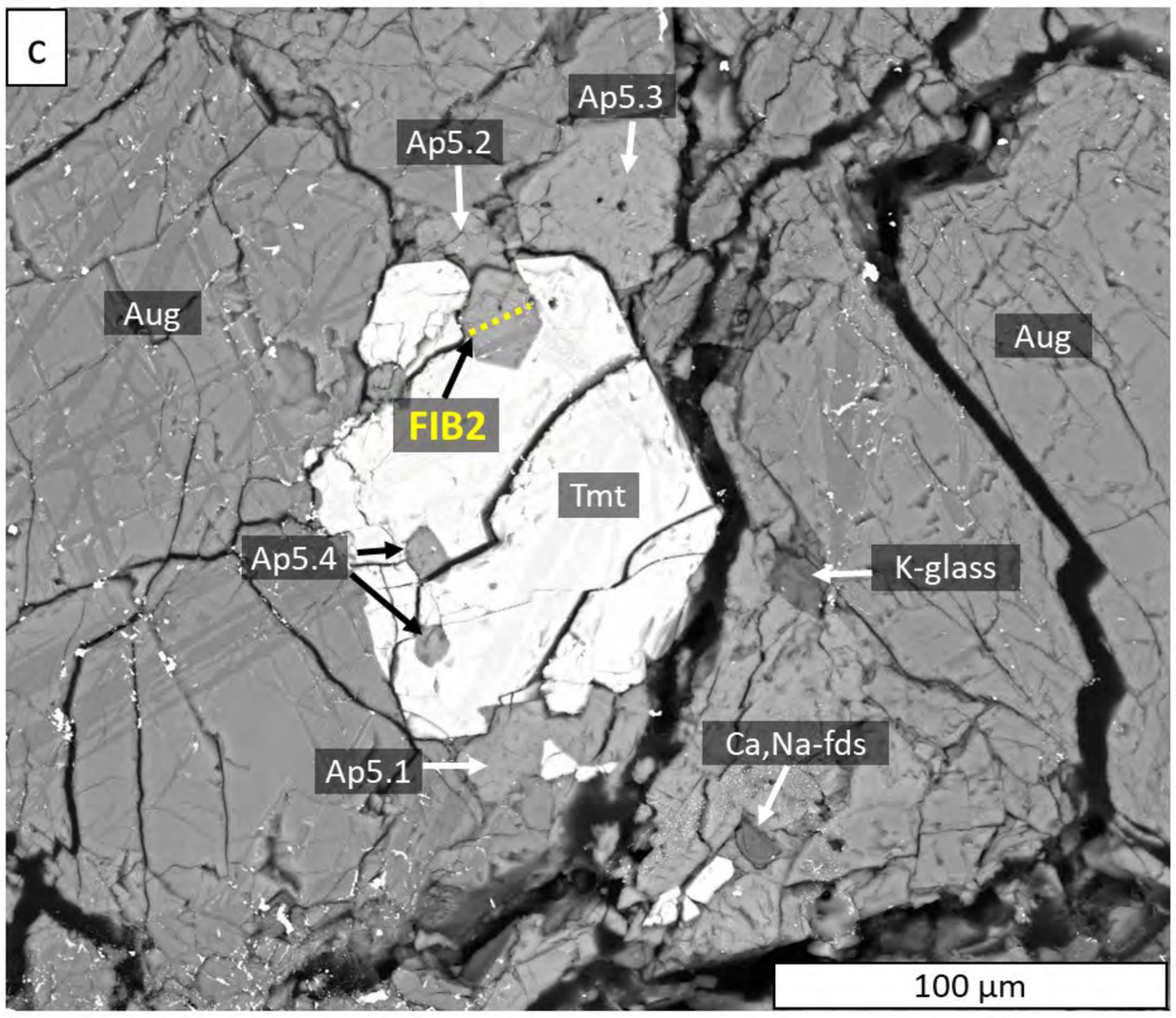
c
Ap5.3
Ap5.2
Aug
Aug
FIB2
Tmt
Ap5.4
K-glass
Ap5.1
Ca,Na-fds
100 µm

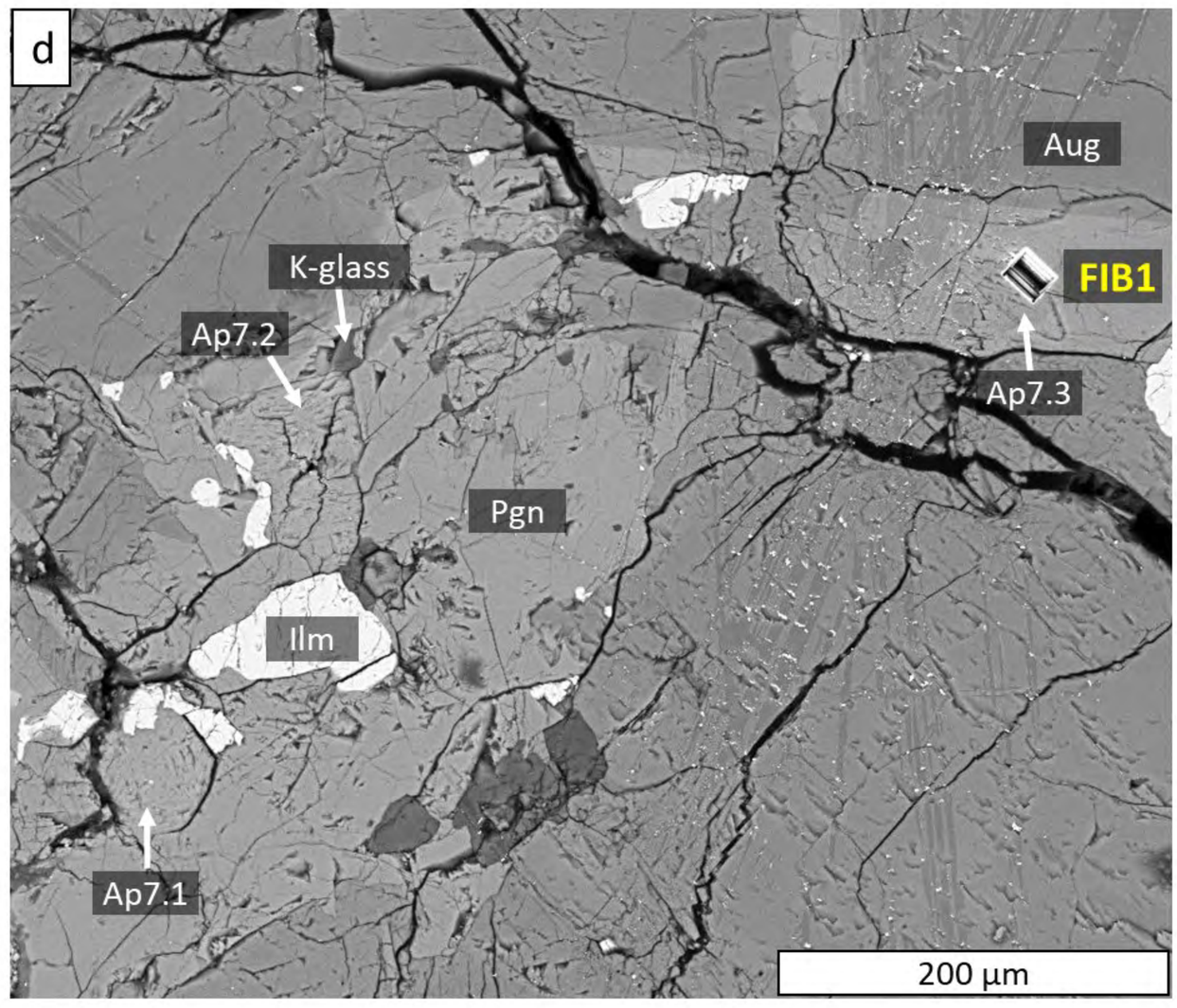
d
Aug
K-glass
FIB1
Ap7.2
Ap7.3
Pgn
Ilm
Ap7.1
200 µm

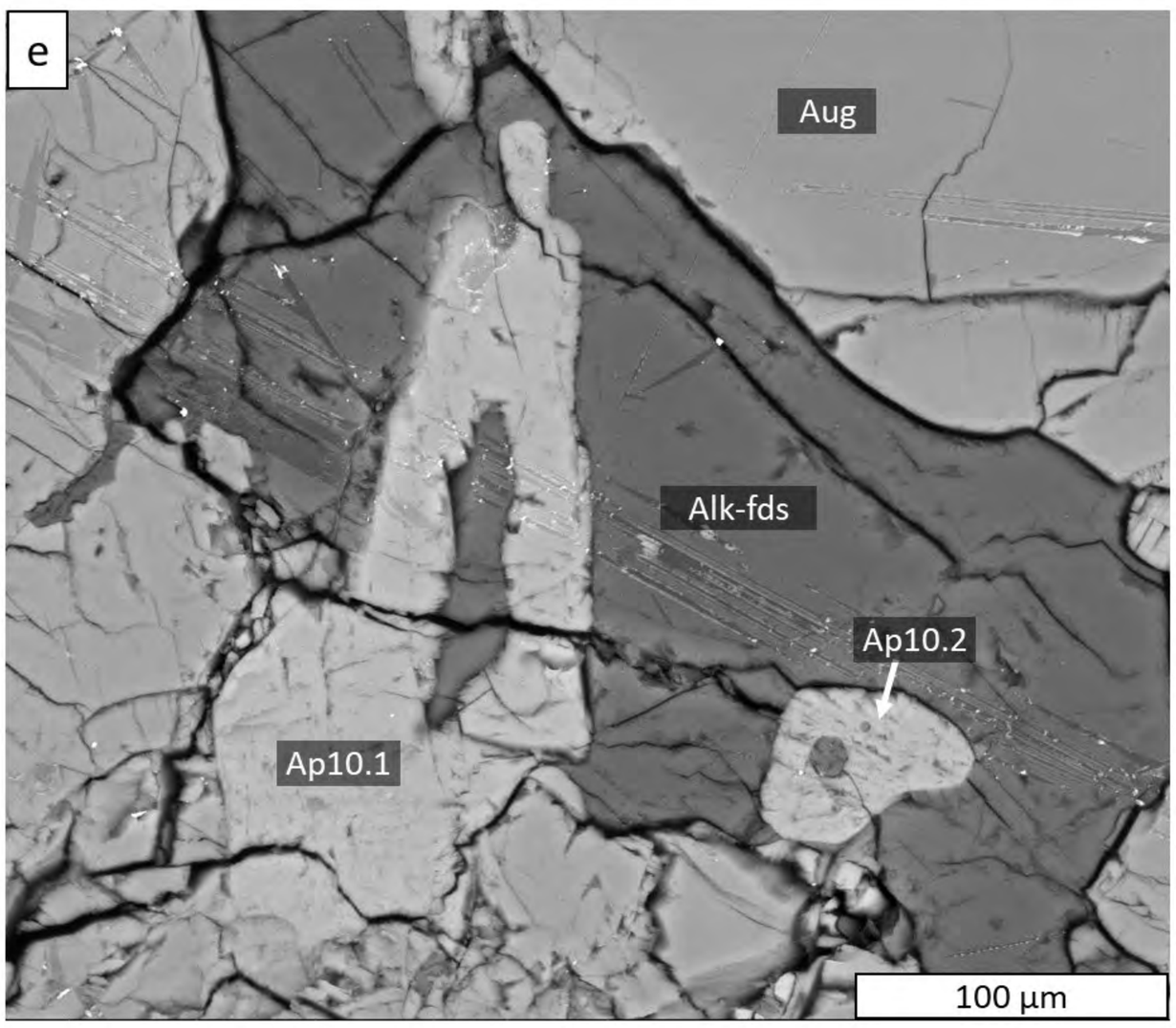
e
Aug
Alk-fds
Ap10.2
Ap10.1
100 µm

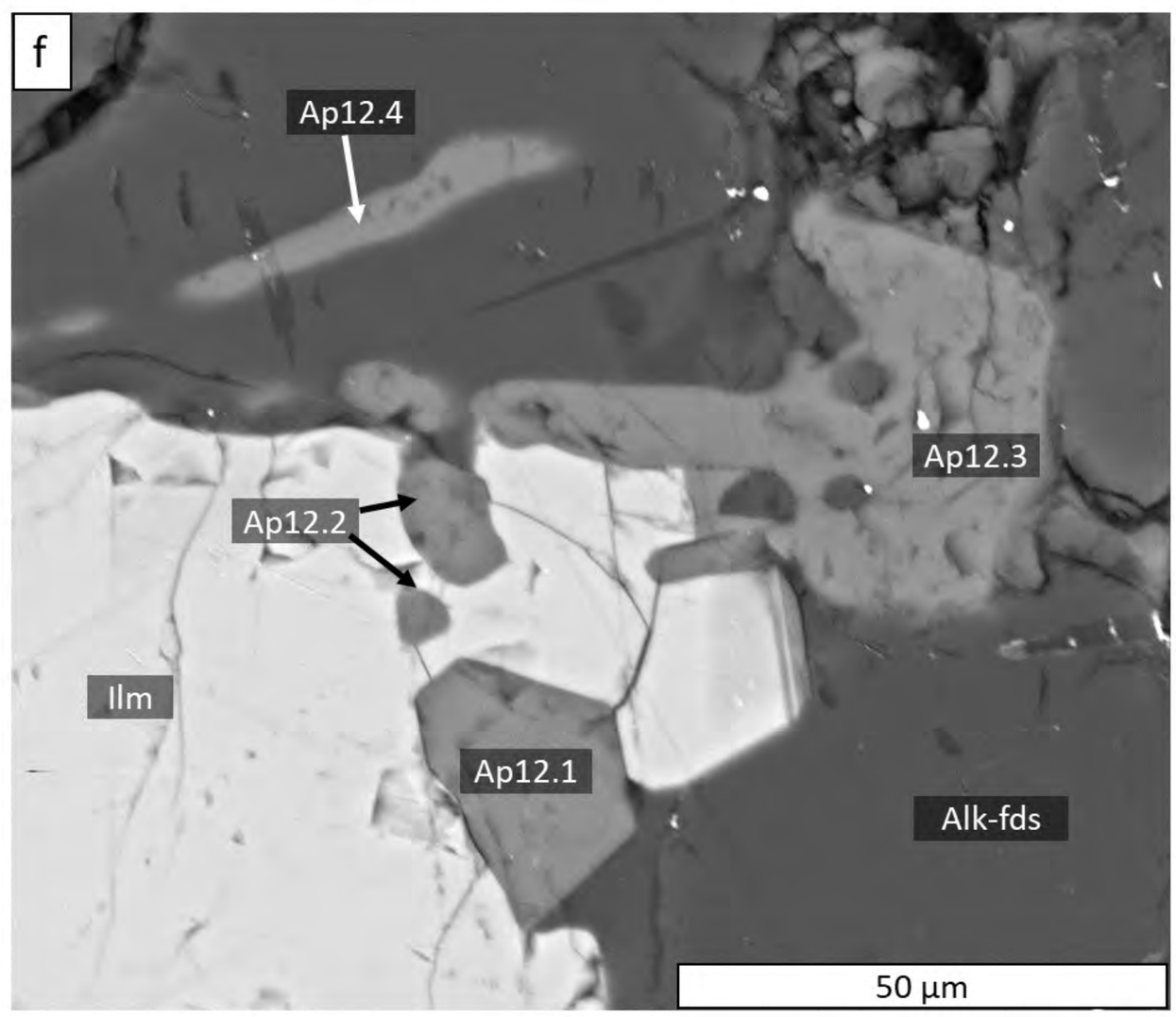
f
Ap12.4
Ap12.3
Ap12.2
Ilm
Ap12.1
Alk-fds
50 µm

Figure 3

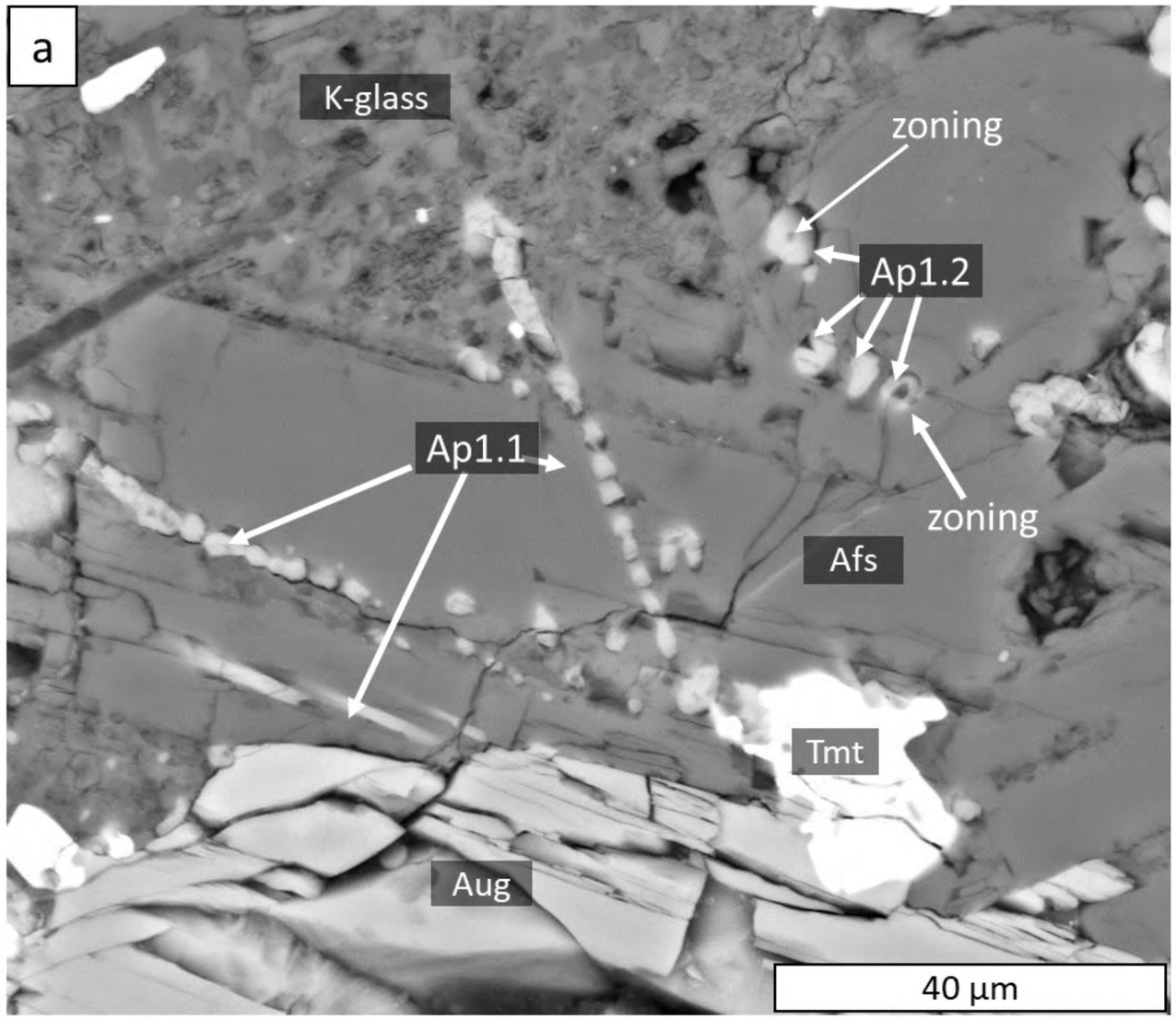
a
K-glass
zoning
Ap1.2
Ap1.1
zoning
Afs
Tmt
Aug
40 µm

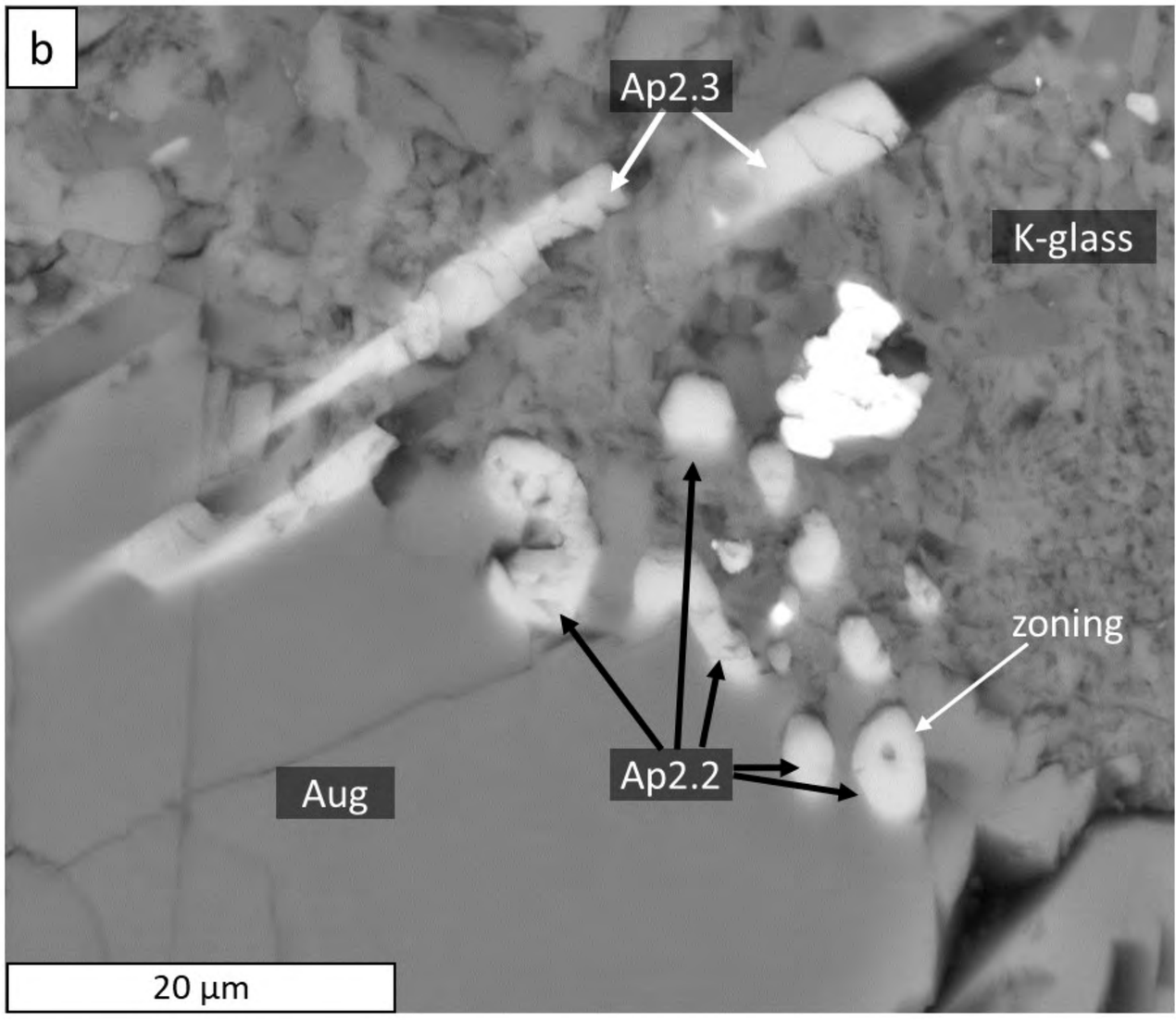
b
Ap2.3
K-glass
zoning
Aug
Ap2.2
20 µm

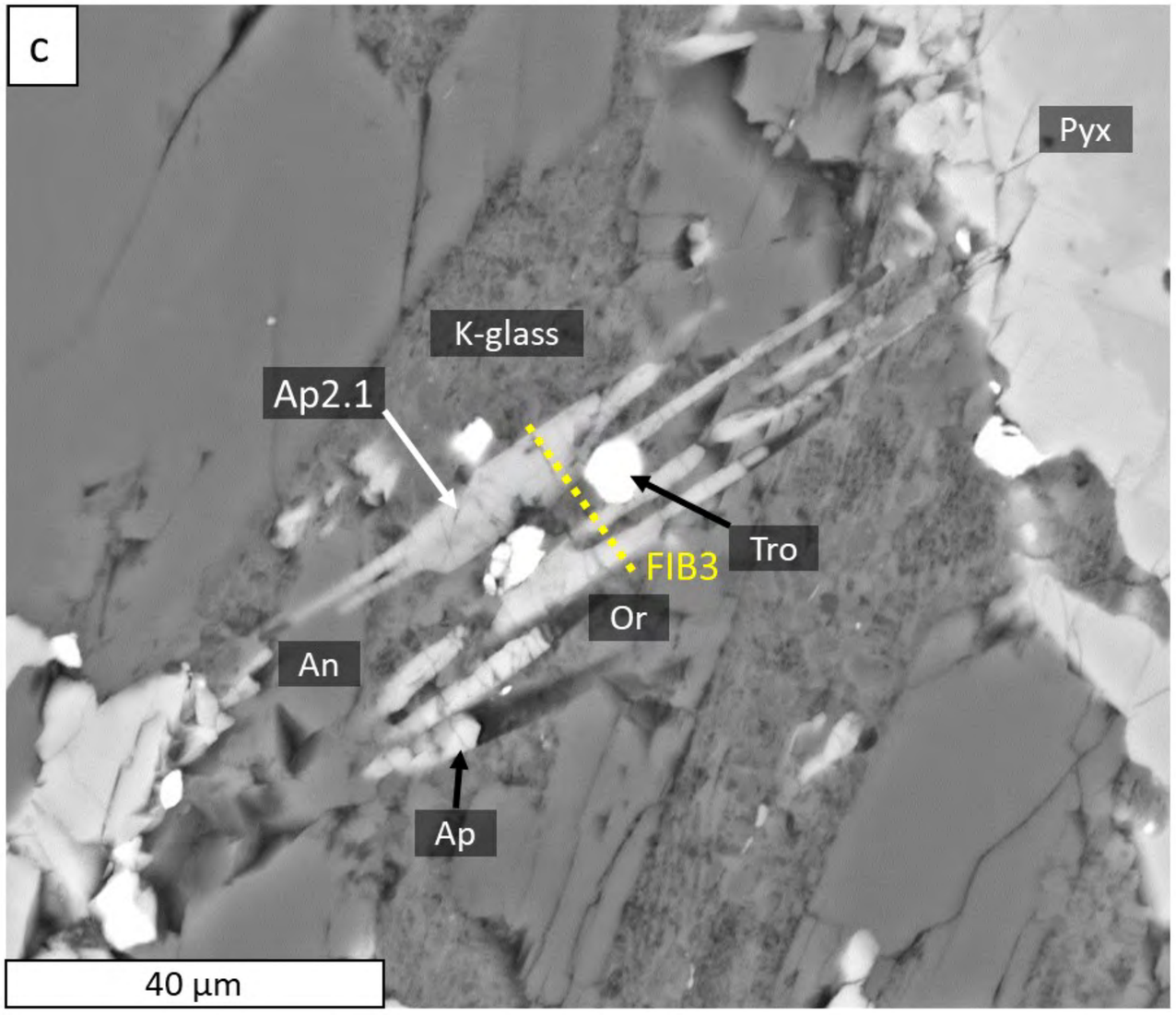
c
Pyx
K-glass
Ap2.1
FIB3
Tro
Or
An
Ap
40 µm

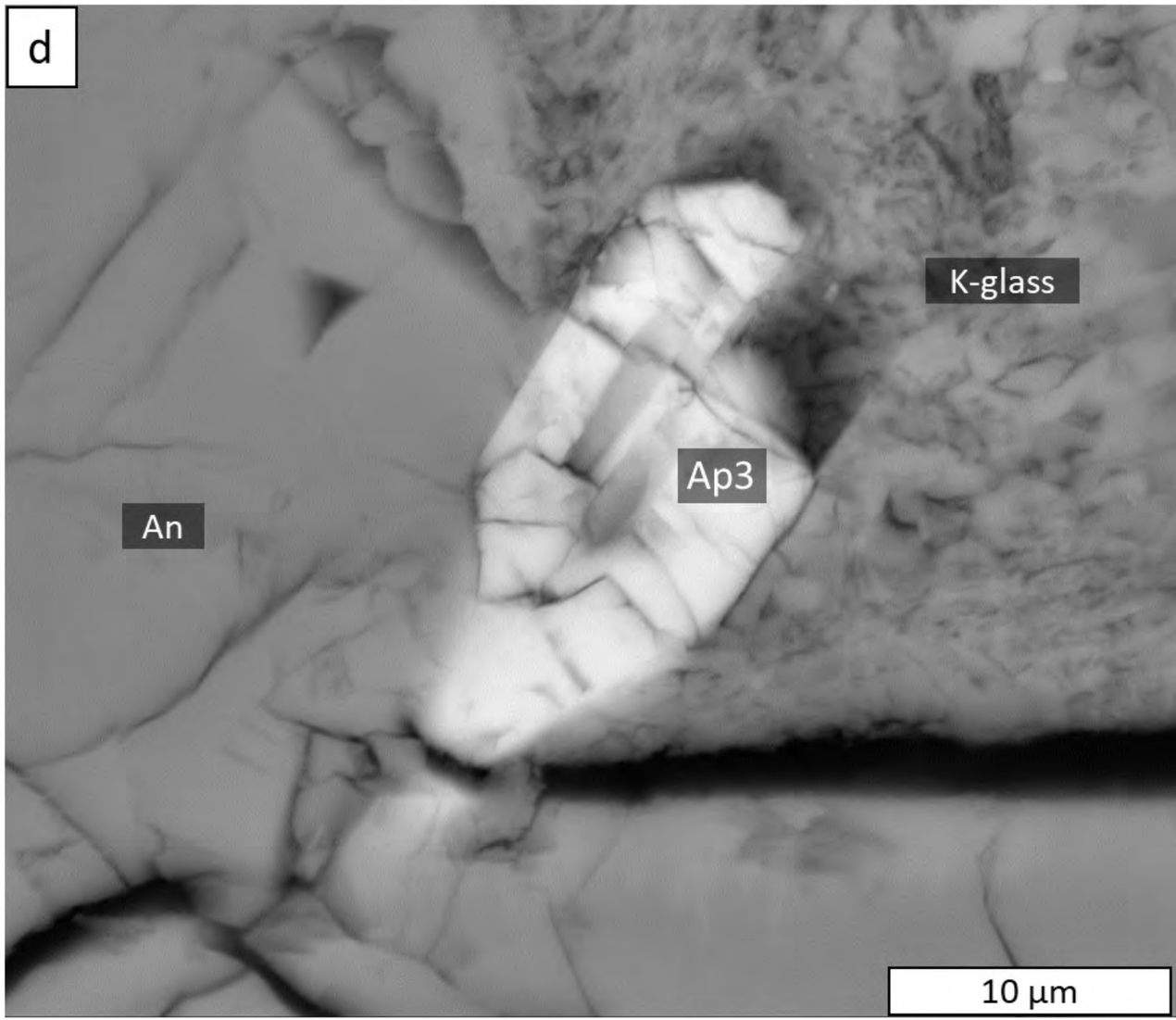
d
K-glass
Ap3
An
10 µm

Figure 4

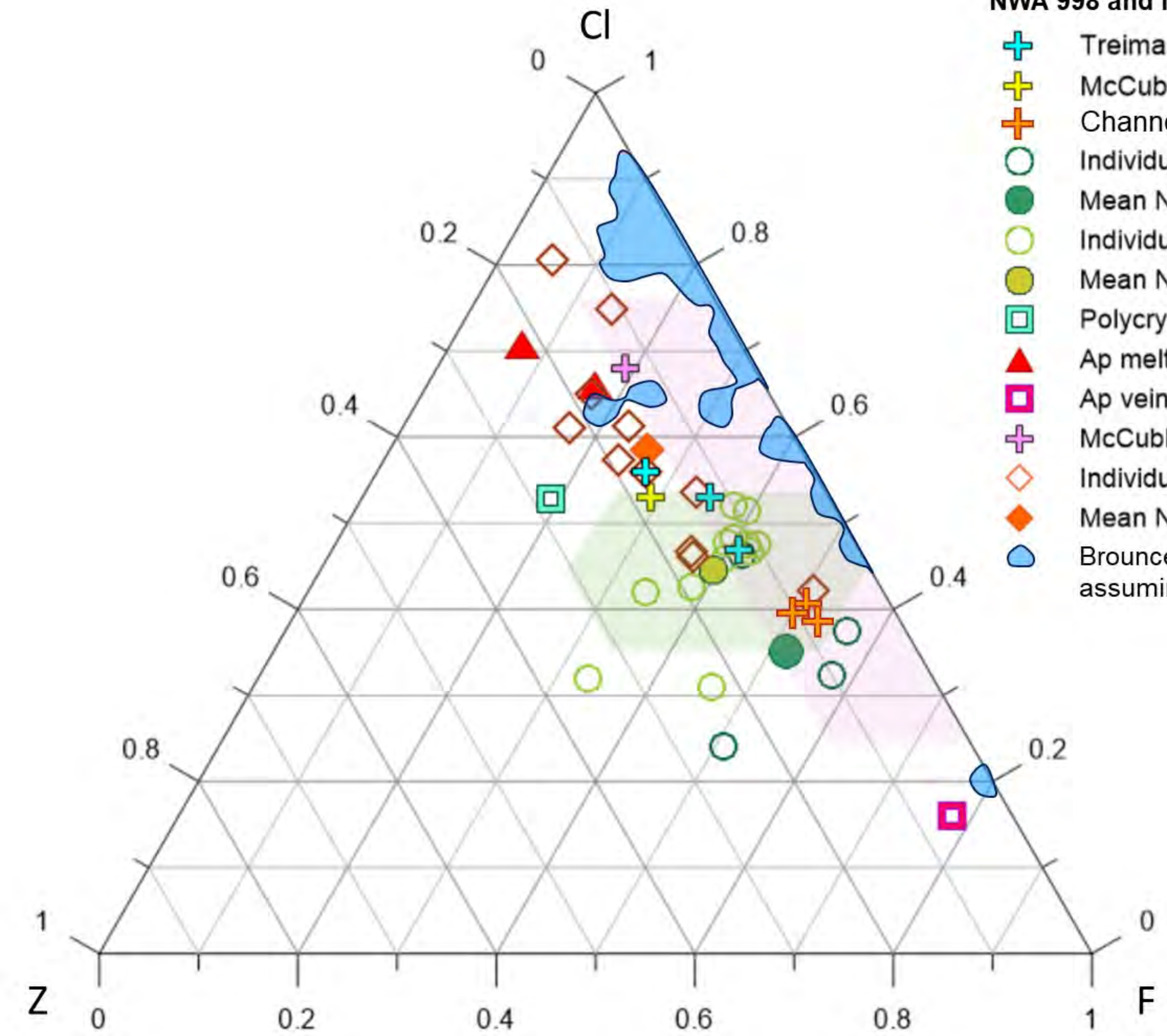

NWA 998 and Nakhla apatites

- Treiman & Irving (2008) NWA 998 **(EPMA)**
- McCubbin et al. (2013) NWA 998 **(EPMA)**
- Channon (2013) NWA 998 (SIMS)
- Individual NWA 998 FIB1 **(this work)**
- Mean NWA 998 FIB1 **(this work)**
- Individual NWA 998 FIB2 **(this work)**
- Mean NWA 998 FIB2 **(this work)**
- Polycryst. Ap NWA 998 FIB2 **(this work)**
- Ap melt incl. NWA 998 FIB2 **(this work)**
- Ap vein NWA 998 FIB2 **(this work)**
- McCubbin et al. (2013) Nakhla **(EPMA)**
- Individual Nakhla FIB3 **(this work)**
- Mean Nakhla FIB3 **(this work)**
- Brounce et al. (2022) Nakhla, $Z = OH + S^{2-}$ assuming $1–F–Cl = OH + S^{2-}$ (EPMA)

Figure 5

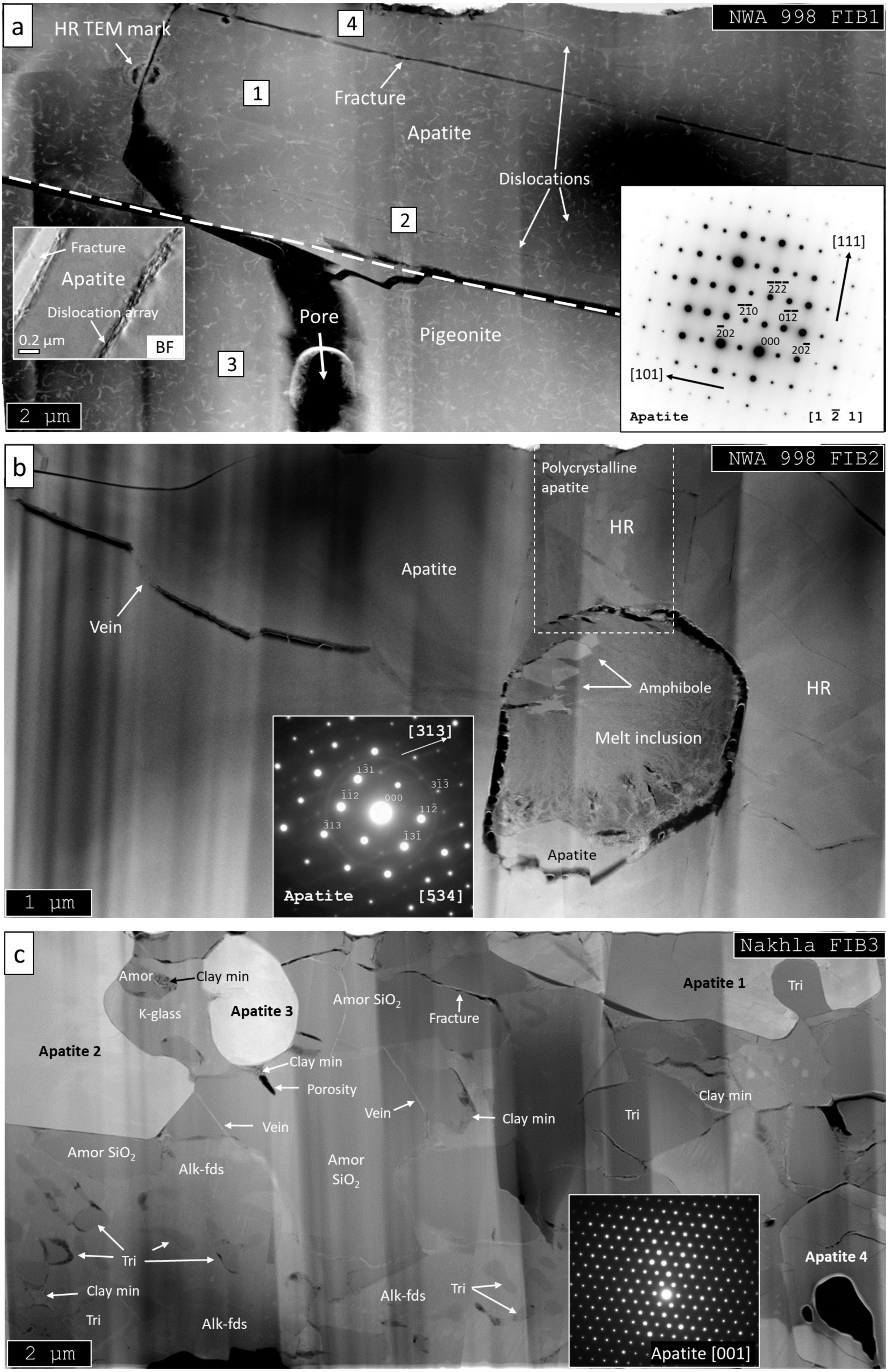
a
NWA 998 FIB1
HR TEM mark
4
1
Fracture
Apatite
Dislocations
2
Fracture
Apatite
Dislocation array
0.2 µm
BF
Pore
3
Pigeonite
2 µm
[111]
[101]
Apatite
[1 2̄ 1]
b
NWA 998 FIB2
Polycrystalline apatite
HR
Apatite
Vein
Amphibole
HR
Melt inclusion
Apatite
[313]
Apatite
[534]
1 µm
c
Nakhla FIB3
Amor
Clay min
K-glass
Apatite 3
Amor SiO2
Fracture
Apatite 1
Tri
Apatite 2
Clay min
Porosity
Vein
Vein
Clay min
Tri
Clay min
Amor SiO2
Alk-fds
Amor SiO2
Tri
Clay min
Tri
Alk-fds
Alk-fds
Tri
Apatite 4
Apatite [001]
2 µm

Figure 6

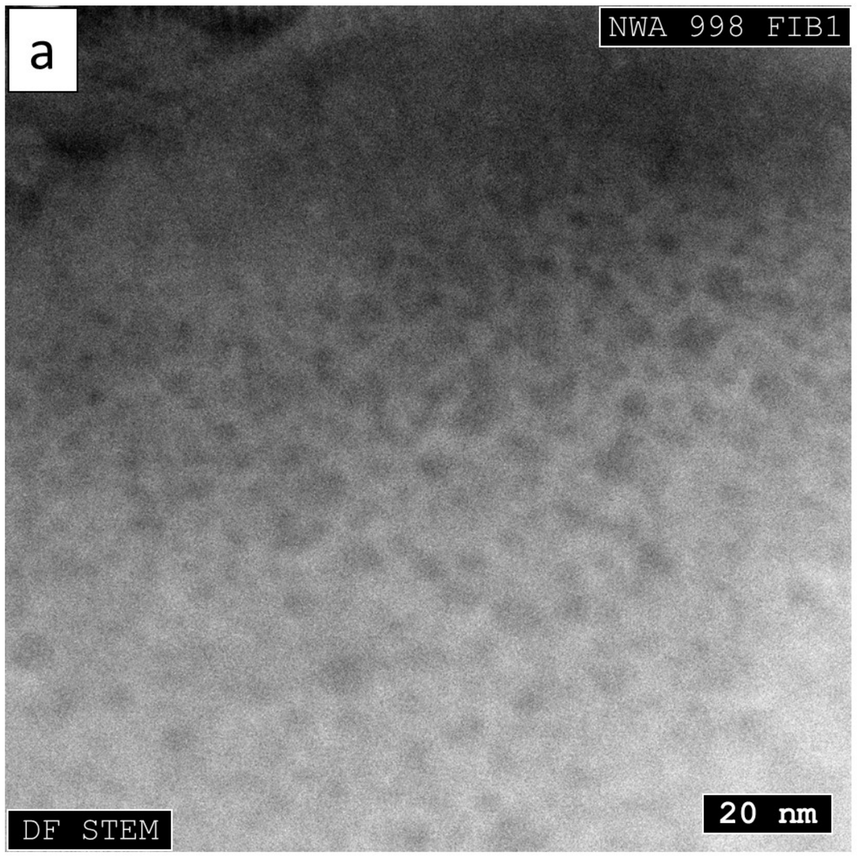
a
NWA 998 FIB1
DF STEM
20 nm

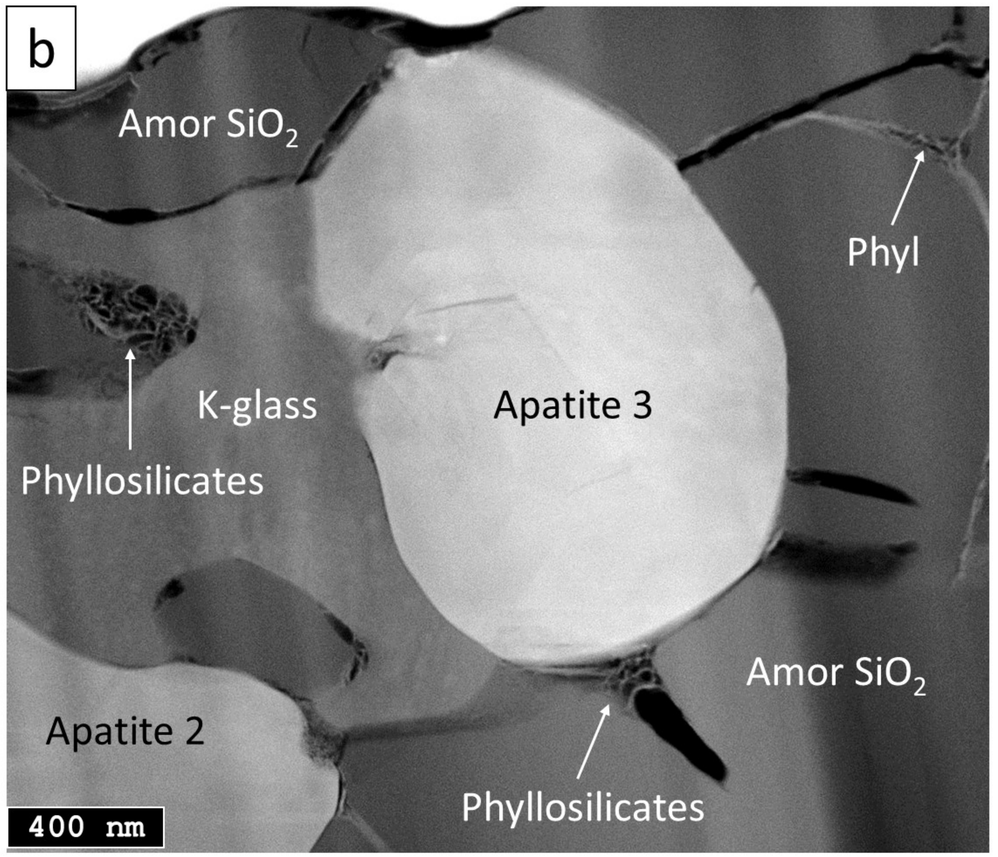
b
Amor SiO_2
Phyl
K-glass
Apatite 3
Phyllosilicates
Amor SiO_2
Apatite 2
Phyllosilicates
400 nm

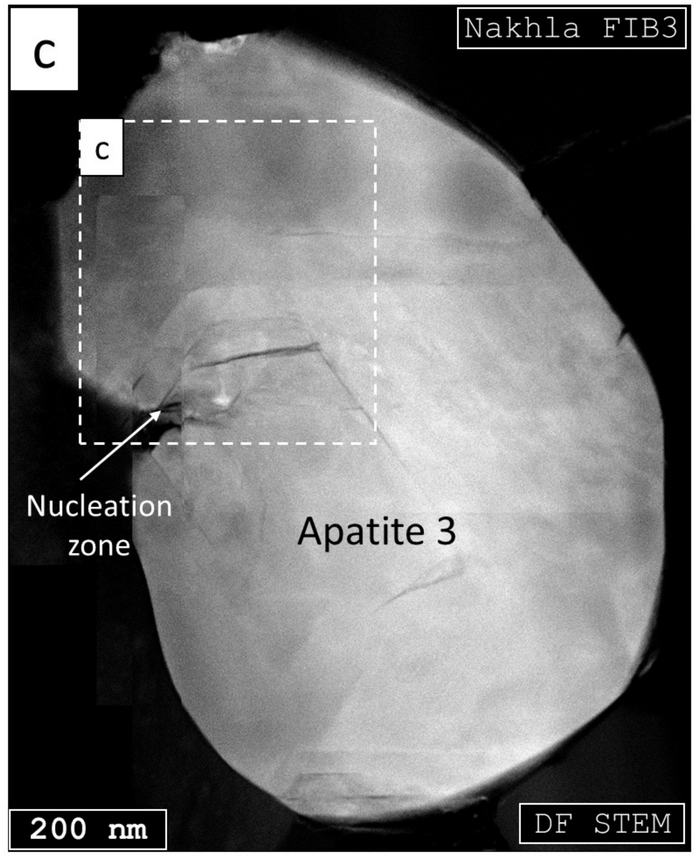
c
Nakhla FIB3
c
Nucleation zone
Apatite 3
200 nm
DF STEM

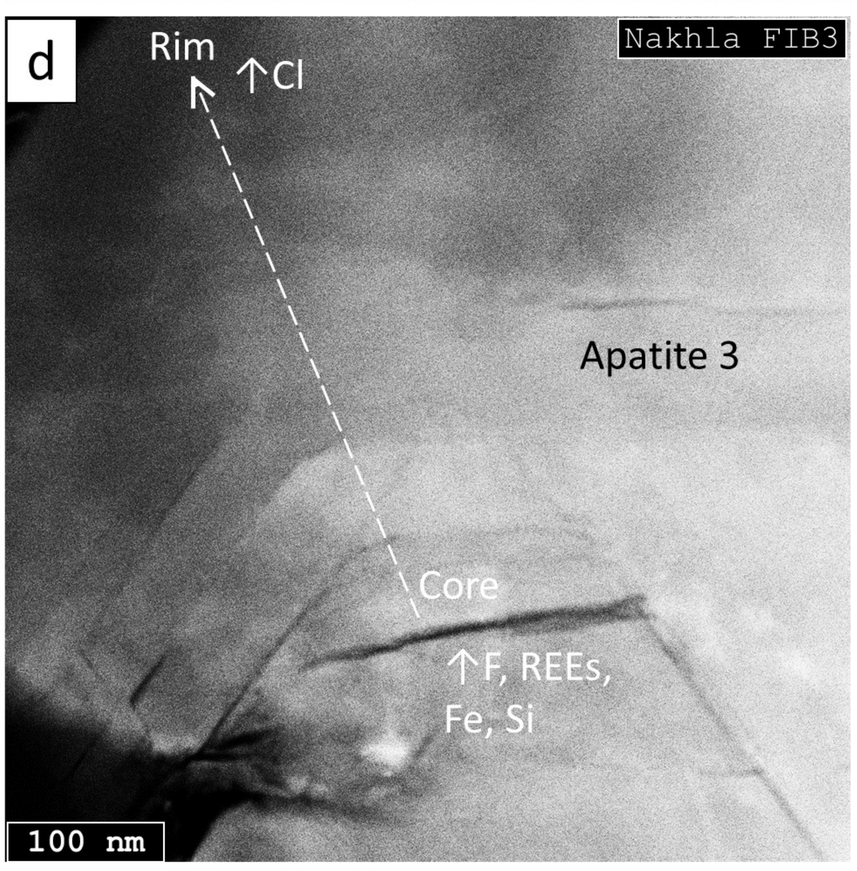
d
Rim
↑Cl
Nakhla FIB3
Apatite 3
Core
↑F, REEs, Fe, Si
100 nm

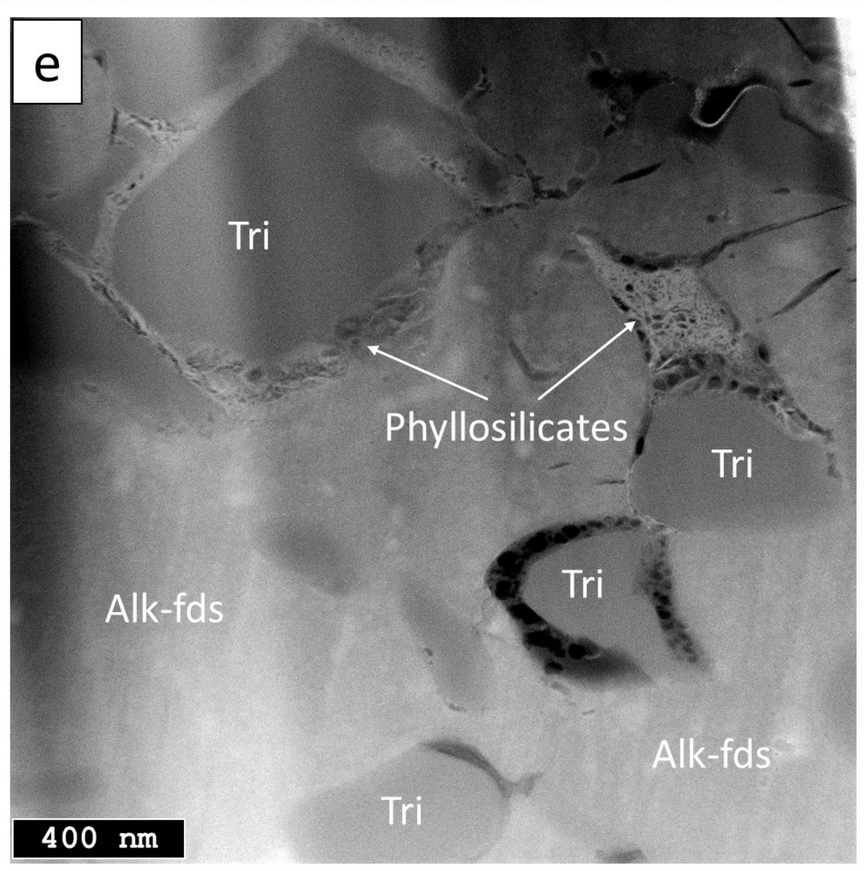
e
Tri
Phyllosilicates
Tri
Tri
Alk-fds
Alk-fds
Tri
400 nm

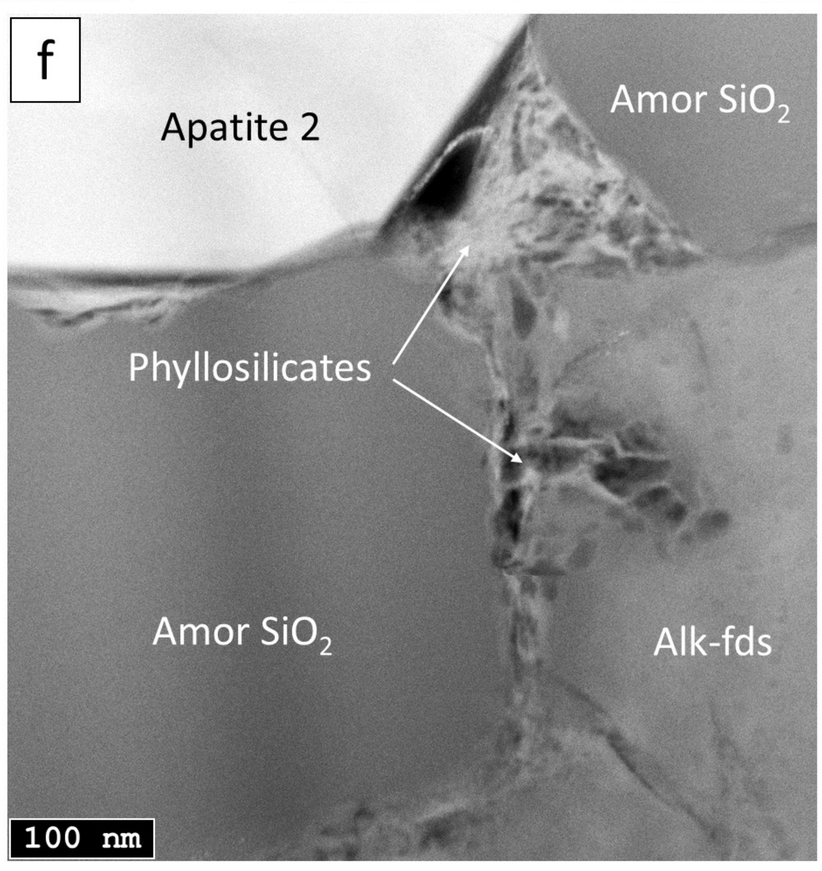
f
Apatite 2
Amor SiO_2
Phyllosilicates
Amor SiO_2
Alk-fds
100 nm

Figure 7

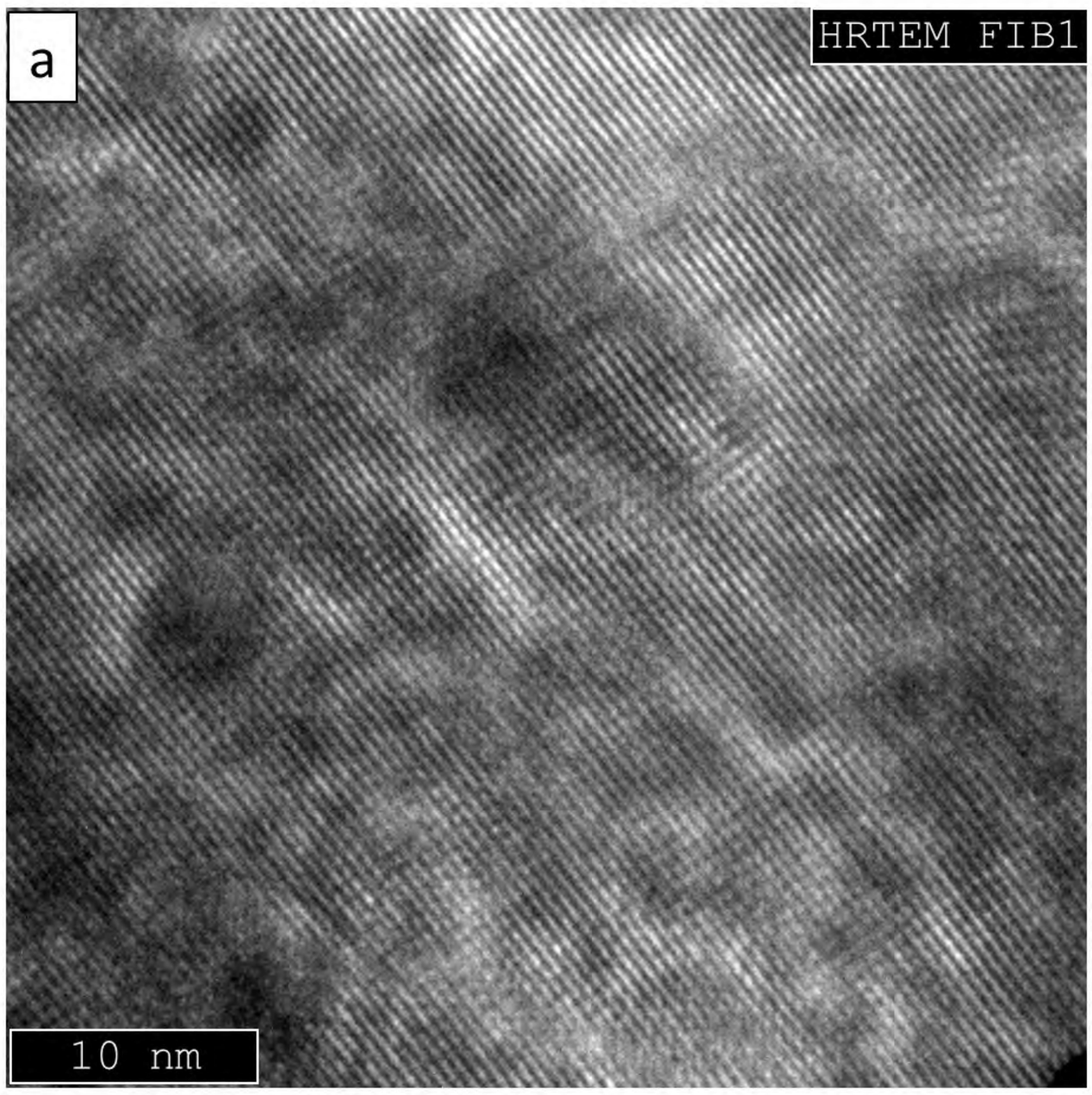
a
HRTEM FIB1
10 nm

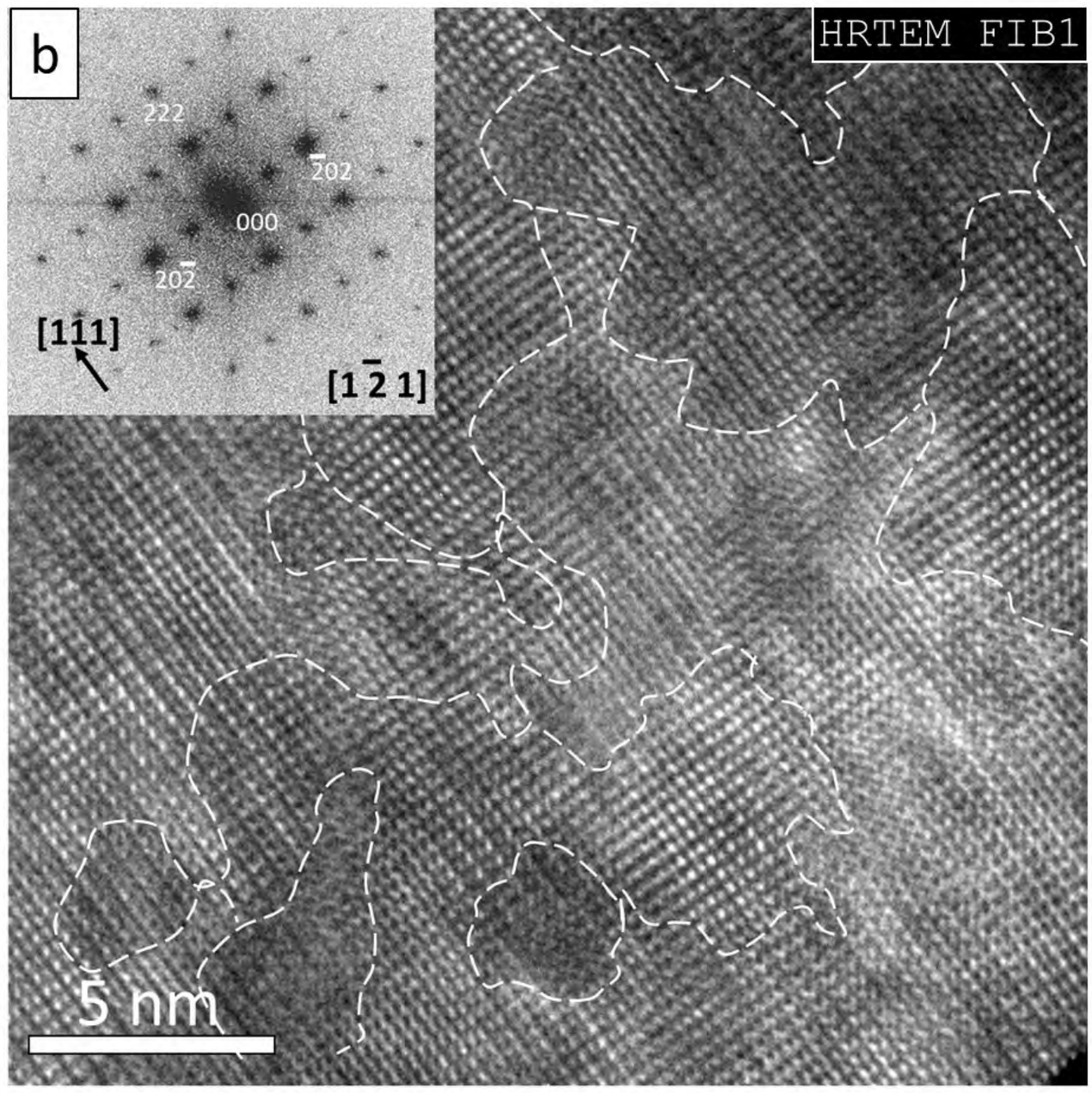
b
HRTEM FIB1
222
$\bar{2}02$
000
$20\bar{2}$
[1$\bar{1}$1]
[1 $\bar{2}$ 1]
5 nm

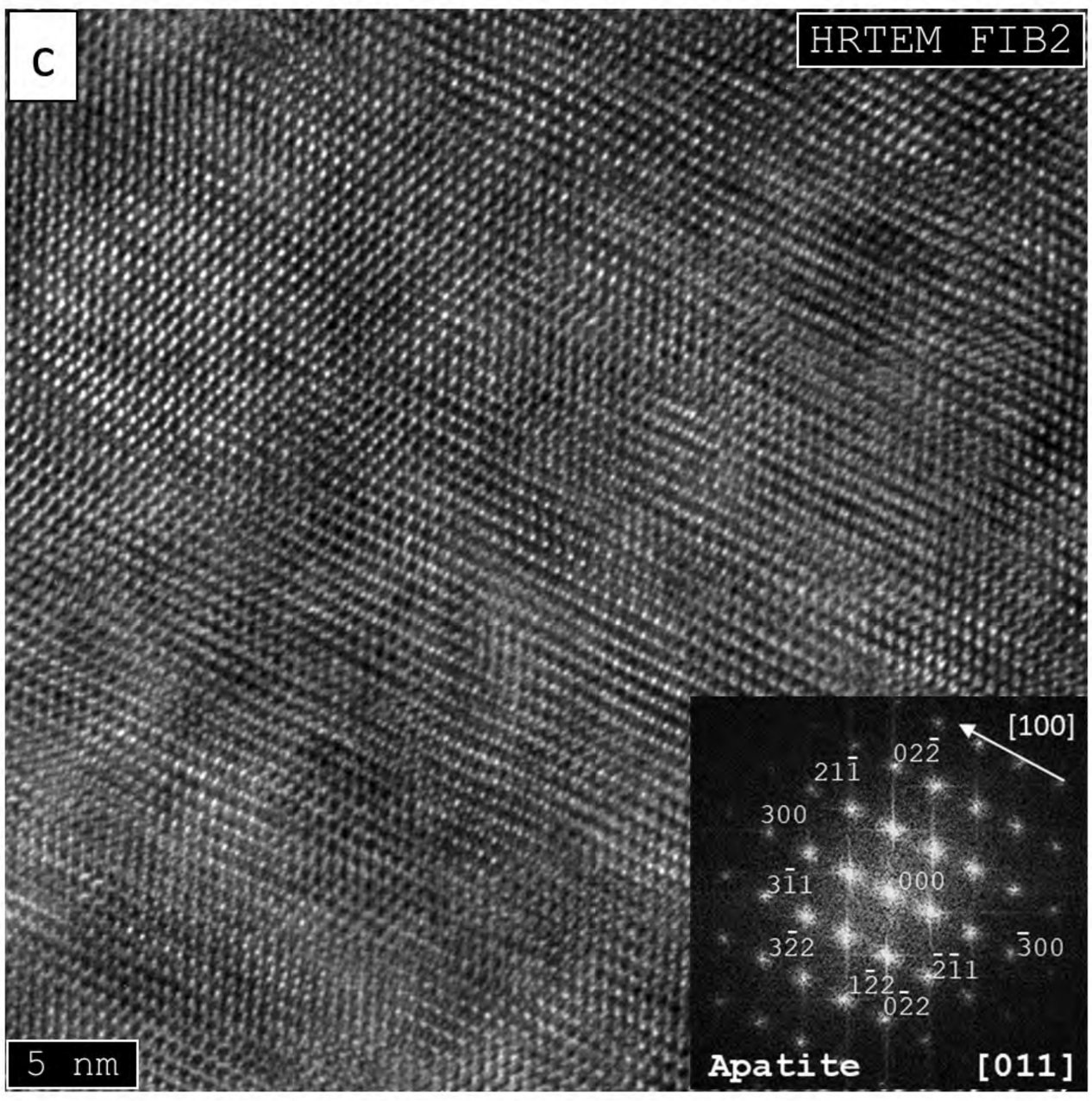
c
HRTEM FIB2
[100]
$21\bar{1}$
$02\bar{2}$
300
$3\bar{1}1$
000
$3\bar{2}2$
$\bar{3}00$
$\bar{2}11$
$1\bar{2}2$
$0\bar{2}2$
Apatite
[011]
5 nm

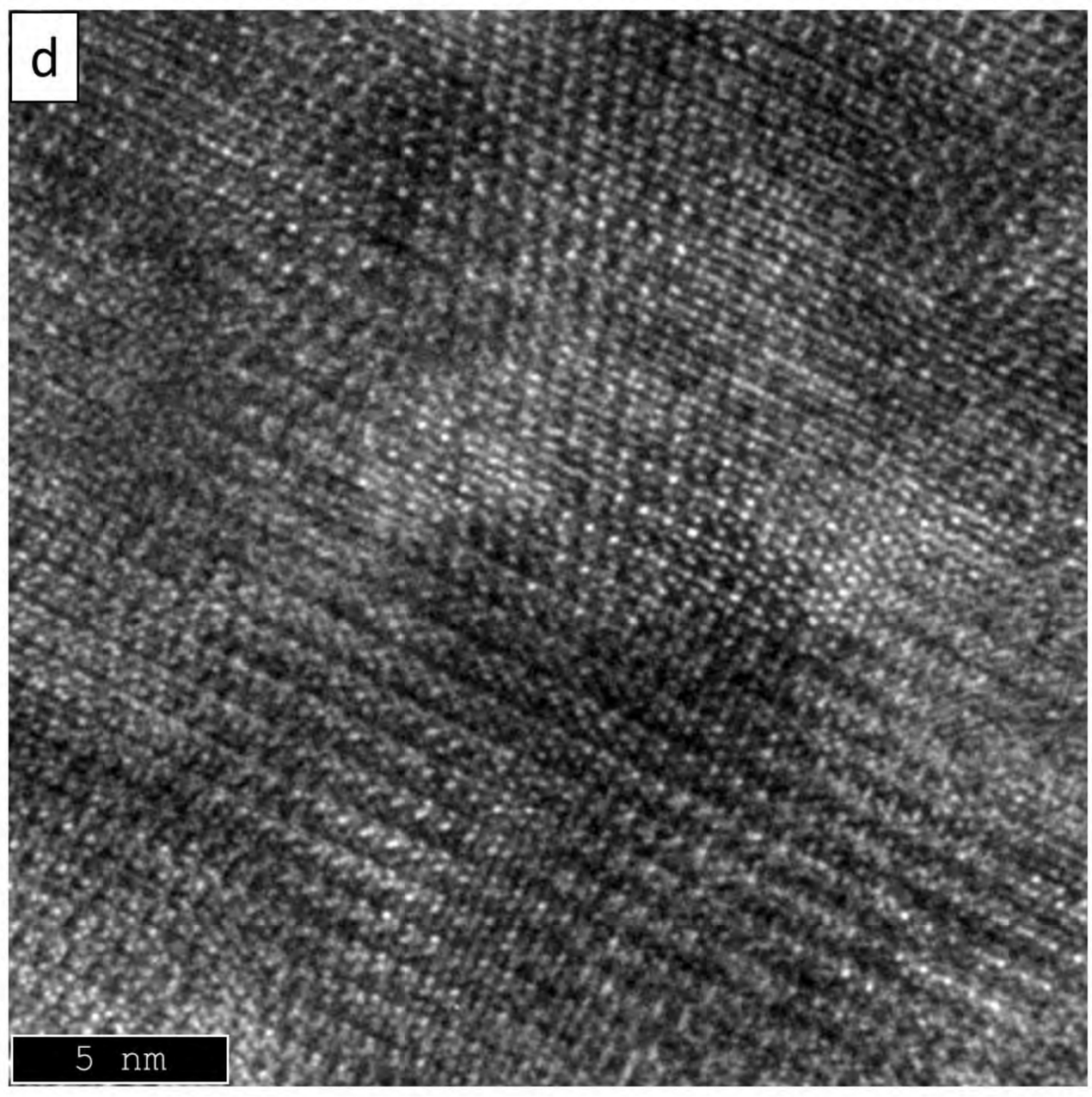
d
5 nm

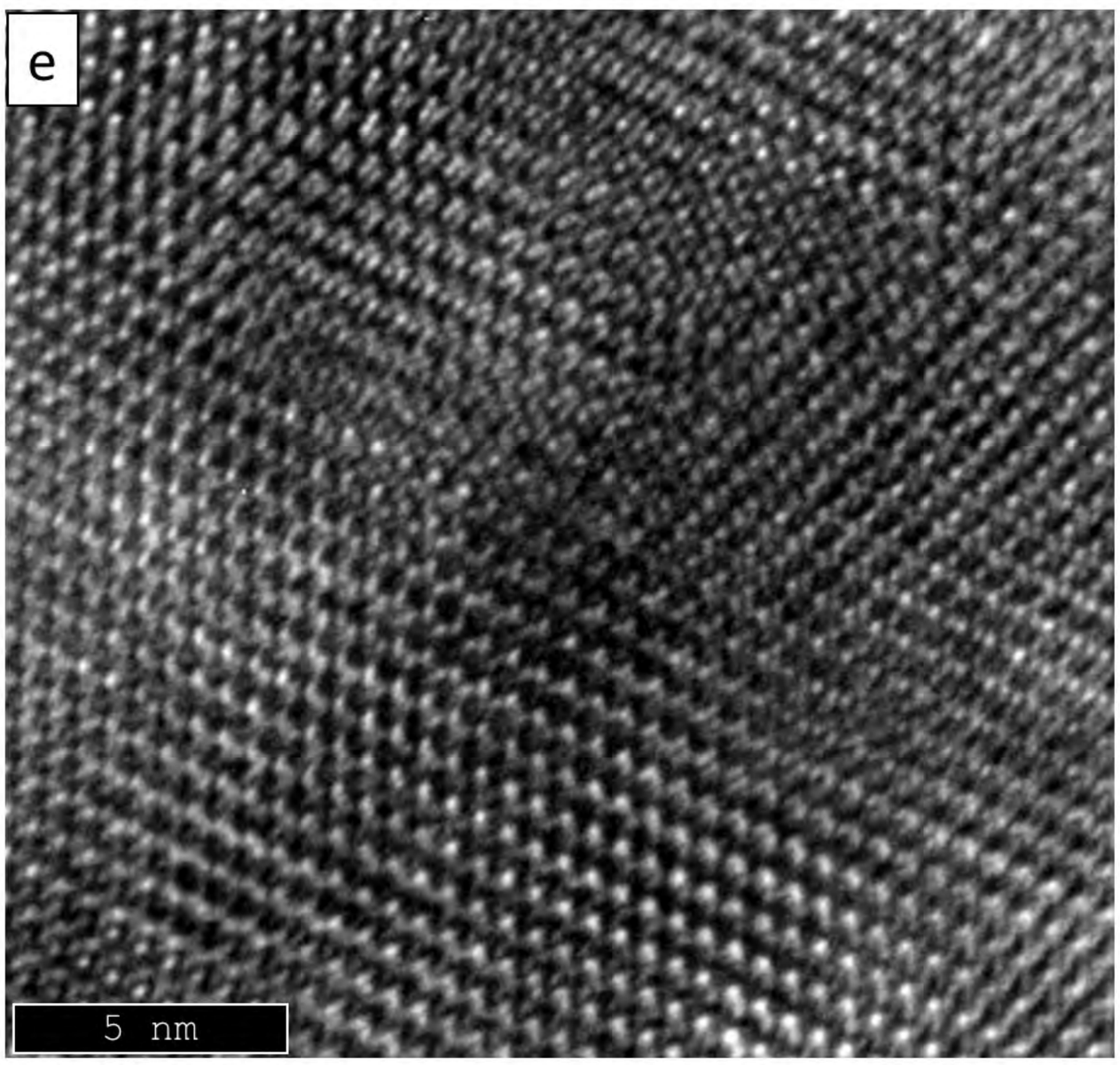
e
5 nm

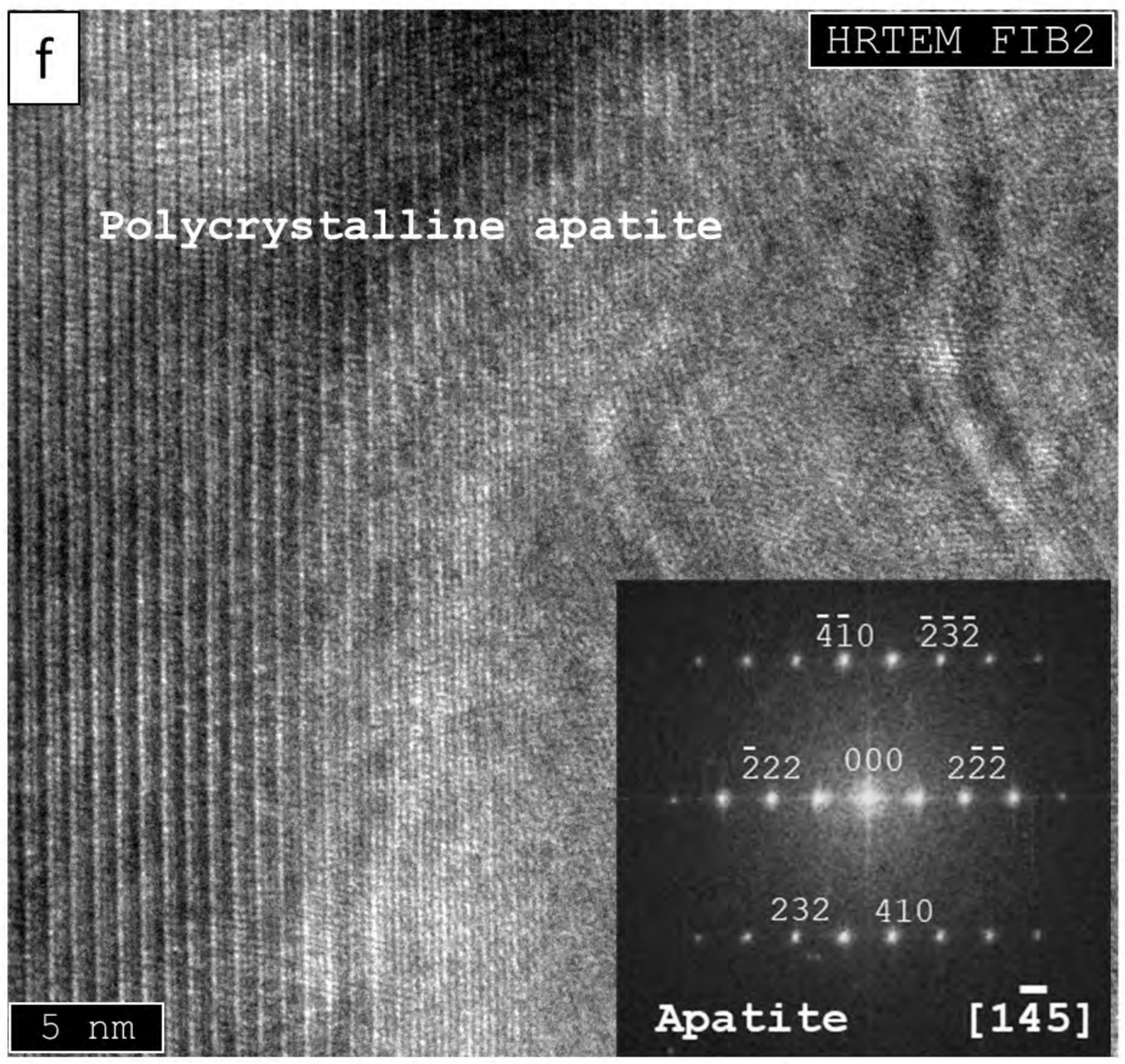
f
HRTEM FIB2
Polycrystalline apatite
$\bar{4}\bar{1}0$
$\bar{2}\bar{3}\bar{2}$
$\bar{2}22$
000
$2\bar{2}\bar{2}$
232
410
Apatite
[1$\bar{4}\bar{5}$]
5 nm

Figure 8

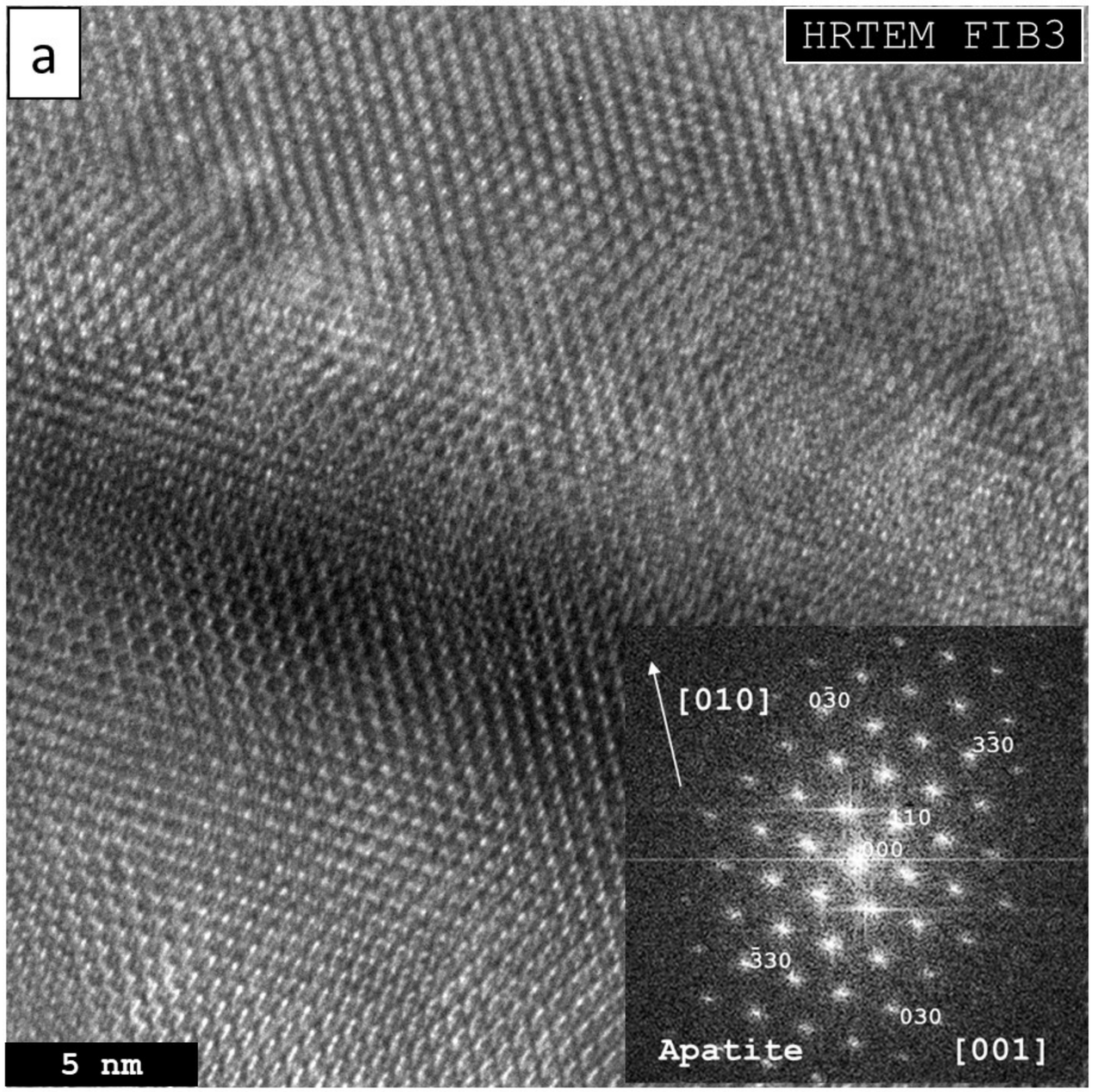
a
HRTEM FIB3
[010]
0$\bar{3}$0
3$\bar{3}$0
110
000
$\bar{3}$30
030
Apatite
[001]
5 nm

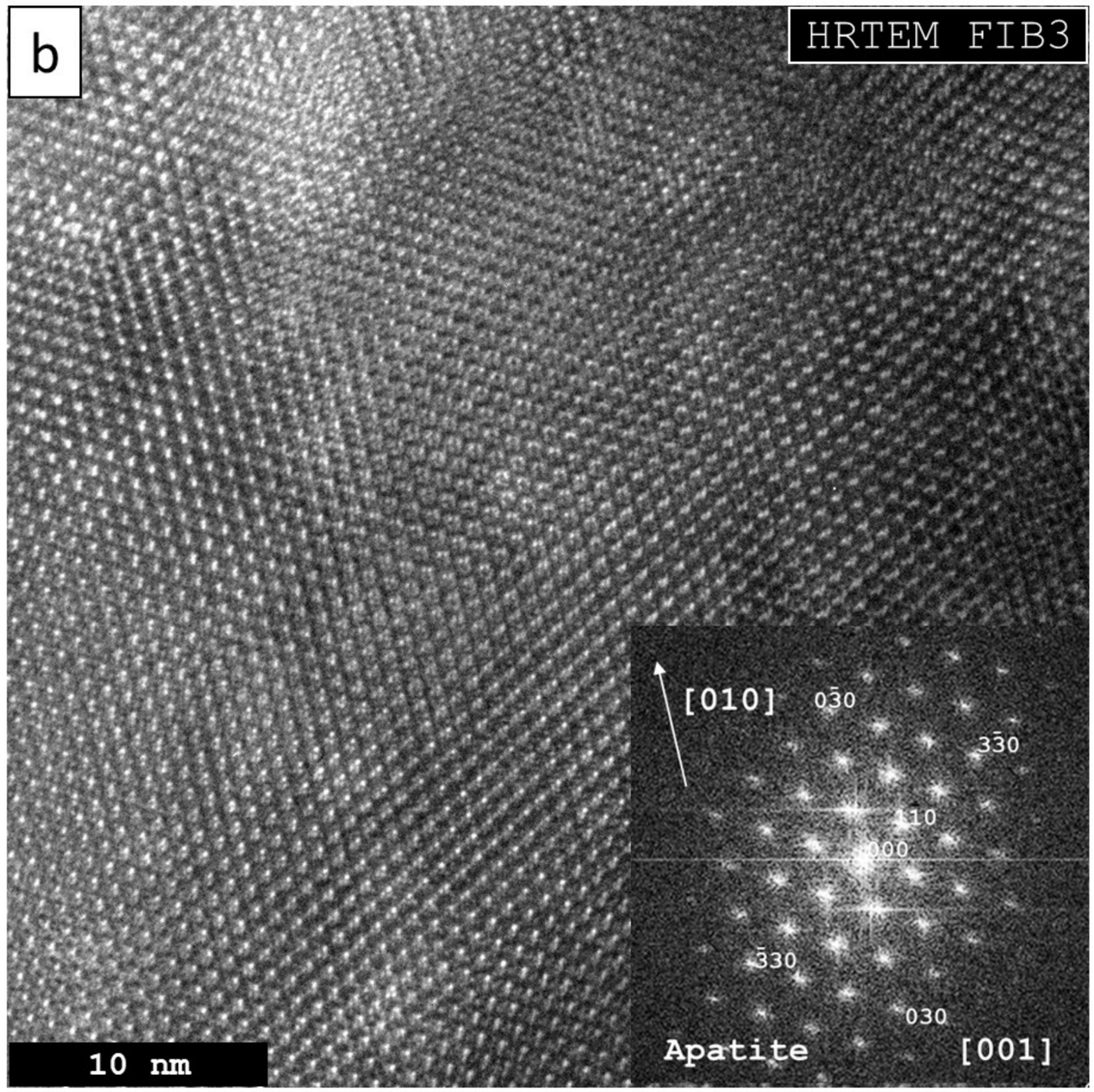
b
HRTEM FIB3
[010]
0$\bar{3}$0
3$\bar{3}$0
110
000
$\bar{3}$30
030
Apatite
[001]
10 nm

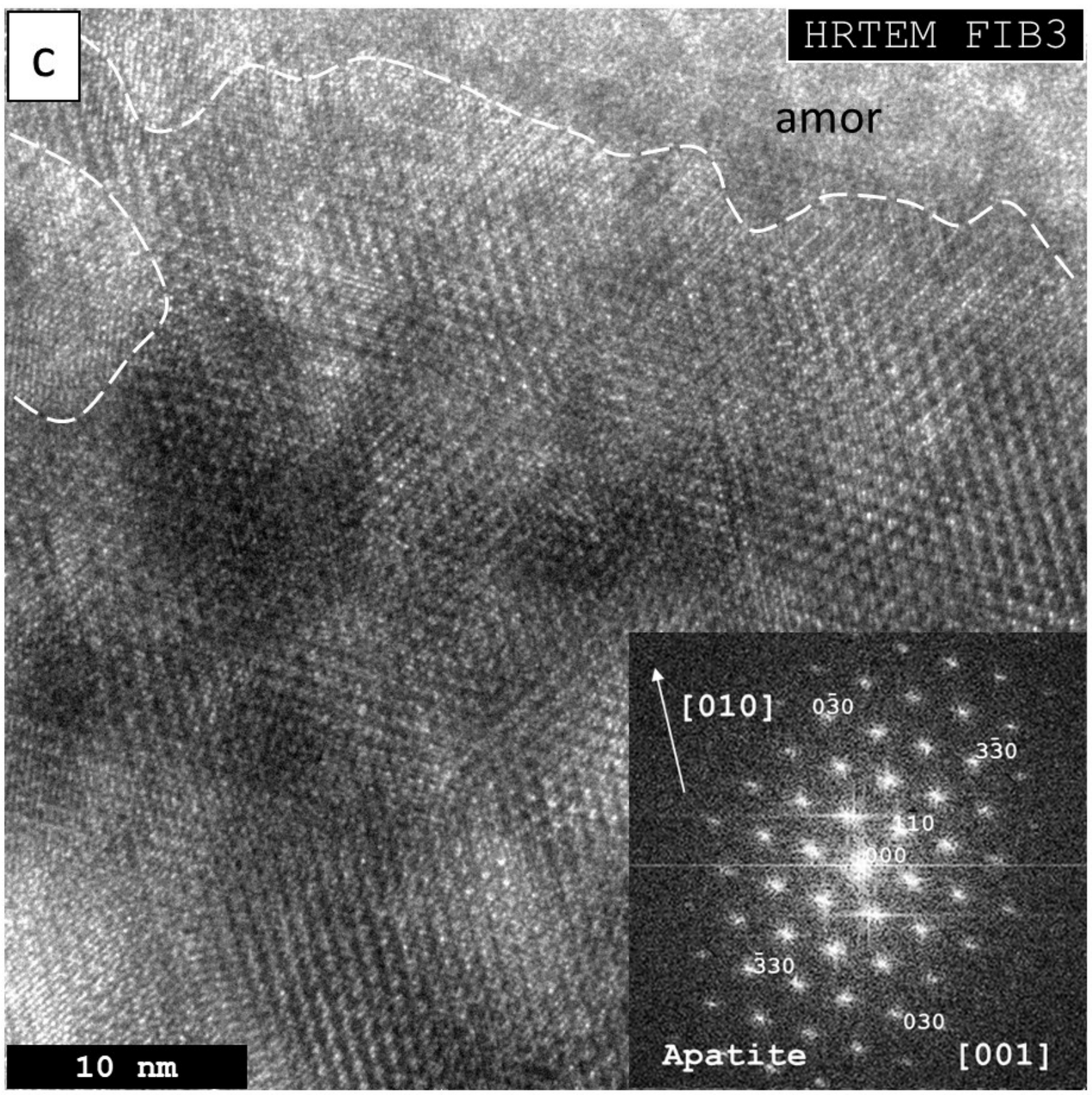
c
HRTEM FIB3
amor
[010]
0$\bar{3}$0
3$\bar{3}$0
110
000
$\bar{3}$30
030
Apatite
[001]
10 nm

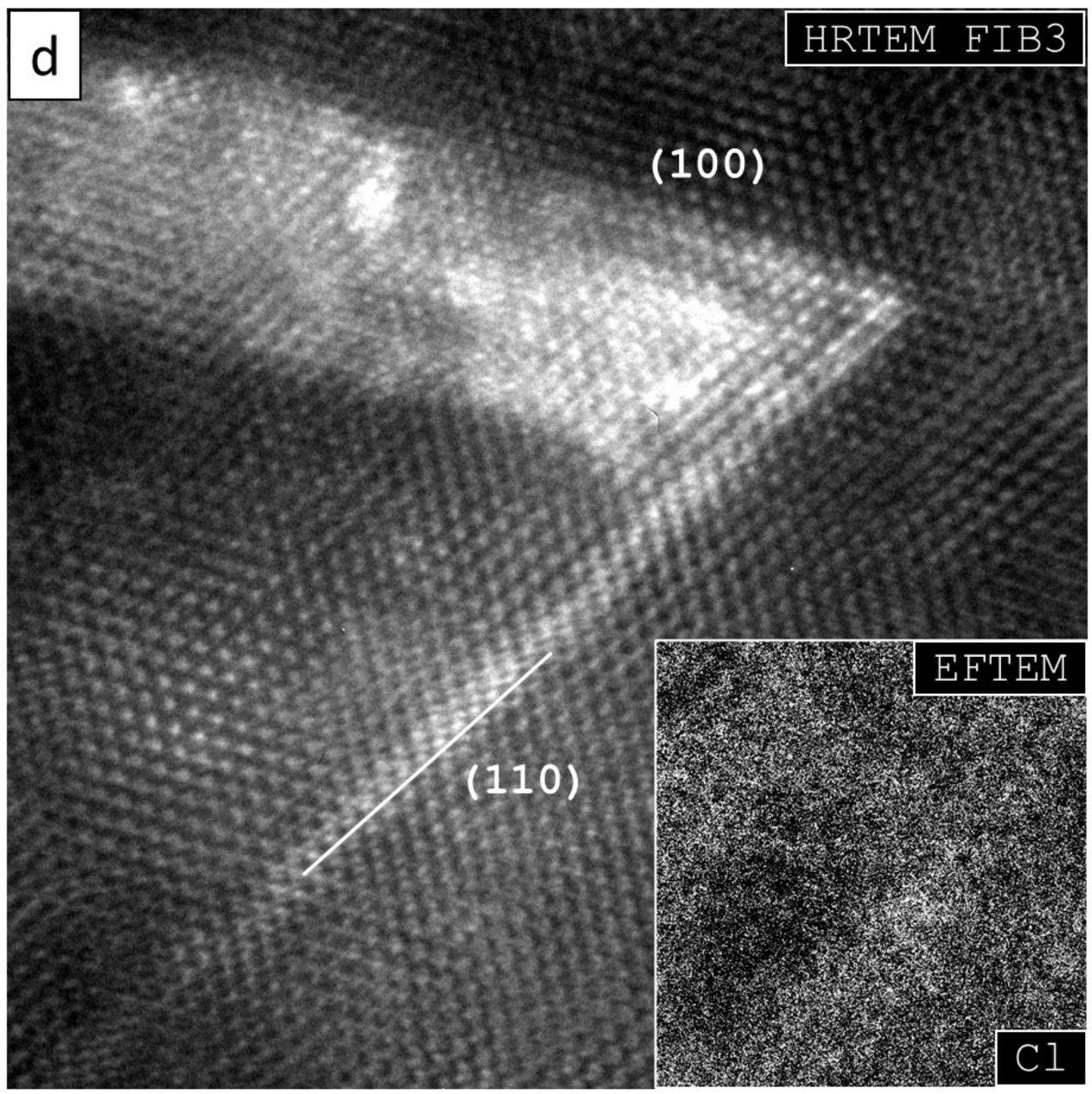
d
HRTEM FIB3
(100)
(110)
EFTEM
Cl

Figure 9

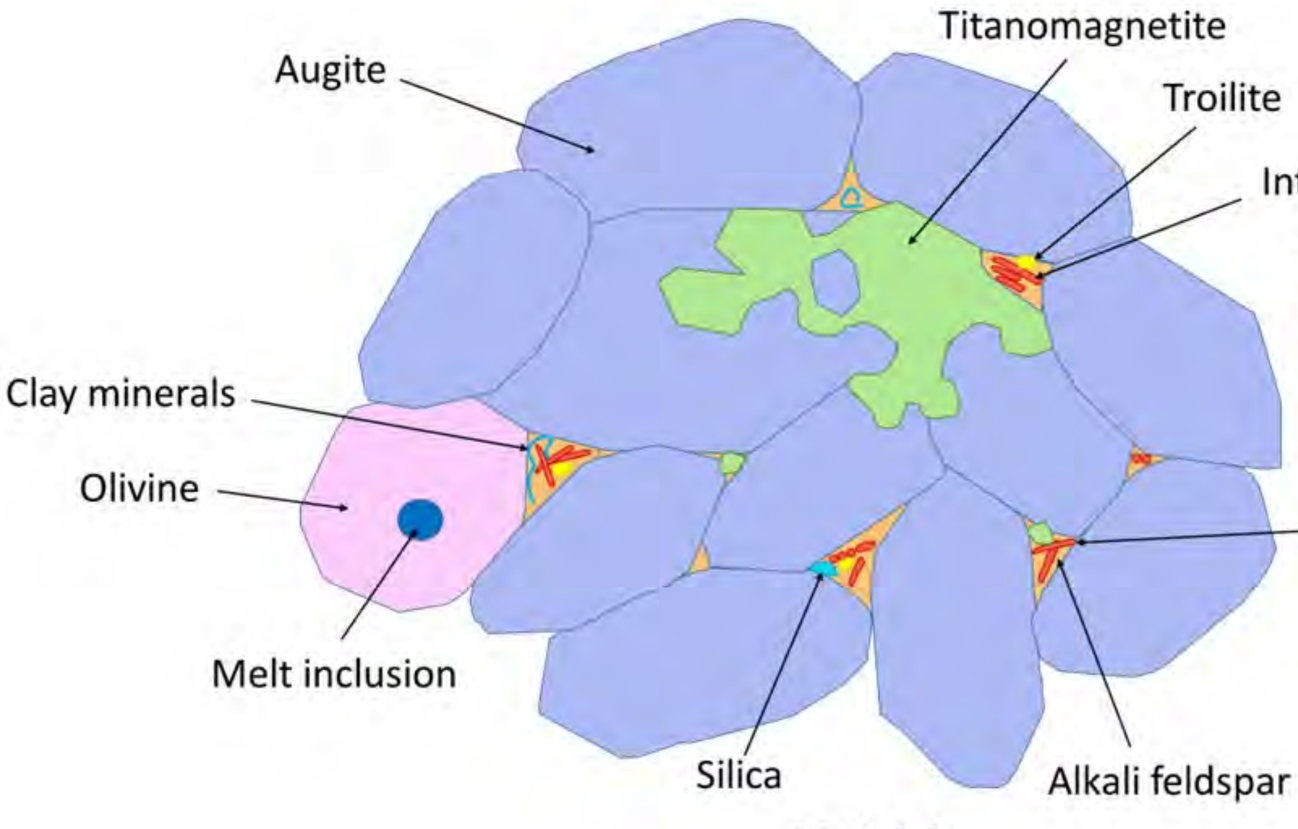

Nakhla

Intercumulus apatite:
0.95 wt% F
4.02 wt% Cl

F: 5 – 51 mol%
Cl: 42 – 80 mol%
Z: 7 – 19 mol%

FIB3

Intercumulus apatite:
0.72 wt% F
4.65 wt% Cl

F: 12 – 76 mol%
Cl: 24 – 75 mol%
Z: 0 – 14 mol%

(McCubbin et al., 2013)

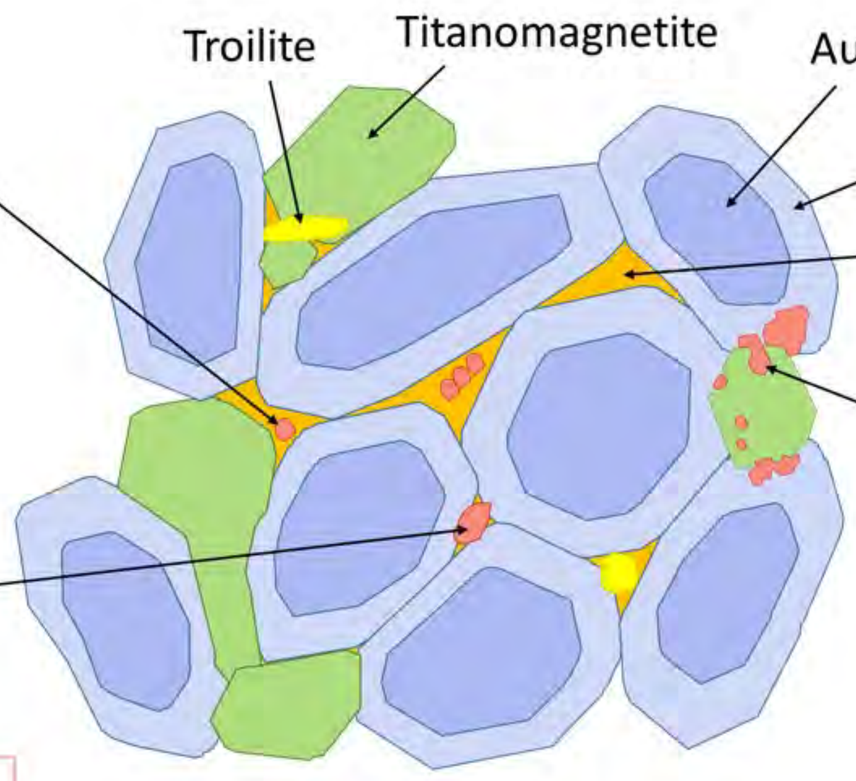

NWA 998

Intercumulus apatite
1.06 wt% F
3.68 wt% Cl

F: 29 – 55 mol%
Cl: 37 – 54 mol%
Z: 0 – 30 mol%

(McCubbin et al., 2013)

Intercumulus mesostasis
(K-fds, alkali-glass, pyrrhotite, chalcopyrite, etc.)

Cumulus apatite (Ap-C) host:
1.5 wt% F
3.1 wt% Cl

F: 33 – 46 mol%
Cl: 31 – 52 mol%
Z: 9 – 35 mol%

Ap in Ap-C-host melt inclusion:
0.4 wt% F
4.7 wt% Cl

FIB2

Cumulus apatite
1.9 wt% F
2.4 wt% Cl

F: 42 – 58 mol%
Cl: 24 – 46 mol%
Z: 6 – 25 mol%

FIB1

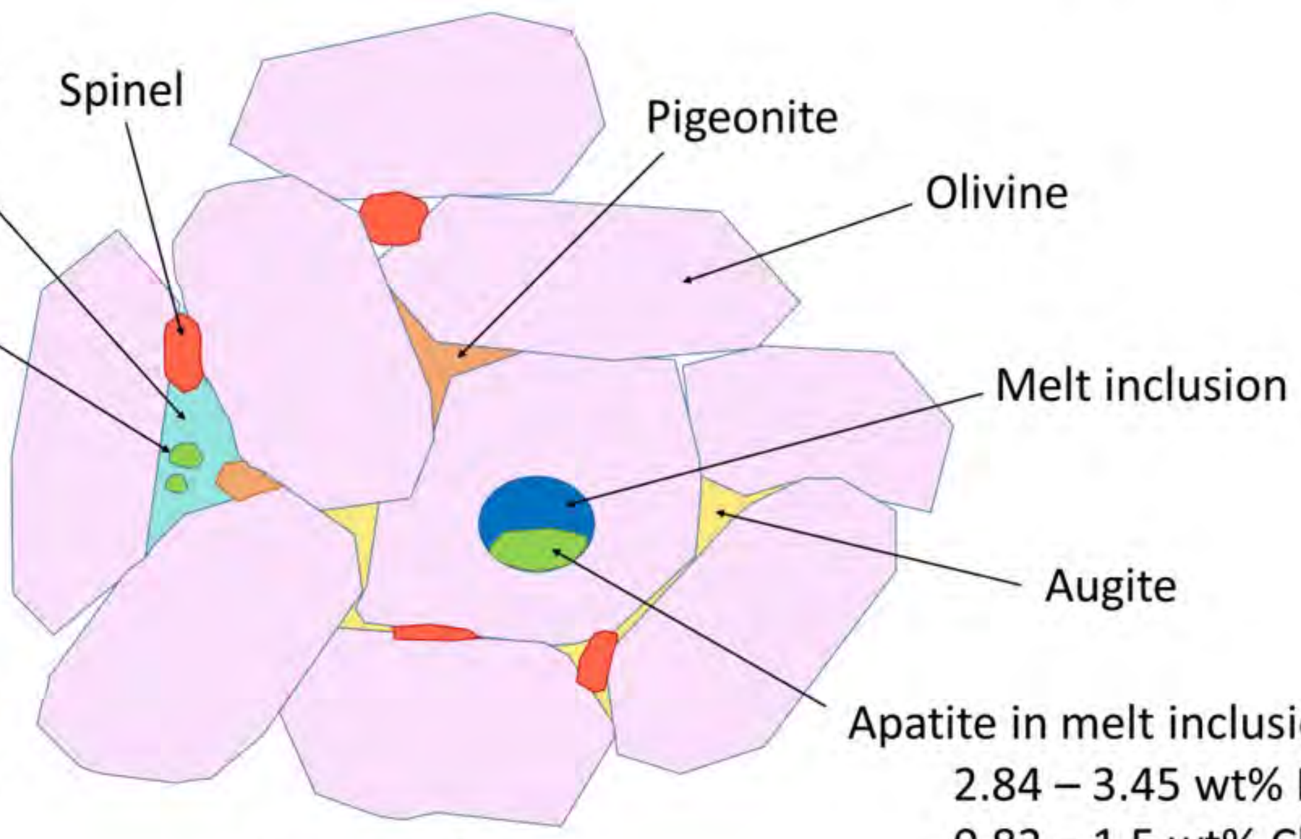

Chassignites

Intercumulus apatite

NWA 8694

2.34 wt% F[d]
2.20 wt% Cl[d]

Chassigny

1.33 – 2 wt% F[c]
3.13 – 3.92 wt% Cl[c]

NWA 2737

1.36 wt% F[a] 2.11 wt% F[b]
2.68 wt% Cl[a] 2.21 wt% Cl[b]

Apatite in melt inclusion[a]
2.84 – 3.45 wt% F
0.82 – 1.5 wt% Cl

[a]Beck et al., 2006
[b]McCubbin et al., 2013
[c]McCubbin and Nekvasil, 2008
[d]Hewins et al., 2020

Upper in the cumulus pile

Base of the cumulus pile

deeper

Figure 10

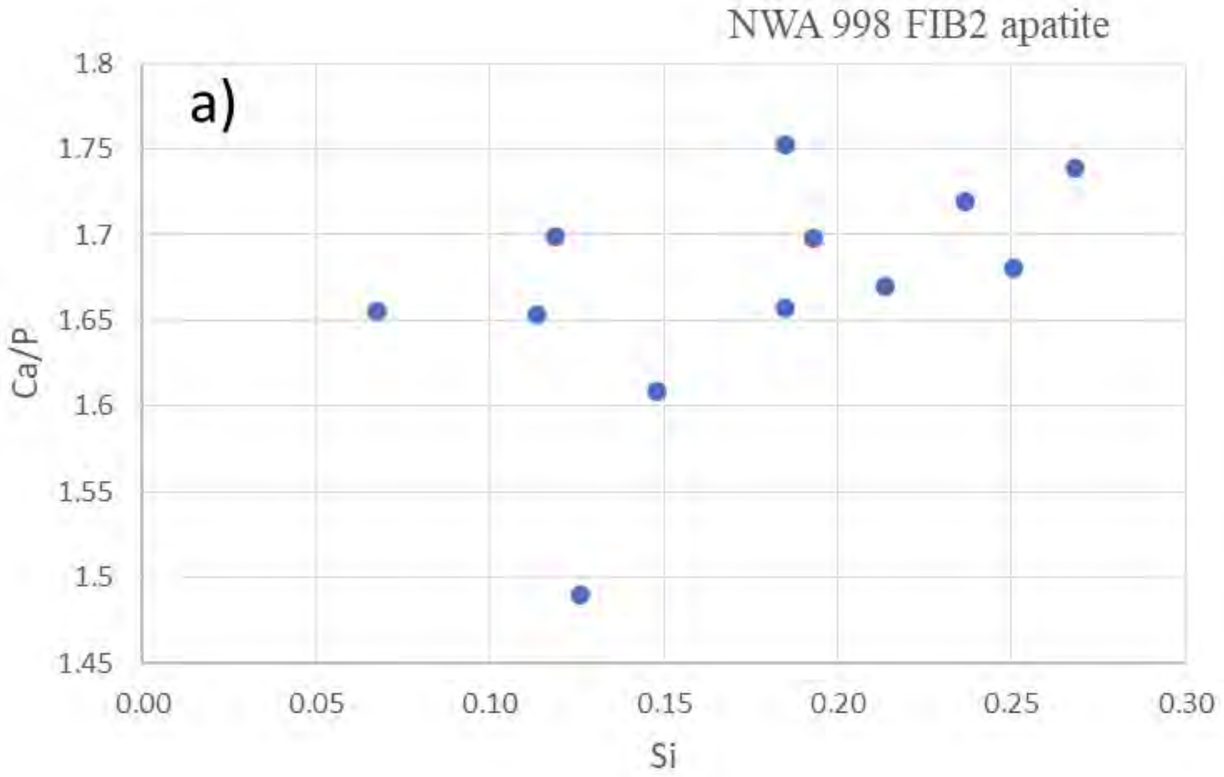
NWA 998 FIB2 apatite
a)
Ca/P
Si
1.8
1.75
1.7
1.65
1.6
1.55
1.5
1.45
0.00
0.05
0.10
0.15
0.20
0.25
0.30

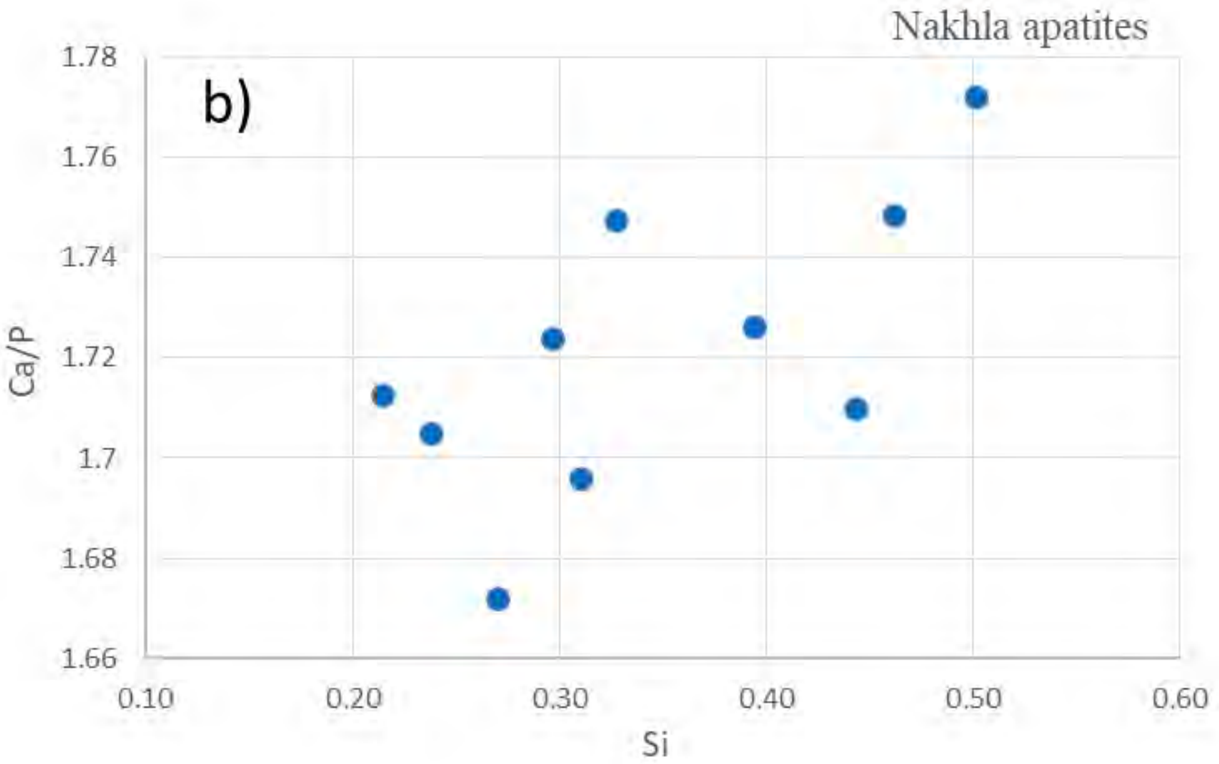
Nakhla apatites
b)
Ca/P
Si
1.78
1.76
1.74
1.72
1.7
1.68
1.66
0.10
0.20
0.30
0.40
0.50
0.60